The University of Nottingham

Effects of Metal Modification on Titanium Dioxide for Photocatalytic Reduction of Carbon Dioxide

Dong Liu, MSc

Thesis submitted to the University of Nottingham for the degree of

Doctor of Philosophy

March 2012

Abstract

To study the effects of metal modification on titanium dioxide (TiO_2) for photocatalytic reduction of carbon dioxide (CO_2), a series of pure and metal modified TiO_2 catalysts (referred as SG TiO_2 and M/TiO_2, respectively) were synthesized via a refined sol-gel process. The metals chosen to modify TiO_2 included Cu, Zn, and Rh. These catalysts were then characterized by using various analytical techniques, including ICP-MS, powder XRD, XPS, TEM, N_2 adsorption isotherms, Cu surface area and dispersion measurement, and DR UV-Vis. It was found that all the sol-gel derived TiO_2 catalysts had the same crystalline phase of anatase, and similar particle sizes (11-16 nm) and surface areas (50.24-63.37 m^2/g). It is worthy to note that, even though synthesized via the same sol-gel process, the three added metals modified their TiO_2 supports differently. The added Cu and Zn were loaded on the surface of TiO_2 with their chemical states to be Cu_2O and ZnO, respectively. Whereas, the added Rh was substitutionally doped into the lattice of its TiO_2 supports. The specific surface area and dispersion of the added Cu on the surface of Cu/TiO_2 were further measured by using N_2O as adsorbate. It was found that the aggregation of the added Cu occurred when the Cu ratio of Cu/TiO_2 over-increased (over 0.03 wt%). The following CO_2 photoreduction experiments confirmed that the added Cu and Rh were able to significantly improve the activity of TiO_2 for CO_2 photoreduction to methane, wherein the activities of the best performing

0.03 wt% Cu/TiO_2 and 0.01 wt% Rh/TiO_2 were around 10-times higher than that of SG TiO_2. The added Cu and Rh were expected to affect the activity of TiO_2 via different ways. The combination of the loaded Cu and TiO_2 was considered to be a composite semiconductor catalyst, and the Cu dispersion dominated the activity of Cu/TiO_2. In comparison, the doped Rh was able to affect the activity of TiO_2 by introducing an additional energy level to the band-gap of TiO_2. Finally, TiO_2 catalysts simultaneously loaded by Cu and doped by Rh ($Rh/Cu/TiO_2$, synthesized via the identical sol-gel process) were also tested for CO_2 photoreduction. The results indicate that the loaded Cu and doped Rh were able to synergistically enhance the activity of TiO_2 for CO_2 photoreduction, allowing the optimal $Rh/Cu/TiO_2$ (0.06 wt% Rh/0.03 wt% Cu/TiO_2) to present even better (at least 25 % higher) activity than any of the Cu/TiO_2 or Rh/TiO_2 in this work.

Acknowledgements

I would like to thank my tutor, Prof. Mercedes Maroto-Valer, for her supervision during my PhD study.

I am grateful to Prof. Adam F. Lee of Cardiff University and Prof. Jeffery Chi-Sheng Wu of National Taiwan University, who have offered essential supports for my work. Meanwhile, I also wish to thank Dr. Di Hu of University of Nottingham, who has given me very helpful advice for my thesis correction.

Most importantly, I would like to thank my families: my parents, Mr. Yuxin Liu and Mrs Luping Pan; and my fiancee, Dr. Qian Cao. They are and will be always the source of the motivity for my achievement.

Table of Contents

List of Tables

Chapter 2

Chapter 4

Chapter 5

List of Figures

Chapter 1

Chapter 2

Chapter 3

Chapter 4

Chapter 5

Abbreviations

CO_2	Carbon dioxide
CH_4	Methane
CH_3OH	Methanol
C_4H_9OH	n-butanol
CH_3COOH	Acetic acid
$C_8H_{16}O_{10}Rh_2$	Rhodium(II) acetate
$CuCl_2$	Copper(II) chloride
Cu_2O	Copper(I) oxide
DR UV-Vis	Diffuse reflective ultraviolet-visible spectroscopy
FID	Flame ionization detector
GC	Gas chromatography
ICP-MS	Inductively coupled plasma mass spectrometry
TiO_2	Titanium dioxide
$Ti(OC_4H_9)_4$	Titanium(IV) n-butoxide
TEM	Transmission electron microscopy
UV	Ultraviolet
XRD	X-ray diffraction
XPS	X-ray photoelectron spectroscopy
$ZnCl_2$	Zinc chloride
ZnO	Zinc oxide

Addendum

The author of this thesis has made contributions to three published papers during the PhD study. These papers are:

Pei-Yin Liou[a], Shang-Chien Chen[a], Jeffrey Chi-Sheng Wu*[a], **Dong Liu**[b], Sarah Mackintosh[b], Mercedes Maroto-Valer[b], Robert Linforth[c]. (2011). Photocatalytic CO_2 reduction using an internally illuminated monolith photoreactor. *Energy & Environmental Science* **4**: 1487.

Jeannie Ziang Yie Tan, Yolanda Fernandez Diez, **Dong Liu**, Mercedes Maroto-Valer, Xiwen Zhang*, Juncao Bian. (2012). Photoreduction of CO_2 using copper-decorated TiO_2 nanrod films with localized surface Plasmon behavior. *Chemical Physics Letters* **531**: 149-154.

Dong Liu[a], Yolanda Fernandez[a,b], Oluwafunmilola Ola[a], Sarah Mackintosh[a], Mercedes Maroto-Valer[a]*, Christopher M. A. Parlett[c], Adam F. Lee[c]*, Jeffrey Chi-Sheng Wu[d]*. (2012). On the impact of Cu dispersion on CO_2 photoreduction over Cu/TiO_2. *Catalysis Communications* **25**: 78-82.

Chapter 1: Introduction

Carbon dioxide (CO_2) is a colourless and odourless gas which serves as the source of carbon for photosynthesis of plants and crops (Song, 2006). Etheridge et al. (1998) measured the historical atmospheric CO_2 concentrations from 1000 to 1997 by analysing the air enclosed in the three ice cores obtained at East Antarctica, and recent (1958-2004) atmospheric CO_2 concentrations were determined by Keeling and Whorf (2005) by using the records from the sites in the air sampling network of Scripps Institution of Oceanography (SIO). It can be seen in Fig. 1.1 that the global atmospheric CO_2 concentration only presented slight variation during the period of a thousand years till 20th century, wherein such concentration only increased from 280 ppm in 1000 to 295 ppm in 1900 (Etheridge et al., 1998). However, the atmospheric CO_2 concentration then rapidly increased through the whole 20th century and reached 377 ppm by 2004 (Keeling and Whorf, 2005). Such rapid increase of the atmospheric CO_2 concentrations was primarily caused by the anthropogenic CO_2 emissions, such as deforestation and burning fossil fuels (NASA, 2011a). The rapid increase of the atmospheric CO_2 concentration is an issue of great concern as it is related to the increase of global temperature in recent decades (Fig. 1.2) (NASA, 2011b).

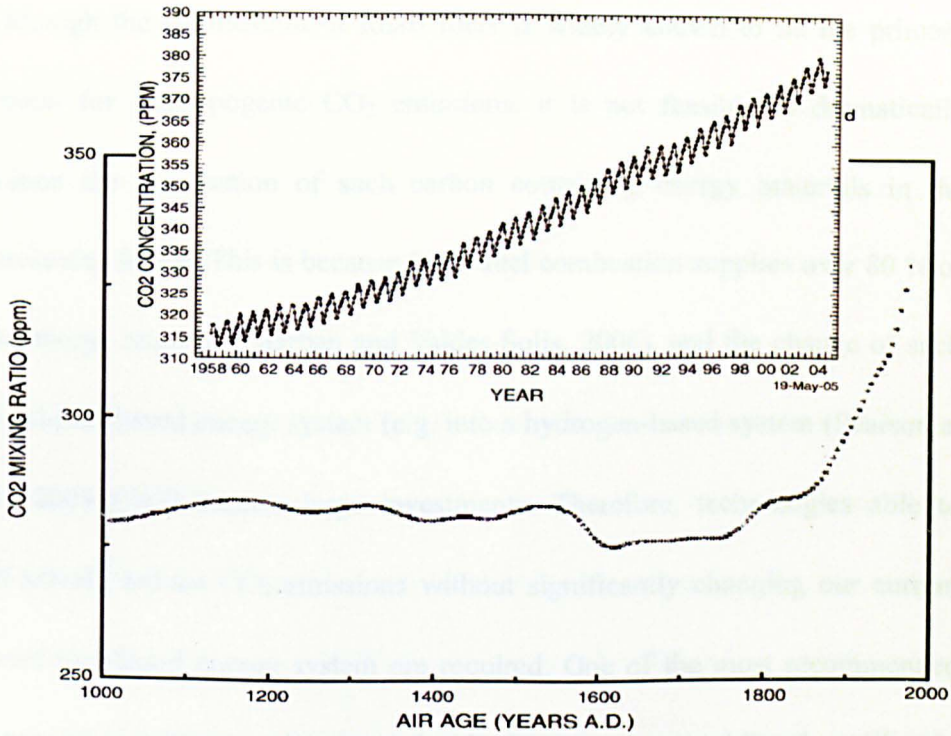

Fig. 1.1: Atmospheric CO_2 concentrations during 1000-2004 based on the analysis of ice cores for 1000-1997 (Etheridge et al., 1998) and the actual atmospheric CO_2 concentrations during 1958-2004 (Keeling and Whorf, 2005).

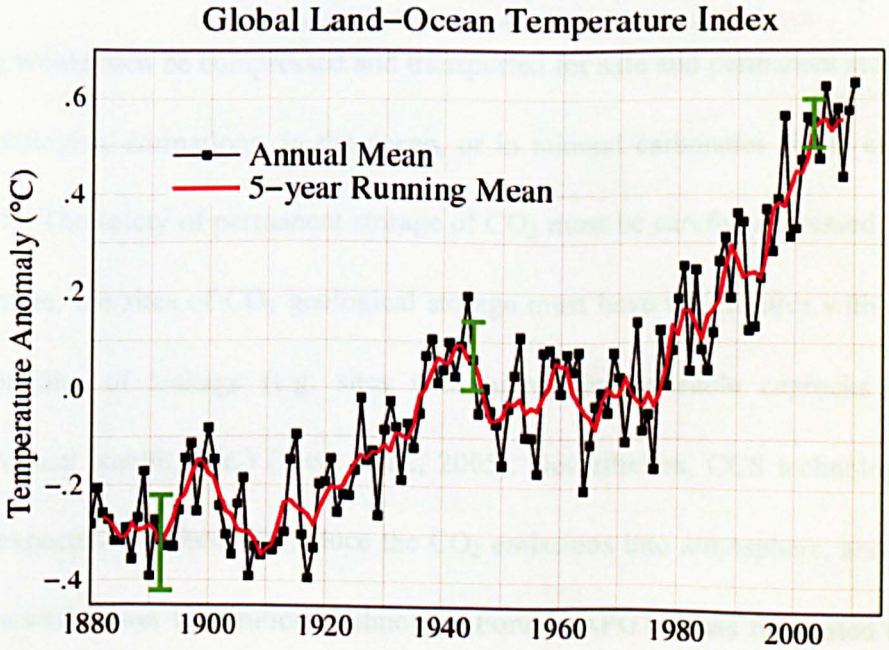

Fig. 1.2: Global temperature change from 1880 to 2010 (NASA, 2011b).

Although the combustion of fossil fuels is widely known to be the primary reason for anthropogenic CO_2 emissions, it is not feasible to dramatically reduce the combustion of such carbon containing energy materials in the foreseeing future. This is because fossil fuel combustion supplies over 80 % of the energy required (Marban and Valdes-Solis, 2006), and the change of such fossil-fuel-based energy system (e.g. into a hydrogen-based system (Pearson et al., 2009)) will require large investments. Therefore, technologies able to effectively reduce CO_2 emissions without significantly changing our current fossil-fuel-based energy system are required. One of the most recommended strategies to achieve such purpose by the Intergovernmental Panel on Climate Change (IPCC) is carbon capture and storage (CCS) (Metz et al., 2005). Such approach can be applied to large point sources of CO_2 (e.g. large fossil fuel energy facilities) to capture the emitted CO_2 (Metz et al., 2005). The captured CO_2 would then be compressed and transported for safe and permanent storage in geological formations, in the ocean, or in mineral carbonates (Metz et al., 2005). The safety of permanent storage of CO_2 must be carefully assessed. For example, the sites of CO_2 geological storage must have the features with low probability of leakage (e.g. sites with highly impermeable caprocks and geological stability etc.) (Metz et al., 2005). Nevertheless, CCS technologies are expected to effectively reduce the CO_2 emissions into atmosphere, and the Advanced Power Generation Technology Forum (APGTF) has forecasted that CCS would make a major contribution in UK to the targets of 80 % greenhouse

gas emissions reduction by 2050 (APGTF, 2011). Meanwhile, the application of CCS will also produce large amounts of concentrated CO_2. Other than transporting CO_2 for storage, such CO_2 can be used for other purpose, e.g. the production of fuel materials (Jiang et al., 2010).

The utilization of the captured CO_2 to synthesize fuel materials is an attractive option, because this approach can substantially reduce CO_2 emissions, lower the fossil fuel consumption, and sustainably supply energy for our society (Arakawa, 2001; Centi and Perathoner, 2009; Indrakanti et al., 2009; Mikkelsen et al., 2010; Jiang et al., 2010). However, as shown in Fig. 1.3, CO_2 is clearly a highly stable molecule. Consequently, the conversion of CO_2 into any fuel material must require substantial input of energy (Jiang et al.. 2010).

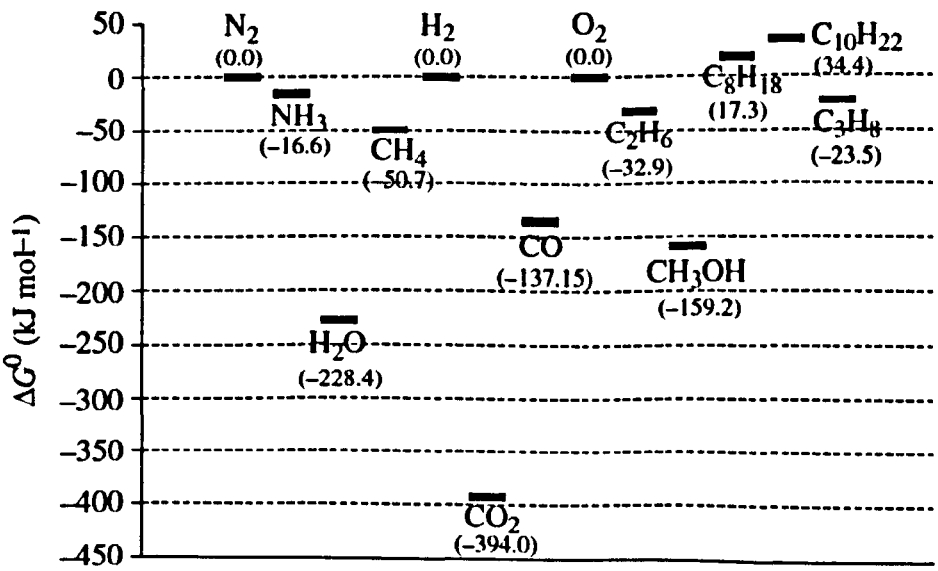

Fig. 1.3: Gibbs free energy of formation for selected chemicals (Jiang et al., 2010).

To avoid net CO_2 emissions, the energy input for the CO_2 conversion into fuel materials must come from renewable source (e.g. solar and wind) (Metz et al., 2005). A series of techniques for CO_2 conversion into fuel materials has been developed. For example, CO_2 can be electrochemically reduced into hydrocarbons, such as methane and ethylene. Hori et al. (1985, 1986) reported that such reactions could occur at a copper foil electrode with current density of 5-10 mA/cm^2 and current efficiency up to 69 % at 0 °C (reactions 1.1 and 1.2). Another technique is to react CO_2 directly with H_2 under suitable conditions (e.g. high pressure to compensate for the negative value of Gibbs free energy to initiate the reaction) to produce methanol (Xu and Ja. 1996).

$$CO_2 + 8H^+ + 8e^- \rightarrow CH_4 + 2H_2O \qquad E_0 = 0.169 \text{ V vs. NHE} \qquad \text{Reaction 1.1}$$

$$2CO_2 + 12H^+ + 12e^- \rightarrow C_2H_4 + 4H_2O \qquad E_0 = 0.079 \text{ V vs. NHE} \qquad \text{Reaction 1.2}$$

The standard potentials (E_0) were calculated by Gattrell et al. (2006) using formation energies from (Dean, 1999).

The processes of converting CO_2 into fuel material can meet the requirement of avoiding net CO_2 emissions if their desired energy input (e.g. electricity) and reactants (e.g. H_2) could be generated by using a renewable energy source (e.g. using solar energy to generate electricity or H_2). Another attractive way to achieve renewable CO_2 conversion into fuel material is the direct utilization of renewable energy to induce such CO_2 conversion. One of the techniques that can achieve such purpose is CO_2 photoreduction with H_2O by using a

semiconductor as the photocatalyst. The primary energy input for this technique is from light. However, although CO_2 photoreduction has attracted a lot of interest in recent years, this technique is still not practical for industrial use at the current stage because the effective photocatalyst for CO_2 photoreduction has not been well developed. The current photocatalysts for such reaction are all suffering with relatively low efficiency and poor utilization of solar energy. This work focused on the improvement on the efficiency of the semiconductor photocatalyst for CO_2 photo-reduction. The further review on CO_2 photoreduction and detailed objectives of this study are presented in Chapter 2.

References

Advanced Power Generation Technology Forum (APGTF). (2011). *APGTF updated strategy for carbon capture and storage*. (Online). APGTF. Available at: <http://www.apgtf-uk.com/index.php?option=com_docman&Itemid=137> (Accessed Aug. 2011).

Arakawa, H. (2001). Catalysis research of relevance to carbon management: progress, challenges, and opportunities. *Chemical Reviews* **101**: 953-996.

Centi, G., Perathoner, S. (2009). Opportunities and prospects in the chemical recycling of carbon dioxide to fuels. *Catalysis Today*: **148**. 191-205.

Dean, J. A. (1999). *Lange's handbook of chemistry*. McGraw-Hill, New York.

Etheridge, D. M., Steele, L. P., Langenfelds, R. L., Francey, R. J., Barnola, J. M., Morgan, V. I. (1998). *Historical CO_2 record from the Law Dome DE08, DE08-2, and DSS ice cores*. (Online) Carbon Dioxide Information Analysis Center (CDIAC). Available at: <http://cdiac.ornl.gov/trends/co2/graphics/lawdome.smooth75.gif> (Accessed Aug. 2011).

Gattrel, M., Gupta, N., Co, A. (2006). A review of the aqueous electrochemical reduction of CO_2 to hydrocarbons at copper. *Journal of Electroanalytical Chemistry* **594**: 1-19.

Hori, Y., Kikuchi, K., Suzuki, S. (1985). Production of CO and CH_4 in electrochemical reduction of CO_2 at metal electrodes in aqueous hydrogencarbonate solution. *Chemistry Letters*: 1695.

Hori, Y., Kikuchi, K., Murata, A. Suzuki, S. (1986). Production of methane and ethylene in electrochemical reduction of carbon dioxide at copper electrode in aqueous hydrogencarbonate solution. *Chemistry Letters*: 897.

Indrakanti, V. P., Kubicki, J. D., Schobert, H. H. (2009). Photoinduced activation of CO_2 on Ti-based heterogeneous catalysts: Current state, chemical physics-based insights and outlook. *Energy & Environmental Science* **2**: 745-758.

Jiang, Z., Xiao, T., Kuznetsov, V. L., Edwards, P. P. (2010). Turning carbon dioxide into fuel. *Philosophical Transaction of the Royal Society A* **368**: 3343-3364.

Keeling, C. D., Whorf, T. P. (2005). *Monthly atmospheric CO_2 records from sites in the SIO air sampling network.* (Online) Carbon Dioxide Information Analysis Center (CDIAC). Available at: <http://cdiac.ornl.gov/trends/co2/graphics/mlo145e_thrudc04.pdf> (Accessed Aug. 2011).

Marban, G., Valdes-Solis, T. (2006). Towards the hydrogen economy? *International Journal of Hydrogen Energy* **32**: 1625-1637.

Metz, B., Davidson, O., de Coninck, H. C., Loos, M., Meyer, L. A. (2005). *IPCC Special Report on Carbon Dioxide Capture and Storage.* Cambridge University Press. United Kingdom and New York.

Mikkelsen, M., Jorgensen, M., Krebs, F. C. (2010). The teraton challenge: A review of fixation and transformation of carbon dioxide. *Energy & Environmental Science* **3**: 43-81.

NASA (2011a). *Carbon dioxide concentration.* (Online). NASA. Available at: <http://climate.nasa.gov/keyIndicators/> (Accessed Aug. 2011).

NASA (2011b). *GISS surface temperature analysis.* (Online). NASA. Available at: <http://data.giss.nasa.gov/gistemp/graphs/> (Accessed Aug. 2011).

Pearson, R. J., Turner, J. W. G., Peak, A. J. (2009). *Gasoline-ethanol-methanol tri-fuel vehicle development and its role in expediting sustainable organic fuels for transport.* (Online) Institution of Mechanical Engineers. Available at: <http://www.grouplotus.com/mediagallery/image/1002548.pdf> (Accessed Aug. 2011).

Song, C. S. (2006). Global challenges and strategies for control, conversion and utilization of CO_2 for sustainable development involving energy, catalysis adsorption and chemical processing. *Catalysis Today*: 2-32

Xu, X., Ja, M. (1996). Mitigation of CO_2 by chemical conversion: Plausible chemical reactions and promising products. *Energy and Fuels* **10**: 301.

Chapter 2: Literature review

This chapter reviews the state of the art in CO_2 photoreduction. The concept of CO_2 photoreduction is presented in Section 2.1, while the mechanism is described in Section 2.2. Section 2.3 reviews the use of TiO_2 as photocatalyst for CO_2 photoreduction and the approaches to improve its performance. Section 2.4 introduces the analytical techniques that can be used for TiO_2 characterization in this work. Finally, Section 2.5 describes the aim and objectives of this study.

2.1 Utilizing CO_2 to produce fuel

Nature can maintain the equilibrium between carbon dioxide (CO_2) release (e.g. via animal and plant respiration, and volcanic activity) and fixation (e.g. via photosynthesis by plants) (EPA, 2011). However, anthropogenic CO_2 emissions (e.g. fossil fuel combustion) have disturbed such equilibrium, and became the main contributors to global warming (Metz et al., 2005; Vernon et al., 2011). To mitigate such problem, IPCC recommended to develop and adopt carbon capture and storage (CCS) (Metz et al., 2005). These technologies are expected to not only effectively reduce anthropogenic CO_2 emission to atmosphere, but also provide an abundant source of concentrated CO_2 (Jiang et. al., 2010).

Since CO_2 presents the advantages of being abundant (due to the use of CCS techniques) and non-toxic, the development of effective approaches for CO_2 utilization is worthy (Jiang et al., 2010; Mikkelsen et al., 2010). One of the most attractive options of CO_2 utilization is for the production of fuel. However, as shown in Fig. 1.3, the low energy level of CO_2 determines that any process to convert CO_2 requires a large energy input (Sakakura et al., 2007; Jiang et. al., 2010). As a result, the traditional industrial utilization of CO_2 for chemical synthesis normally requires high temperature, high pressure, and additional organic material as reactant (e.g. industrial urea production requires temperature to be 170–200 °C, pressure to be 13–30 MPa, and ammonia as reactant (Hamidipour et al., 2005)). In contrast, the novel-developed CO_2 utilization approaches shall avoid any net CO_2 emission (Metz et al., 2005). In other words, the energy input for CO_2 conversion must be from renewable energy sources, such as wind or solar. Among these options, the direct use of solar energy to convert CO_2 into fuel is an attractive option (de_Richter and Caillol, 2011). Photocatalytic reduction of CO_2 by using semiconductor as photocatalyst is a process that can achieve such purpose. This technique is able to convert CO_2 in the presence of water (H_2O) into fuel (e. g. CH_3OH and CH_4) at ambient conditions, wherein the primary energy to induce this reaction is from light (Inoue et al., 1979; Tan et al., 2006; Wu et al., 2005; de_Richter and Caillol, 2011).

2.2 Mechanism of CO_2 photoreduction

The first CO_2 photoreduction was reported by Inoue et al. (1979), where CO_2 was photo-reduced in aqueous solution into organic materials, such as formaldehyde (HCHO), formic acid (HCOOH), methanol (CH_3OH), and methane (CH_4) by using various semiconductor photocatalysts including tungsten trioxide (WO_3), titanium dioxide (TiO_2), zinc oxide (ZnO), cadmium sulfide (CdS), gallium phosphide (GaP), and silicon carbide (SiC).

The basic mechanism of CO_2 photoreduction in the presence of H_2O is schematically described in Fig. 2.1. Similar to other photocatalysis processes (e.g. photocatalytic degradation of contaminants and photocatalytic water splitting), CO_2 photoreduction makes use of a semiconductor as a photocatalyst to promote the reaction in the presence of light (Turchi and Ollis, 1990; Bhatkhande et. al., 2001; Ni et. al., 2007). Firstly, the semiconductor is exposed to light and absorbs photon energy (hv). Then, if the absorbed photon energy is sufficient to overcome the band-gap of the semiconductor (the void energy region that extends from the top of the filled valance band to the bottom of the vacant conduction band (Usubharatana et al., 2006)), the electrons (e^-) in the valence band (VB) can be excited and transferred to the conduction band (CB), leaving positively charged holes (h^+) in the VB. These photo-generated electron and hole pairs (e^-/h^+) may move to the surface of the semiconductor

and react with the adsorbed species (e. g. CO_2, H_2O) to initiate the CO_2 photoreduction.

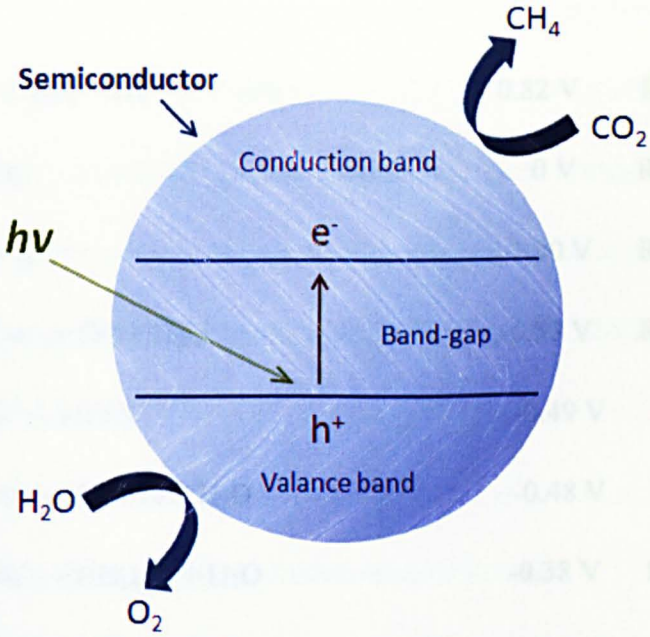

Fig. 2.1: Mechanism of photocatalytic reduction of CO_2.

It should be noted that the photo-generation of electron and hole pairs is a reversible process, and such electron and hole pairs may experience bulk or surface recombination emitting photon and heat energy. Such recombination process can prevent electron and hole pairs participating in reactions for CO_2 photoreduction. Therefore, the decrease of the electron and hole recombination rate can increase the life-time of these charge carriers and significantly improve the efficiency of CO_2 photoreduction (Indrakanti et al., 2009).

The possible reactions involved in CO_2 photoreduction with H_2O and their corresponding redox potentials with respect to NHE (normal hydrogen electrode) are shown in Reactions 2.1-2.8 (Indrakanti et al., 2009):

$H_2O + 2h^+ \rightarrow 1/2O_2 + 2H^+$	0.82 V	Reaction. 2.1
$2H^+ + 2e^- \rightarrow H_2$	0 V	Reaction. 2.2
$CO_2 + e^- \rightarrow CO_2^{\cdot}$	-1.90 V	Reaction 2.3
$CO_2 + 2H^+ + 2e^- \rightarrow CO + H_2O$	-0.53 V	Reaction 2.4
$CO_2 + H^+ + 2e^- \rightarrow HCO_2^-$	-0.49 V	Reaction 2.5
$CO_2 + 4H^+ + 4e^- \rightarrow HCHO + H_2O$	-0.48 V	Reaction 2.6
$CO_2 + 6H^+ + 6e^- \rightarrow CH_3OH + H_2O$	-0.38 V	Reaction 2.7
$CO_2 + 8H^+ + 8e^- \rightarrow CH_4 + 2H_2O$	-0.24 V	Reaction 2.8

It can be seen that CO_2 photoreduction with H_2O requires both multi-electron transfer reactions (Reactions 2.4 – 2.8) and water oxidation (Reaction 2.1) to occur simultaneously (Jiang et al. 2010). Wherein, the band-edge energy positions of the VB and CB of the semiconductor are critical to determine whether these reactions can be initiated. The band-edge position of the VB must be sufficiently positive to allow photo-generated hole to initiate the necessary oxidation (e. g. more positive than the redox potential of H_2O decomposition, 0.82 V, Reaction 2.1). Meanwhile, the band-edge position of the CB must be sufficiently negative to allow photo-generated electron to

participate in the reduction reactions (e. g. more negative than redox potential of CO_2 reduction into CH_4, -0.24 V, Reaction 2.8). Moreover, based on the redox potentials of equations 2.3–2.8, CO_2 photoreduction may be more favourable to be a multi-electronic process which yields the final product of CH_4 through different intermediates ($CO_2 \rightarrow HCOOH \rightarrow HCHO \rightarrow CH_3OH \rightarrow CH_4$), because Reactions 2.4–2.8 require much less energy per electron transferred as compared to mono-electron process (Reaction 2.3) (Ishitanij et al., 1993; Yahaya et al., 2004; Hwang et al., 2005; Tan et al., 2006; Yang et al., 2009; Dey, 2007).

2.3 TiO_2 as a catalyst for CO_2 photoreduction

Based on the description of the CO_2 photoreduction mechanism in Section 2.2, it can be realized that the semiconductor photocatalyst is the key for this process. The suitable semiconductor photocatalyst for CO_2 photoreduction should not only provide appropriate VB and CB with suitable energy positions that can induce water decomposition and CO_2 reduction reactions simultaneously, but also have the properties of chemical stability and low cost (Bhatkhande et al., 2001). To combine all of these factors into consideration, titanium dioxide (TiO_2), the most widely used semiconductor in world, is one of the best options to act as photocatalyst for CO_2 photoreduction (Fujishima et al., 2000; Ni et al., 2007; Chen and Mao, 2007; Nguyen and Wu, 2008a;

Indrakanti et al., 2009; Jiang et al., 2010).

Two different crystalline structures of TiO_2, rutile and anatase, are commonly used in photocatalysis, with anatase showing a higher photocatalytic activity (Augustynski, 1993; Sclafani, 1996). This may be because of the relatively larger band-gap of anatase (3.2 eV) than that of rutile (3.0 eV), which allows anatase to provide more sufficiently negative and positive redox potentials in CB and VB during photocatalysis (Usubharatana et al., 2006). Hence, most of the TiO_2 reported to successfully initiate CO_2 photoreduction had the crystalline structure of anatase (Tseng et al.,2002; Yahaya et al., 2004; Wu et al., 2005; Nguyen and Wu, 2008a; Koci et. al. 2009, 2010; Varghese et al., 2009; Zhang et al., 2009a; Zhao et al., 2009; Luo et al., 2011). The inherent properties of TiO_2 anatase are listed in Table 2.1. It can be seen that the VB and CB positions of TiO_2 anatase make it possible to induce simultaneously water decomposition (0.82 V, Reaction. 2.1) and CO_2 reduction into CH_4 (-0.24 V, Reaction 1.8).

Table 2.1: Band-gap, threshold wavelength, and VB and CB positions of anatase (Xu and Schoonen, 2000).

Band-gap	3.2 eV
Threshold wavelength	387.50 nm
VB position (NHE)	2.91 V
CB position (NHE)	-0.29 V

However, there are still disadvantages hindering the use of TiO_2 as effective catalyst for CO_2 photoreduction. Firstly, the efficiency of CO_2 photoreduction by using TiO_2 is still too low for practical application. Indrakanti et al. (2009) summarized the highest rates of CO_2 photoreduction obtained by using TiO_2 as catalysts in published works (Fig. 2.2). It can be seen that even the best work (conducted by Ikeue et al. (2001)) could only achieve a CO_2 conversion rate at around 26 $\mu mol \cdot g_{-TiO2}^{-1} \cdot hr^{-1}$ (Indrakanti et. al., 2009). Such reaction efficiency is obviously too low for practical application, and therefore, it is necessary to improve the activity of TiO_2 for CO_2 photoreduction.

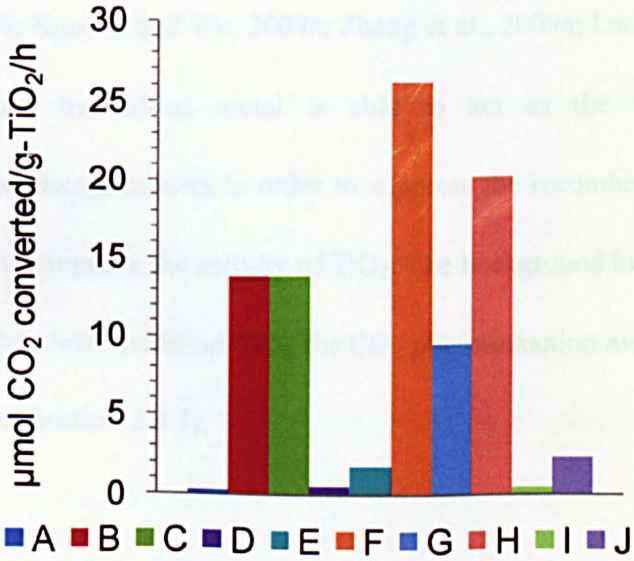

Fig. 2.2: The highest specific rates of CO_2 photoreduction obtained by using Ti-based catalysts in the selected articles (Indrakanti et al., 2009). A: Yamashita et al., 1994a, B: Anpo et al., 1997, C: Yamashita et al., 1998, D: Kaneco et al., 1998, E: Kaneco et al., 1999, F: Ikeue et al., 2001, G: Ikeue et al., 2002a, H: Tseng et al., 2002, I: Wu et al., 2005, J: Nguyen and Wu, 2008a.

Another problem when using TiO_2 is its relatively large band-gap (3.2 eV, as shown in Table 2.1) that can only be effectively excited by ultraviolet (UV) light (wavelength: 400-100 nm, corresponding to photon energies of 12.40-3.1 eV). As only small fraction of solar spectrum is within the UV region (no higher than 3%), there is a need to modify the light absorption range of TiO_2 to efficiently utilize solar energy for CO_2 photoreduction.

One of the most widely used methods to improve the activity of TiO_2 for CO_2 photoreduction is by modifying TiO_2 with metal (Choi et al., 1994; Linsebigler et al., 1995; Kohno et al., 1999; Xie et. al., 2001; Tseng et. al. 2002, 2004; Wu and Chen, 2004; Nguyen and Wu, 2008a; Zhang et al., 2009a; Luo et al., 2011). This is because the added metal is able to act as the traps of the photo-generated charge carriers in order to suppress the recombination rate of electron/hole and improve the activity of TiO_2. The background knowledge and utilization of the metal modified TiO_2 for CO_2 photoreduction are reviewed in the next section (Section 2.3.1).

2.3.1 Metal modification on TiO_2

To improve the activity of TiO_2 by metal modification, certain amount of metal is added to the surface of TiO_2 (Linsebigler et al., 1995). Such added metal has two ways to modify TiO_2: one of them is to load the metal on the TiO_2 surface,

and another one is to dope the metal into the lattice of the TiO_2 surface. These two types of metal modification have different mechanisms to affect the TiO_2 activity, as described below.

2.3.1.1 Metal loading on TiO_2 surface

When a metal is loaded on TiO_2, the added metal is deposited on the TiO_2 surface and not incorporated into the TiO_2 lattice. The way for such loaded metal to improve the activity of TiO_2 for CO_2 photoreduction is to function as the electron trap. The key point for this phenomenon is believed to be the formation of the Schottky barrier between the loaded metal and its TiO_2 support (Linsebigler et al., 1995). Linsebigler et al. (1995) have clearly illustrated the mechanism of the formation of a Schottky barrier in one of their publications (Fig. 2.3). If electrically neutral and isolated from each other, the metal and n-type semiconductor (e.g. TiO_2) have different Fermi level positions (E_f: the value which corresponds to the energy halfway between the conduction and valence band edges) (Rhoderick and Williams, 1988; Linsebigler et al., 1995; Xu and Schoonen, 2000). When these two materials are in contact with each other and the work function of metal (Φ_m, energy required to move an electron from the Fermi level into vacuum) is higher than that of the semiconductor (Φ_s), the electron will migrate from semiconductor to metal until the two Fermi levels are aligned as shown in Fig 2.3. This causes a

negative charge carrier accumulation on the outer surface region of the semiconductor. To preserve electrical neutrality, a positive space charge layer (depletion layer) is formed just within semiconductor causing a bending of bands upward toward the surface. As a result, a barrier is formed at the metal-semiconductor interface preventing any further electron migration between the loaded metal and semiconductor. This barrier is called the Schottky barrier (Linsebigler et al., 1995).

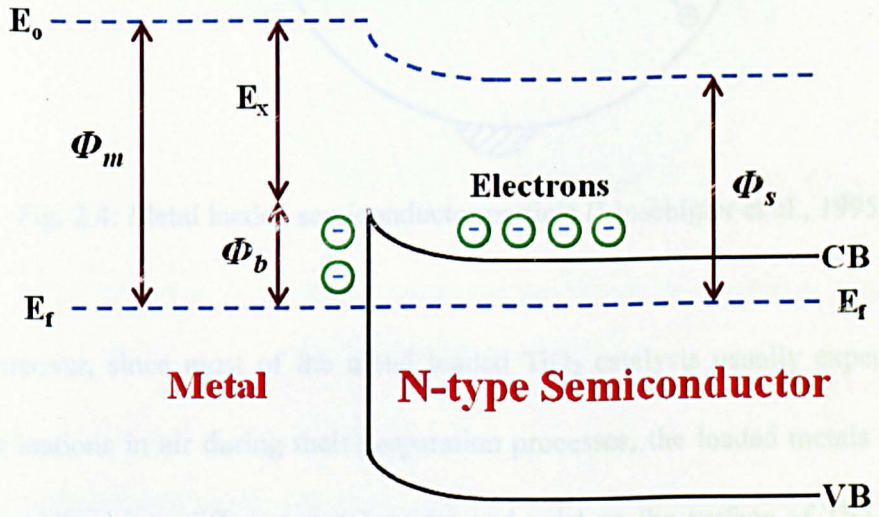

Fig. 2.3: Schematic of Schottky barrier, modified from Linsebigler et al. (1995).

Therefore, the procedure of the metal loaded TiO_2 for photocatalysis can be described by Fig. 2.4, wherein the semiconductor support (e. g. TiO_2) firstly absorbs photon energy (hv) to generate electron and hole pairs, then the electron will migrate to the loaded metal and be trapped by Schottky barrier. This process can suppress the recombination rate of electron/hole and increase

the possibility for those charge carriers to react with the adsorbing species on this metal loaded semiconductor photocatalyst.

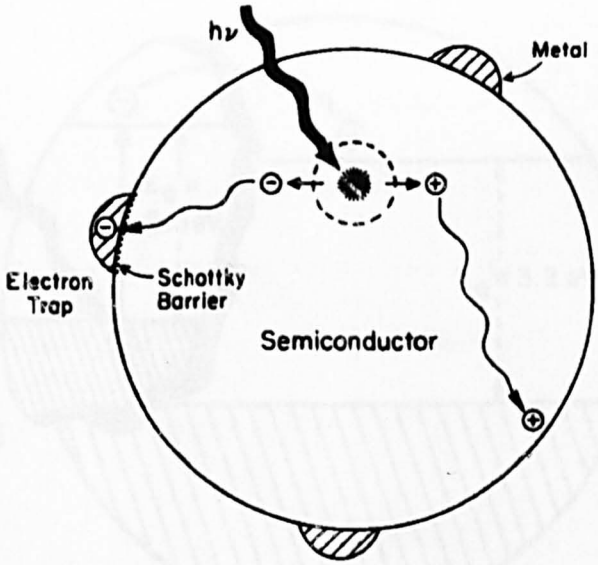

Fig. 2.4: Metal loaded semiconductor particle (Linsebigler et al., 1995).

Moreover, since most of the metal loaded TiO_2 catalysts usually experience calcinations in air during their preparation processes, the loaded metals could be oxidized into different metal oxides and exist on the surface of TiO_2 with different chemical states (e. g. the loaded Cu to be Cu_2O or CuO (Tseng et al., 2002; Yang et. al., 2011)). It is interesting to note that some of these loaded metal oxides, can act as another semiconductor material located on the TiO_2 surface, e.g. both Cu_2O and CuO are also widely used semiconductor materials (Xu and Schoonen, 2000; Hara et al., 1998). In this case, such metal oxide loaded TiO_2 can be considered to be a composite semiconductor catalyst, wherein the charge carriers can transfer from one semiconductor to another due

to the different absolute positions of CB and VB of these two semiconductor materials (e.g. CdS loaded TiO_2, Fig. 2.5, (Linsebigler et al., 1995)).

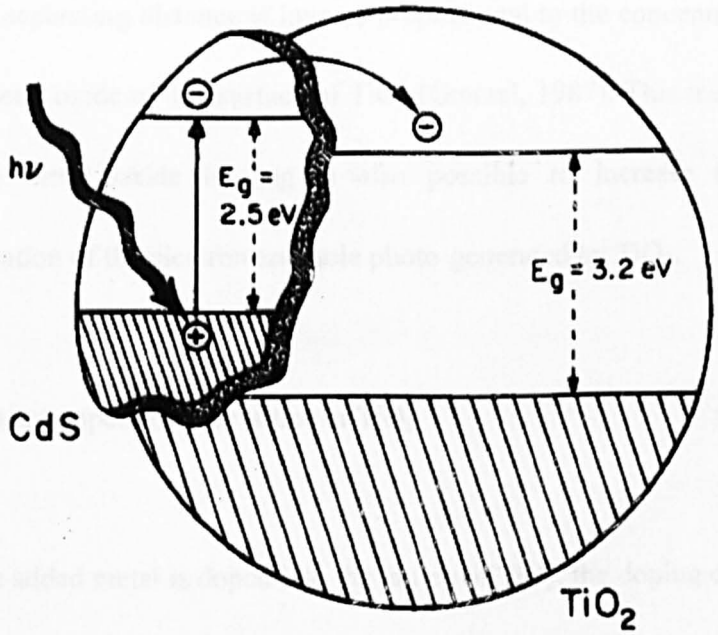

Fig. 2.5: Photoexcitation in composite semiconductor photocatalyst (Linsebigler et al., 1995).

The loaded metal oxide can act as electron and hole traps, depending on the relative positions of the CB and VB. For example, the photo-generated electron on the CB of TiO_2 can transfer to that of the loaded metal oxide if the CB position of TiO_2 is relatively higher than that of the loaded metal oxide. And such electron transition can allow the loaded metal oxide to act as electron trap and improve the activity of TiO_2 (Linsebigler et al., 1995). Meanwhile, the loaded metal oxide can also trap the photo-generated hole if its VB is relatively higher than that of TiO_2. Such phenomenon allows the loaded metal oxide to

trap both electron and hole at the same time. But the trapped electron and hole may recombine, where the rate of this trapped charge carrier recombination is determined by the average distance separating the trapped electron and hole, and such separating distance is inverse proportional to the concentration of the loaded metal oxide on the surface of TiO_2 (Gratzel, 1987). This means that the excessive metal oxide loading is also possible to increase the rate of recombination of the electron and hole photo-generated by TiO_2.

2.3.1.2 Metal doped into the lattice of TiO_2

When the added metal is doped into the lattice of TiO_2, the doping can be either substitutional or interstitial. Both of these two types of doping can affect the lattice spacing of TiO_2.

Substitutional metal doping means that some of the Ti^{4+} ions in the lattice of TiO_2 are replaced by the doped metal ions (or atoms). Such doping is likely when the ionic (or atomic) radius of the dopant is comparable (normally when the size difference is not higher than 15 %) to that of the Ti^{4+} ion (Barrett and Massalski, 1980; Li et al., 2005). Substitutional metal can either decrease or increase the lattice spacing of TiO_2, depending on valency and the ionic (or atomic) size of the doped metal (Barrett and Massalski, 1980).

On the other hand, interstitial metal doping indicates that the ions (or atoms) of the doped metal are accommodated in the interstices of the lattice of TiO_2. Because the dopant is doped into the interstices of the lattice of TiO_2, interstitial metal doping can always increase the lattice spacing of TiO_2 (Barrett and Massalski, 1980).

Metal doping is reported to be able to improve the activity of TiO_2 because such doping can introduce additional energy level into the band-gap of TiO_2, which is able to act as the trap site of charge carriers and increase the separation of electron and hole (Choi et al., 1994). Choi et al. (1994) explained that that when the doped metal (M^{n+}) had a energy level of $M^{n+}/M^{(n-1)+}$ below the CB edge of TiO_2, the metal dopant would be able to act as electron trap (Reaction 2.9). Conversely, if the energy level of $M^{n+}/M^{(n+1)+}$ lay above the VB edge of TiO_2, the metal dopant would be able to act as hole trap (Reaction 2.10) (Choi et al., 1994).

$$M^{n+} + e^- \rightarrow M^{(n-1)+} \qquad \text{Reaction 2.9}$$

$$M^{n+} + h^+ \rightarrow M^{(n+1)+} \qquad \text{Reaction 2.10}$$

However, it must be noted that the trapped charge carriers may recombine with the other electrons and holes photo-generated by TiO_2 (Reaction 2.11 and 2.12) (Choi et al., 1994).

$M^{(n-1)+} + h^+ \rightarrow M^{n+}$ Reaction 2.11

$M^{(n+1)+} + e^- \rightarrow M^{n+}$ Reaction 2.12

In this case, the energy level introduced by metal doping will act as the charge carrier recombination center to decrease the TiO_2 activity. For example, Zhu et al. (2006) reported that Cr^{3+} dopant was able to trap the photo-generated hole from TiO_2 and improve the TiO_2 photo-activity due to the energy level of Cr^{3+}/Cr^{4+} lying above the VB edge of TiO_2 ($Cr^{3+} + h^+ \rightarrow Cr^{4+}$). But they also reported that excessive Cr^{3+} doping could deactivate TiO_2 because the trapped hole might react with the electron photo-generated by TiO_2 ($Cr^{4+} + e^- \rightarrow Cr^{3+}$), in which Cr^{3+} act as an charge carrier recombination center and, therefore, decrease the photo-activity of TiO_2. Hence, the ratio of the doped metal must be carefully considered, because the presence of the metal dopant can simultaneously suppress and enhance the recombination of the photo-generated electron and hole within TiO_2. The optimal doping ratio should be able to achieve the balance on these two opposite effects and lead to the maximum promotion on the photo-activity of TiO_2.

It is worthy to note that one of the most promising methods to determine if the added metal is loaded on TiO_2 surface or doped into the TiO_2 lattice is to use powder XRD analysis. The theory of powder XRD and the examples to determine how the metal is added to TiO_2 are presented in Section 2.4.1.

2.3.1.3 Metal modified TiO_2 for CO_2 photoreduction

Published works reporting the utilization of metal modified TiO_2 for CO_2 photoreduction are summarized in Table 2.2. It can be seen that various metals have been proven to be able to improve the activity of TiO_2 for CO_2 photoreduction, including Cu, Pt, Pd, Rh, Fe, and Ag. However, it should be noted that not all the published papers had conclusively clarified whether the added metal was loaded on the TiO_2 surface or doped into the lattice of TiO_2, and in these cases, the term "metal modified TiO_2" is used in Table 2.2. It has also been found that the ratio and chemical state of the added metal can affect the activity and selectivity of TiO_2 for CO_2 photoreduction. These effects are further reviewed in Sections 2.3.1.3.1 and 2.3.1.3.2.

Table 2.2: Summary of the published works on metal modified TiO_2 for CO_2 photoreduction with H_2O.

Catalyst	Experimental conditions and products	Reference
Sol-gel derived TiO_2 with Cu loaded on its surface. The loaded Cu was primarily with chemical state of Cu_2O and the Cu loading ratio ranged from 0.6 wt% to 6.7 wt%.	CH_3OH was the primary product of CO_2 photoreduction conducted in a batch aqueous suspension reactor under 8 W UVC illumination. Cu loading was able to increase the CH_3OH yield with the optimal loading ratio to be 2 wt%.	Tseng et al., 2002

Sol-gel derived Cu loaded TiO_2 supported by mesoporous SiO_2 (P25, mixture of approximately 80 % anatase and 20 % rutile). The loaded Cu was with the chemical state of Cu_2O. The Cu loading ratio was 1.7-25 wt%.	CH_4 was the primary product of CO_2 photoreduction. The experiments were conducted in a continuous-flow reactor illuminated by Xe lamp with wavelength to be 250 nm-400 nm and light intensity to be 2.4 mW/cm^2, wherein H_2O vapour was the reductant. The optimal Cu loading ratio to improve the activity of TiO_2 was 4.25 wt%.	Li et al., 2010
Sol-gel derived Cu modified TiO_2 (anatase) with Cu ratio to be 1-5 wt%. The added Cu was claimed to be with the chemical state of CuO.	The present of CuO increased the total organic carbon (including HCOOH, HCHO, and CH_3OH) production of CO_2 photoreduction. The experiments were conducted in a batch aqueous suspension reactor illuminated by a 250 W Hg lamp. The optimal CuO ratio was 3 wt%.	Yang et al., 2011
Pt modified TiO_2 nano-tube (anatase) prepared by incipient wetness method with Pt ratio to be 0.07-0.21 wt%.	CO_2 photoreduction experiments were conducted in a continuous fixed-bed photo-reactor with H_2O vapour and 300 W Hg lamp illumination. CH_4 was the primary product. The optimal Pt ratio to improve TiO_2 activity was 0.12 w%.	Zhang et al., 2009a

Pd and Ru modified TiO_2 prepared by incipient wetness method. Pd was claimed to be with the chemical states of Pd^0 and Pd_2O.	HCOOH was formed during the CO_2 photoreduction conducted in a batch aqueous suspension with 450 W Xe lamp illumination. The added Pd was able to improve the yields of organic products.	Xie et al., 2001
Rh modified TiO_2, prepared by incipient wetness method.	The presence of 1 wt% Rh selectively improved the production of CH_3OH and HCOOH during CO_2 photoreduction in a batch aqueous suspension reactor under 500 W Xe lamp illumination.	Solymosi et al., 1994
TiO_2 (P25) with Cu and Fe simultaneously loaded on the surface, wherein the chemical states of Cu and Fe were Cu_2O and Fe_2O_3 respectively.	CO_2 photoreduction experiments were conducted in a continuous optical-fiber reactor with H_2O vapour and UVA or UVC illumination (intensity: 225 mW/cm^2). The products were C_2H_6 and CH_4. The Cu/Fe double loaded TiO_2 exhibited better activity than Cu or Fe single loaded TiO_2.	Nguyen and Wu, 2008 (a)
Ag modified TiO_2 (anatase) with Ag loading ratio to be 1-7 wt%.	CO_2 photoreduction experiments were conducted in a batch aqueous suspension reactor illuminated by an 8 W UVC lamp. The primary products were CO, CH_4, and CH_3OH. 7 wt% Ag modified TiO_2 showed the best activity.	Koci et al., 2010

2.3.1.3.1 Effects of metal ratio

There seemed to be optimal metal ratios in most of the studies listed in Table 2.2, wherein the activity of TiO_2 decreased when the metal ratio exceeded such a value (Tseng et al., 2002; Li et al., 2010; Yang et al., 2011; Nguyen and Wu, 2008a). For example, Tseng et al. (2002) reported that the CH_3OH yield from CO_2 photoreduction achieved the maximum value (118.5 $\mu mol/g_{-catalyst}$) when TiO_2 with 2 wt% Cu_2O loaded on its surface was used as catalyst. However, the CH_3OH yield dropped to be 20 $\mu mol/g_{-catalyst}$ when the Cu loading ratio increased up to 6 wt%. The primary reason for such TiO_2 deactivation should be the increase of the rate of the charge carrier recombination caused by the over-increase of the added metal ratio (as described in Section 2.3.1.1 or 2.3.1.2). However, such phenomenon can also be caused by other factors, such as the change of the dispersion of the metal loaded on the surface of TiO_2, as described below.

When metal is loaded on the surface of TiO_2, it is not always uniformly dispersed. It is believed that the over-increase of the metal loading ratio will lead to the aggregation of the loaded metal. Significant aggregation of the loaded metal can be detected by powder XRD (e.g. Fig. 2.6 (Tseng et al., 2002)), or observed directly by TEM (e. g. Fig. 2.7 (Yang et al., 2006)).

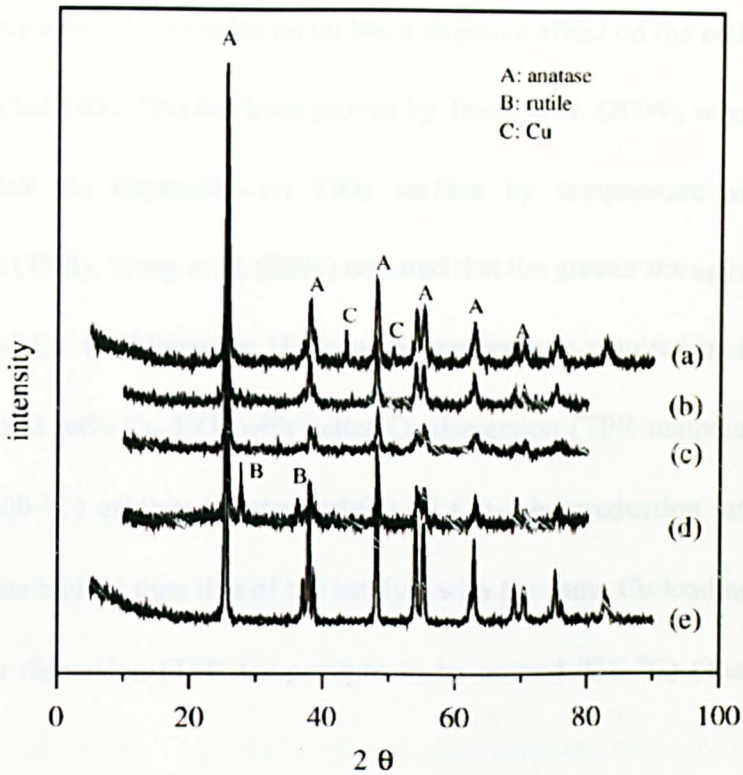

Fig. 2.6: XRD spectra of TiO_2 and Cu/TiO_2. (a): 6.7wt% Cu/TiO_2, (b): 2.0wt% Cu/TiO_2, (c) TiO_2, (d): P25, (e): JRC-2 pure TiO_2, wherein the loaded Cu aggregation of 6.7 wt% Cu/TiO_2 was significant enough to be detectable by XRD (Tseng et al., 2002).

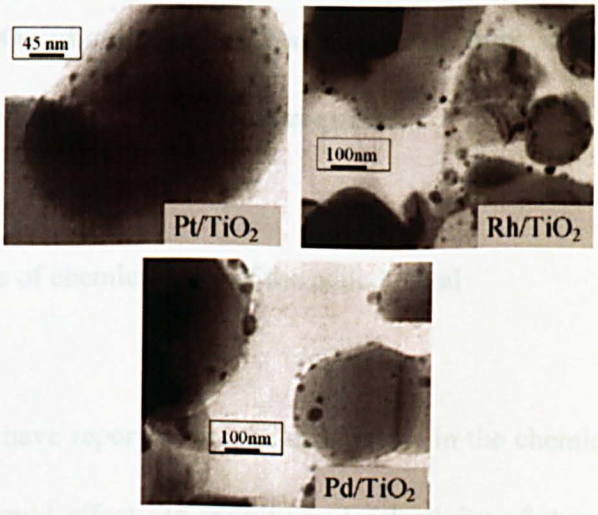

Fig. 2.7: TEM images of 1 wt% metal loaded TiO_2 with aggregated loaded metal (Yang et. al., 2006).

The aggregation of the loaded metal has a negative effect on the activity of the metal loaded TiO_2. This has been proven by Tseng et al. (2004), who evaluated the loaded Cu dispersion on TiO_2 surface by temperature-programmed reduction (TPR). Tseng et al. (2004) reported that the greater the aggregation of the loaded Cu, the higher the H_2-reducing temperature required in TPR. They found that 2 wt% Cu-TiO_2 with better Cu dispersion (TPR temperature to be around 200 °C) exhibited better activity on CO_2 photoreduction into CH_3OH (1.75 times higher) than that of the catalyst with the same Cu loading ratio but lower Cu dispersion (TPR temperature to be around 230 °C) (Tseng et. al., 2004).

Although the negative effect of the loaded metal aggregation on the activity of the metal loaded TiO_2 catalyst had been proven, the precise relation of the loaded metal dispersion versus the metal loaded TiO_2 activity for CO_2 photoreduction has not been fully investigated. More detailed investigation on this field is required.

2.3.1.3.2 Effects of chemical state of the added metal

Several studies have reported that the differences in the chemical states of the added metals could affect the activity and selectivity of the metal modified TiO_2 for CO_2 photoreduction (Kohno et al. 1999, 2001; Tseng et. al., 2004).

For example, Kohno et al. (1999, 2001) studied the effects of the chemical state of Rh on CO_2 photoreduction with H_2 by Rh modified TiO_2 (Rh/TiO_2, Rh loaded or doped not clarified). The results of the CO_2 photoreduction showed that the change of the chemical state of Rh affected both the activity and selectivity of Rh/TiO_2 for CO_2 photoreduction. Fig. 2.8 illustrates the performance of the 1 wt% Rh/TiO_2 catalyst for CO_2 photoreduction in the study of Kohno et al. (1999). The added Rh of such catalyst was originally in the chemical state of Rh^{3+}, and its chemical state was adjusted by H_2 reduction under various temperatures (the higher the reduction temperature, the higher reduction rate of Rh^{3+} into Rh^0). Their results indicated that 1 wt% Rh/TiO_2 exhibited the highest activity towards CO_2 photoreduction with H_2 to CO when the added Rh on TiO_2 was in a mixture of Rh^0 and Rh^{3+} (the optimal ratio of Rh^0/Rh^{3+} was not specified in the study of Kohno et al.). When the Rh was completely reduced into Rh^0, the selectivity of the reaction changed from CO into CH_4 accompanied with a decrease of the total yield of the products from CO_2 photoreduction.

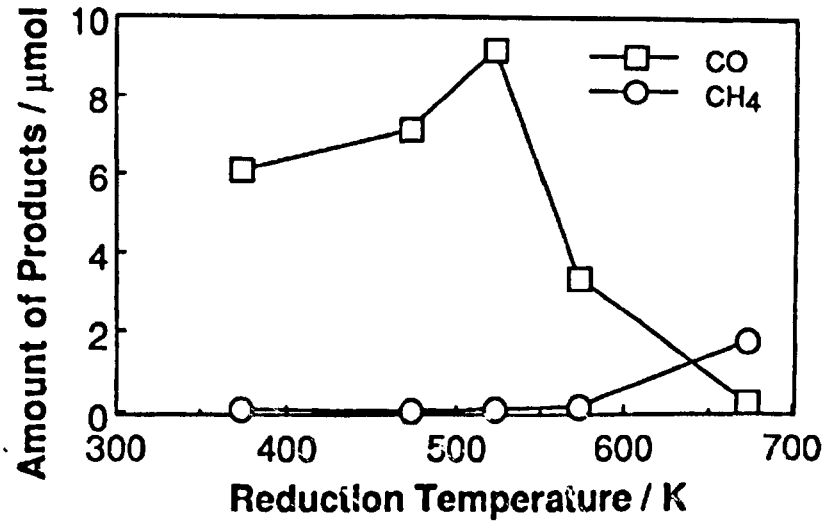

Fig. 2.8: Amount of CO and CH_4 yield after 6-hr photoreaction over 1 wt% Rh/TiO_2 catalysts reduced by H_2 at various temperatures (Kohno et al., 1999).

A similar study on the effects of the chemical state of the added metal was conducted by Tseng et al. (2004) for Cu loaded TiO_2 (Cu/TiO_2). This study reported that the 2 wt% Cu/TiO_2 with the loaded Cu chemical state to be Cu_2O presented significant positive effect to promote CO_2 photoreduction into CH_3OH (yield up to 1000 $\mu mol/g_{-catalyst}$ after 30-hr reaction). However, the activity of the same catalyst decreased significantly (down to 300 $\mu mol/g_{-catalyst}$ after 30-hr reaction) when it was reduced in H_2 at 300 °C for 3 hr (partially reduced Cu_2O into Cu^0) prior to the CO_2 photoreduction reaction. Based on these previous studies (Kohno et al. 1999, 2001; Tseng et. al., 2004), it can be stated that the chemical state of the added metal is also a key to affect the activity of metal modified TiO_2 catalyst for CO_2 photoreduction.

It can be concluded, from the review presented in Section 2.3.1, that metal modification is indeed an effective method to improve the performance of the TiO_2 catalyst for CO_2 photo-reduction. **However, even though extensive studies have been done in this field, most of the previous works simply proved the ability of the metal modification to improve the activity of TiO_2 for CO_2 photoreduction, but did not aim to conduct a systematic investigation to explain the mechanism of the effects of the added metal on TiO_2,** e.g. some of the previous study did not even clarify whether the added metal was loaded or doped to TiO_2 (Zhang et al., 2009a; Koci et al., 2010; Solymosi et al., 1994; Kohno et al., 1999). **Therefore, there is still a need to conduct a systemic investigation on the different effects of the added metal on TiO_2 for CO_2 photoreduction. Such investigation will be helpful to guide the development of the future practical TiO_2 catalysts for CO_2 photoreduction.**

2.3.2 Alternative approaches to improve TiO_2 for CO_2 photoreduction

The previous section (Section 2.3.1) reviewed the approach of using metal modification to improve the performance of TiO_2 for CO_2 photoreduction. There are other alternative approaches for the same purpose. The coming sections review a few of such approaches.

2.3.2.1 Particle size

Particle size is another factor that can affect the activity of TiO_2 catalyst. This is because it can affect the charge carrier recombination of TiO_2 (Zhang et al., 1998). It has been known that the charge carrier recombination can be grouped into two categories: bulk recombination and surface recombination. The bulk recombination is the dominant process in large TiO_2 particles, which can be reduced by decreasing particle size (Serpone et al., 1995). However, when the particle size becomes excessively small, the surface recombination will take the place of bulk recombination to become the dominant factor, because the electron and hole pairs of the ultrafine TiO_2 particle are generated sufficiently close to the surface, and they can quickly reach the surface of the TiO_2 and undergo rapid surface recombination (Serpone et al., 1995). Therefore, an optimal particle size of TiO_2 catalyst exists for the maximum photocatalytic efficiency. Zhang et al. (1998) reported that such optimal size was within the range of 11-21 nm for their TiO_2 catalyst. Koci et al. (2009) further reported that their TiO_2 catalyst with the particle size of around 14 nm performed the best activity on CO_2 photoreduction and the activity decreased significantly only when the size decreased down to 8 nm or increased up to 29 nm. These previous studies revealed that the charge carrier recombination rate of TiO_2 can be retarded by controlling the TiO_2 particle size within certain range, and a TiO_2 catalyst with optimal particle size did exhibit better activity on CO_2

photoreduction.). Furthermore, it is worthy to note that the particle size of a crystalline powder may not be the same as its crystallite size. This is because crystallite is the fine unit to compose a particle of a crystalline powder. A particle of a crystalline powder may consist of more than one crystallite (Waseda et al., 2011). Therefore, the particle size of a crystalline powder should not be smaller than its crystallite size.

The methods to synthesize nano-sized TiO_2 have been extensively reported previously (Wu and Yeh, 2001; Nagaveni et al., 2004; Li et al, 2003; Lee et. al., 2004; Lee et. al., 2006; Cong et al., 2007a; Feng et. al., 2008; Zhang et. al., 2009b; Trentler et. al., 1999), and the mechanisms of those methods have been comprehensively reviewed elsewhere (Chen and Mao, 2007). Among the methods for nano-sized TiO_2 synthesis (e.g. sol-gel method, hydrothermal method, and direct oxidation method), sol-gel method is one of the most widely used ones. This is because such method is able to synthesize highly pure oxides, and the reactions involved in this method can be initiated at ambient conditions. The mechanism of sol-gel method is presented in Section 2.3.2.1.1, and an example of a convenient sol-gel process to synthesize nano-sized TiO_2 is also described.

2.3.2.1.1 Sol-gel method

The sol-gel method is a versatile process used in making various ceramic materials (Chen and Mao, 2007). A sol is a colloidal suspension of solid particles in a liquid, wherein a colloid is a suspension in which the dispersed phase is so small (1-1000 nm) that gravitational forces are negligible and interactions are dominated by short-range forces, such as van der Waals attraction and surface charges (Brinker and Scherer, 1990). A gel is defined as an interconnected solid skeleton containing a continuous liquid phase (Brinker and Scherer, 1990). Therefore, sol-gel methods usually involve a process of the transition from liquid sol into a solid gel phase (Chen and Mao, 2007). In a typical so-gel process, a sol is formed via the hydrolysis and condensation reactions of the precursors, which are usually metal salts or metal alkoxides (Brinker and Scherer, 1990; Chen and Mao, 2007). Then the separated sols can link together via polymerization to form gel (Brinker and Scherer, 1990).

Currently, sol-gel methods are often used for the synthesis of nano-sized TiO_2. This process normally proceeds via a hydrolysis step of titanium(IV) alkoxide followed by condensation (Wu and Yeh, 2001; Chen and Mao, 2007). For example, Wu and Yeh (2001) successfully synthesized nano-sized TiO_2 by a refined sol-gel method. In contrast to other sol-gel methods that normally add hydrolyzing water dropwise (to control the hydrolysis rate; e.g. Anderson and

Bard, 1995; Yu et al., 2001; Zhu et al., 2006), the method developed by Wu and Yeh (2001) was more convenient. This is because the hydrolyzing water in such refined sol-gel process was slowly released by the esterification reaction of the chemicals homogenously mixed with the titanium precursor beforehand. Wu and Yeh (2001) used titanium(IV) n-butoxide ($Ti(OC_4H_9)_4$) as the titanium precursor. In a typical batch, 0.08 mol of n-butanol (C_4H_9OH) and 0.08 mol of acetic acid (CH_3COOH) were added to 0.02 mol of $Ti(OC_4H_9)_4$. Then water was slowly released by the esterification reaction of C_4H_9OH and CH_3COOH (reaction 2.13, wherein R represents C_4H_9O).

$$ROH + CH_3COOH \rightarrow H_2O + RCOOC_2H_5 \qquad \text{Reaction 2.13}$$

The water from esterification could react with $Ti(OC_4H_9)_4$ to initiate hydrolysis reaction (reaction 2.14).

$$Ti(OR)_4 + H_2O \rightarrow Ti(OR)_3(OH) + ROH \qquad \text{Reaction 2.14}$$

Then condensation reactions (Reactions 2.15 and 2.16) could occur to form suspended sol. The slow rate of the water release via the esterification reaction of C_4H_9OH and CH_3COOH (Reaction 2.13) significantly decreased the rate of the hydrolysis reaction of $Ti(OC_4H_9)_4$ (Reaction 2.14). This phenomenon avoided the rapid precipitation and allowed the formation of highly uniform

and fine sol during condensation (Wu and Yeh, 2001).

$$Ti(OR)_3(OH) + Ti(OR)_3(OH) \rightarrow (RO)_3Ti\text{-}O\text{-}Ti(OR)_3 + H_2O \qquad \text{Reaction 2.15}$$

$$Ti(OR)_3(OH) + Ti(OR)_4 \rightarrow (RO)_3Ti\text{-}O\text{-}Ti(OR)_3 + ROH \qquad \text{Reaction 2.16}$$

After the reactions described above (Reactions 2.13-2.16), the sol was dried (at 150 °C) before it transformed to gel, and this was to ensure that the TiO_2 nano-particles with uniform size could be obtained after the synthesis process. After drying, the sample was calcined at 500 °C to burn off the organic materials and transform the titanium precursor to TiO_2. Wu and Yeh (2001) reported that nano-sized (diameter ranged within 10-25 nm) TiO_2 was successfully synthesized via this sol-gel process. And this method could be also applied to synthesize the nano-sized metal (e.g. Cu) modified TiO_2, where the metal precursor (e.g. copper(II) chloride dihydrate) was homogeneously dissolved in the titanium precursor during this sol-gel process. The TiO_2 synthesized via the refined sol-gel method developed by Wu and Yeh (2001) were proven to be able to catalyzed CO_2 photoreduction in the later studies (Tseng et al., 2002, 2004).

2.3.2.2 Involving Ti^{4+} or TiO_2 species in mesoporous silicate materials

Another method to develop highly active and selective Ti-based photocatalyst

for CO_2 photoreduction is to include the Ti species (Ti^{4+} or TiO_2) in mesoporous silicate materials (e. g. MCM-41) (Anpo et al., 1998; Yamashita et al., 1998; Ikeue et al., 2002ab; Shioya et al., 2003; Lin et al., 2004; Li et al., 2010). This is because: (1) such supporting materials have very high surface area (can be up to 910 m^2/g (Zhao et al., 1998)) which leads to high adsorption capacity, and their adsorption properties can be controlled (e.g. through adjusting the pore opening size (Corma, 1997)), (2) active sites can be generated in the framework (e.g. Ti^{4+}) or cavity (e.g. TiO_2) of these porous materials, and (3) the intricate channel structure of these porous materials make them able to present different types of shape selectivity, e.g. product, reactant, and transition state, which can be used to direct a given catalytic reaction toward the desired product avoiding undesired side reactions (Corma, 1997).

Porous solid materials are widely used as adsorbents, catalysts and catalyst supports because of their high surface areas (Ciesla and Schuth, 1999). However, the utilization of these materials was seriously limited due to the small pore size (normally microporous, < 2 nm) and their internal disordered pore system with broad pore-size distributions (Ciesla and Schuth, 1999). This was greatly changed when Kresge et al. (1992) successfully synthesized the first mesoporous (pore size: 2-50 nm) solid material with regularly ordered pore arrangement and a very narrow pore-size distribution (e. g. Fig. 2.9, wherein such material is well known to be MCM-41). The concept of MCM-41

synthesis is known as liquid-crystal templating mechanism, in which the silicate material forms inorganic walls between the ordered surfactant micelles (e.g. hexadecyltrimethylammonium ion), and the surfactant micelles are removed by the heat treatment at the end of the synthesis process (Kresge et. al., 1992), resulting in the highly ordered mesoporous silicate material.

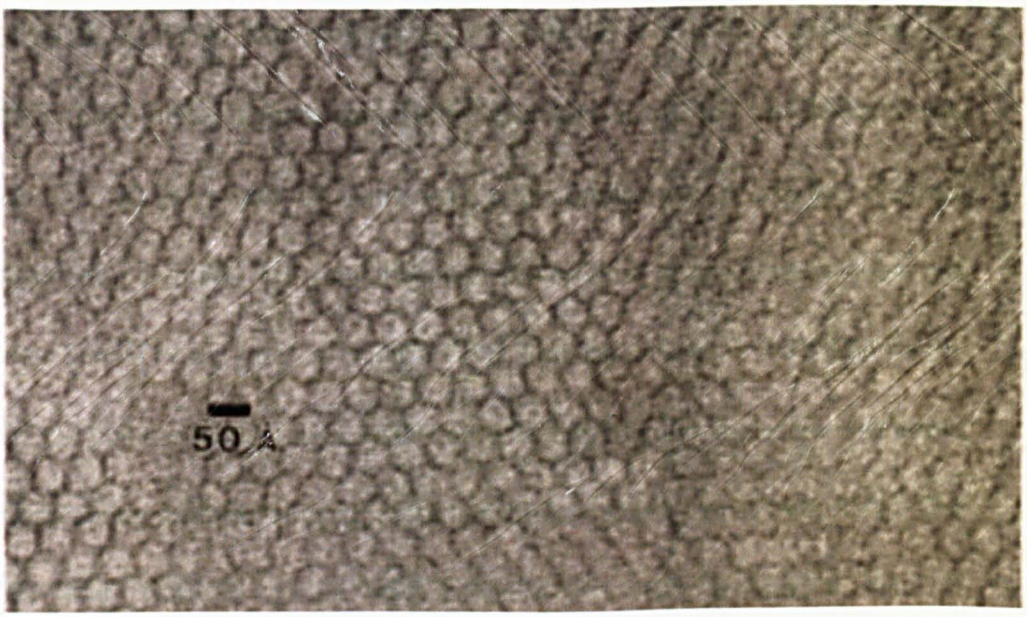

Fig. 2.9: Representative TEM micrograph of MCM-41 (Kresge et al., 1992).

Since liquid-crystal templating mechanism was proposed by Kresge et al. (1992), new mesoporous silicate materials had been synthesized based on the same mechanism (e. g. MCM-48) (Corma, 1997; Ciesla and Schuth, 1999). These mesoporous materials were used for different applications, including as the support for Ti-based species (Ti^{4+} or TiO_2) for redox photocatalysis reactions, e. g. selective photooxidation of hydrocarbon materials (e. g.

alcohols) and photoreduction of CO_2 (Clerici et. al., 1991; Bellusi et. al. 1992; Anpo et. al., 1998; Yamashita et. al., 1998; Ikeue et. al., 2002; Shioya et. al., 2003; Lin et. al., 2004; Li et. al., 2010).

The most extensive studies on Ti-containing mesoporous silica-based materials for CO_2 photoreduction have been conducted by Anpo's group since 1998 (Anpo et. al., 1998; Yamashita et. al., 1998; Ikeue et. al., 2002; Shioya et. al., 2003). They firstly incorporated Ti-based species in MCM-41 or Ti-MCM-48. The Ti^{4+} or TiO_2 were included within the framework or cavities of these mesoporous zeolites, wherein the pore volumes of these catalysts were not lower than 0.79 cm^3/g (Anpo et al., 1998, Yamashita et al., 1998). The results of CO_2 photoreduction with H_2O under UV irradiation indicated that these Ti-containing zeolite catalysts presented higher activity than bulk TiO_2. The CH_4 and CH_3OH yields by Ti-MCM-48 were around 8 and 3 $\mu mol \cdot g_{\text{-catalyst}}^{-1} \cdot hr^{-1}$, respectively. In contrast, the yields of CH_4 and CH_3OH by the bulk TiO_2 were only around 0.5 and 0 $\mu mol \cdot g_{\text{-catalyst}}^{-1} \cdot hr^{-1}$, respectively. Furthermore, Anpo's group also found that the activity of these Ti-containing zeolite catalysts strongly depended on their dispersion states of the Ti-based species in the zeolite frameworks and the internal surface topology of the zeolites. They reported that the catalyst with the highly dispersed Ti-based species (proven by the observation of the absorption band at the wavelength of around 280 nm in photoluminescence spectrum), larger pore size (> 20 nm,

comparing to the catalyst with pore size of 5.7 nm), and three dimentional channel structure presented the highest activity (Anpo et al., 1998, Yamashita et al., 1998).

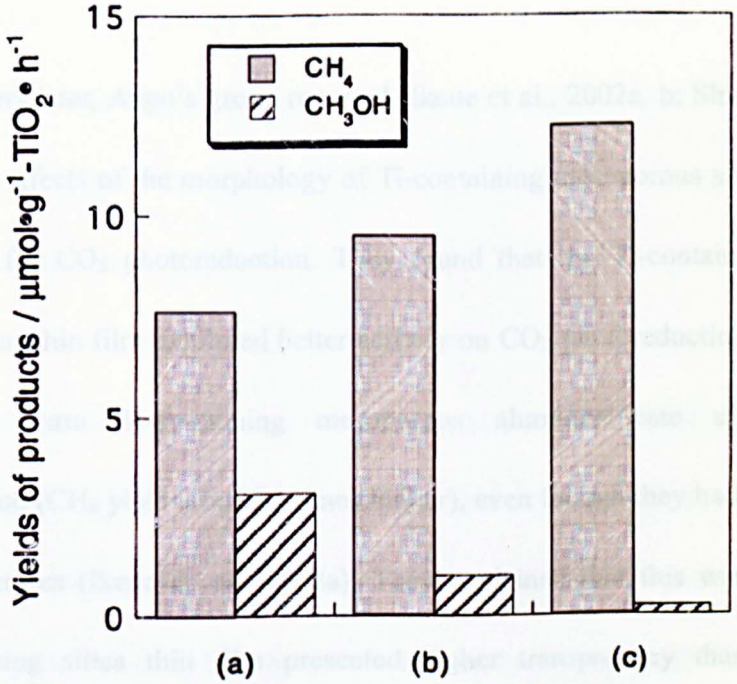

Fig. 2.10: Effects of Pt modification on Ti-MCM-48 for the yields of CH_4 and CH_3OH upon CO_2 photoreduction. (a): Ti-MCM-48, (b) 0.1wt% Pt modified Ti-MCM-48, (c) 1wt% Pt modified Ti-MCM-48, (Anpo et al., 1998).

Moreover, Pt had also been added into Ti-containing zeolite catalysts in order to increase the separation of the photo-generated electrons and holes (Anpo et al., 1998, Yamashita et al., 1998). The following CO_2 photoreduction tests showed that the presence of Pt was able to further promote the activities of Ti-containing zeolite catalysts (Fig. 2.10) even though the local structures of those catalysts were not changed by the presence of Pt. It is interesting to note

that the reaction selectivity of the Pt modified Ti-containing zeolite catalysts was changed compared to the unmodified ones, wherein CH_4 other than CH_3OH became the primary product (Anpo et al., 1998, Yamashita et al., 1998).

A few years later, Anpo's group reported (Ikeue et al., 2002a, b; Shioya et al., 2003) the effects of the morphology of Ti-containing mesoporous silica-based materials for CO_2 photoreduction. They found that the Ti-containing silica mesoporous thin film exhibited better activity on CO_2 photoreduction than the powdered form Ti-containing mesoporous aluminosilicate under UV illumination (CH_4 yield around 5 times higher), even though they had the same pore structures (Ikeue et. al., 2002a). They explained that this was because Ti-containing silica thin film presented higher transparency than that of aluminosilicate and its form of thin film avoided the effect of the light scattering which normally occurred on the surface of the samples in powdered form (Ikeue et. al., 2002a; Shioya et. al., 2003).

Other researchers have also conducted investigations concerning the utilization of Ti-containing mesoporous silica-based materials for CO_2 photoreduction. Lin et al. (2004) monitored the reactions of CO_2 photoreduction with H_2O catalysed by Ti^{4+} incorporated within the framework of MCM-41 using an in-situ FT-IR spectroscopy. They confirmed the ability of the UV excited Ti^{4+}

within the framework of mesoporous zeolite to split CO_2 to CO with the presence of H_2O. Li et al. (2010) also studied the effect of Cu loading on Ti-containing mesoporous silica for CO_2 photoreduction with H_2O, wherein TiO_2 (P25) was included within the cavities of the porous silica. They found that the Cu loading with the chemical state of Cu_2O was able to increase the activity of this mesoporous silica supported TiO_2 (e.g. total hydrocarbon materials yield increased around 5 times when the silica supported TiO_2 catalyst was loaded with 0.5 wt% Cu).

In summary, it can be confirmed that incorporation of TiO_2 in silica based mesoporous materials is indeed one of the promising ways to develop highly active and selective Ti-based catalyst for CO_2 photoreduction. However, the current studies are only sufficient to prove the higher activity of such Ti-containing mesoporous silica catalyst compared to the traditional bulk crystal TiO_2. Furthermore, the detailed relation between the inherent properties of such mesoporous catalysts (e.g. optimal pore size) and their activities for CO_2 photoreduction still need to be further investigated.

2.3.2.3 Anion doped TiO_2

As described in Section 2.3, one of the primary problems for TiO_2 to be an effective catalyst for CO_2 photoreduction is its relatively large band-gap (3.2

eV), which allows it only to be excited within the UV region. Therefore, it is necessary to find an approach to enlarge the absorption range of TiO_2 to the visible region without decreasing the activity of TiO_2. Doping TiO_2 with an anion (e. g. C, N, S) can fit the requirements above and this has attracted great interest in recent years (Khan et al., 2002; Irie et al., 2003a, b; Noworyta et al., 2004; Wang and Lewis 2005, 2006; Asahi et al., 2001; Lindgern et al., 2003; Diwald et al., 2004; Di Valentin et al., 2004; Umebayashi et. al. 2002, 2003a, b; Yamamoto et. al., 2004; Serpone, 2006). Asahi et al. (2001) reported, for the first time, that substitutional doping of C, N, F, P, and S into the lattice of TiO_2 anatase could successfully increase the absorption of visible light of TiO_2 anatase by narrowing the band-gap. Asahi et al. (2001) explained that the TiO_2 band-gap was narrowed by anion dopants (e. g. N) as they introduced additional energy level above the VB edge of TiO_2 anatase (Fig. 2.11). Asahi et al. (2001) also evaluated the activity of their TiO_2 catalysts substitutionally doped with N under visible light, and the results indicated that the photo-degradation rate of gaseous acetaldehyde by N doped TiO_2 was superior (around 40 times more efficient) to that of the pure TiO_2 under visible light, while those two catalysts presented similar activities under UV light.

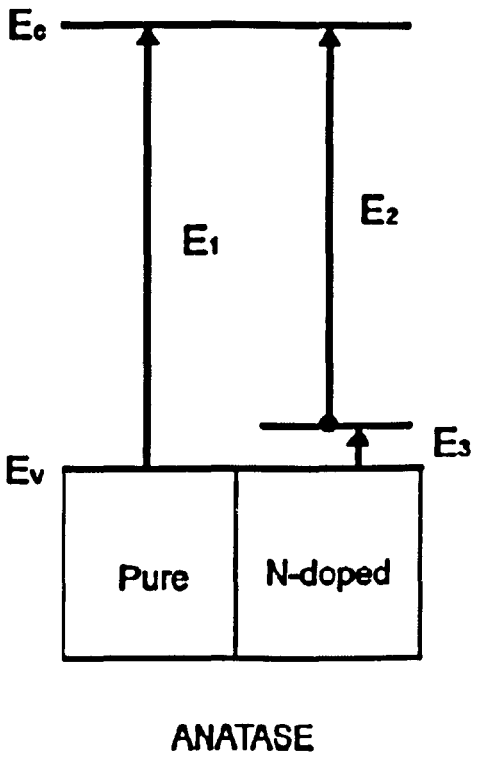

Fig. 2.11: Schematic electronic structure for pure and N substitutionally doped TiO_2 anatase (Di Valentin et al., 2004).

It has been argued that the promotion of the visible light absorption of the anion doped TiO_2 was in fact due to the formation of the colour centres caused by the defects on TiO_2 associated with oxygen vacancies and not to a narrowing of the original band-gap of TiO_2 (Serpone, 2006). However, more studies had been conducted and further proven the activity of the anion doped TiO_2 for various photocatalysis processes under visible light (Irie et. al., 2003a, b; Sakthivel et al., 2004; Sathish et al., 2005; Cong et al., 2007b; Umebayashi et al., 2003a; Hamal et al., 2007; Ho et al., 2006; Lin et al., 2011; Park et al., 2006). The N doped TiO_2 was reported to be active under visible light for the photo-degradation of 2-propanol (Irie et. al., 2003b), 4-chlorophenol (Sakthivel

et al., 2004), methylene blue (Sathish et al., 2005), rhodamine B (Cong et al., 2007b), and 2, 4-dichlorophenol (Cong et al., 2007b). The S doped TiO_2 was reported to be active under visible light for the degradation of methylene blue (Umebayashi et al., 2003a), 4-chlorophenol (Ho et al., 2006), and acetaldehyde (Hamal et al., 2007). Finally C doped TiO_2 was also found to be an efficient photocatalyst under visible light for the degradation of organic materials, e. g. 2-propanol (Irie et. al., 2003a) and dye Reactive Brilliant Red X-3B (Lin et al., 2011).

Even though the anion doped TiO_2 had been successfully utilized for various photocatalysis processes under visible light, the study on the use of such catalyst for CO_2 photoreduction has not yet been extensively conducted. Up to now the only publication on this field is by Varghese et al. (2009), wherein the activity of N doped TiO_2 nanotube arrays was evaluated for CO_2 photoreduction under natural solar light. The result of this study indicated that CO_2 was successfully reduced under sunlight into hydrocarbon materials (including methane, ethane, propane, butane, pentane, hexane, and olefins) by using N doped TiO_2 anatase nanotube with Pt or Cu added to the surface of TiO_2. However, Varghese et al. (2009) did not consider the N dopant to be the significant contributor to such process. This was because they found that their optimal N doped TiO_2 catalyst (with N doping ratio to be 0.4 atom%) generated significantly less charge carriers (around 1/8) at the 400-500 nm wavelength

range than that at the UV region (data obtain by photocurrent spectrum) (Varghese et al., 2009). Nevertheless, their conclusion still needs to be further confirmed by the direct comparison of the pure and N doped TiO_2 catalysts for CO_2 photoreduction under sunlight, as the solar spectrum only has a small fraction (maximum to be 3 %) in the UV region. Meanwhile, the use of other anions (e. g. S, C) doped TiO_2 for visible CO_2 photo-reduction is another interesting topic worthy to be studied.

In summary, the band-gap of TiO_2 may be narrowed through anion doping by introducing additional energy level above the TiO_2 VB. Anion doped catalysts have been proven to be photo-catalytically active under visible light. However, there is still lack of extensive investigation on the utilization of such catalysts for CO_2 photoreduction under visible light.

2.4 Analytical techniques

A series of analytical techniques can be used for TiO_2 characterization to gain information on their properties. This section introduces the background knowledge of these techniques, including powder X-ray diffraction, X-ray photoelectron spectroscopy, transmission electron microscopy, nitrogen adsorption isotherms, copper surface area measurement, inductively coupled plasma spectrometry, and diffuse reflectance ultraviolet-visible spectroscopy.

2.4.1 Powder X-ray diffraction (powder XRD)

X-ray diffraction from crystals was discovered in 1912 by Max von Laue and in 1913 by W. L. Bragg and W. H. Bragg. Since that, there have been numerous advances in the field of using X-ray diffraction for crystallography. One of the most important achievements is the development of the technique of powder XRD. This technique dates back to Debye and Scherrer (1916) who observed X-ray diffraction from LiF powder and successfully revealed its crystal structure. Then, after the efforts of Hull (1919) and Hanawalt et al. (1938), the technique of powder XRD was formalized to determine the crystalline structures of solid powder materials (Pecharsky and Zavalij, 2009).

In a typical powder XRD analysis, a beam of X-ray strikes the atoms of a material. The electrons of these atoms then oscillate and re-emit diffracted X-rays which are the spherical waves centring on the respective atoms and with the same wavelength as that of the incident X-rays (Waseda et al., 2011). These diffracted X-rays from atoms can interfere with each other to generate a diffraction pattern. Such diffraction pattern is recorded and used to reveal the information of the atomic structure of a material when the interferences occur within the orderly arranged atoms, such as the atoms of a crystal (Boone, 2000).

The main target of recording the diffraction pattern of the crystal is to know the particular condition in which the diffracted X-rays from the atoms of the crystal are completely in phase and reinforce each other, which leads to constructive interference and generate characteristic peak in the diffraction pattern (Waseda et al., 2011). Fig 2.12 schematically describes the paths of X-rays through crystal atomic planes. The angle of incidence of the two parallel X-rays (rays A_1B_1 and A_2B_2) is θ, the wavelength of the incident X-rays is λ, and the interplanar spacing between the crystal atomic planes is d. Following the Bragg's law (Pecharsky and Zavalij, 2009), the diffracted X-rays from crystal (rays B_1C_1 and B_2C_2) will present in phase and cause constructive interference when the difference between the lengths of the paths $A_1B_1C_1$ and $A_2B_2C_2$ ($2d \cdot \sin\theta$) is equal to the wavelength of the incident X-ray multiplied by an integral number (n), which is expressed:

$$n\lambda = 2d \cdot sin\theta \qquad \text{Eq. 2.1}$$

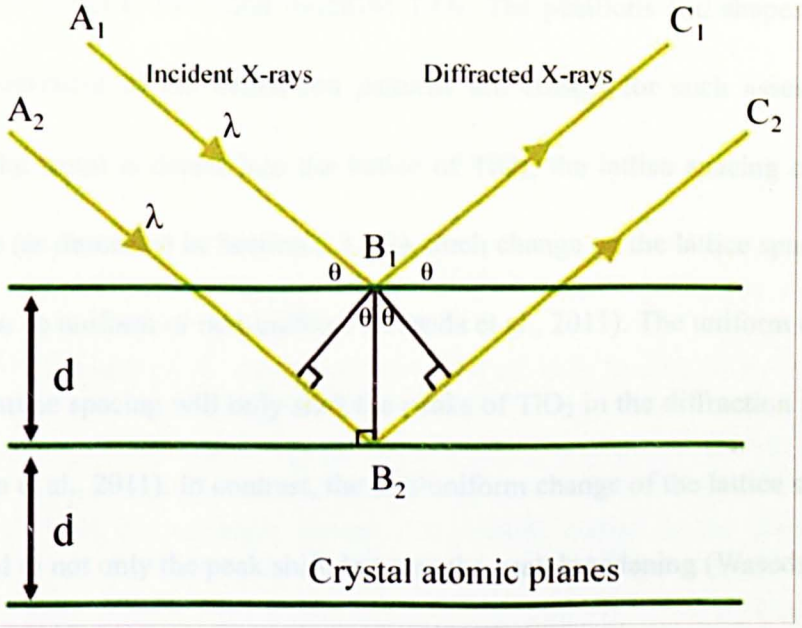

Fig 2.12: Schematic diagram of diffraction of X-rays by a crystal, modified from Henry et al. (2010).

Therefore, when a crystal material with regular atomic planes is scanned by a beam of X-ray with fixed wavelength in a wide range of incident angles, the characteristic peaks at certain angles can be presented in the recorded diffraction pattern, leading to a clear mapping to the crystal structure of the scanned material. Hence, diffraction patterns are usually plotted in the form of the measured intensity of the diffracted X-ray as the dependent variable versus the incident angle of X-ray as the independent variable (Pecharsky and Zavalij, 2009).

Powder XRD can be used to study the crystalline structures of TiO_2, such as to identify if it is anatase or rutile. It is also able to identify if the added metal is

loaded or doped to the metal modified TiO_2. The positions and shapes of the peaks presented in the diffraction patterns are critical for such assessment. When the metal is doped into the lattice of TiO_2, the lattice spacing of TiO_2 changes (as described in Section 2.3.1.2). Such change on the lattice spacing of TiO_2 can be uniform or non-uniform (Waseda et al., 2011). The uniform change of the lattice spacing will only shift the peaks of TiO_2 in the diffraction pattern (Waseda et al., 2011). In contrast, the non-uniform change of the lattice spacing will lead to not only the peak shift, but also the peak broadening (Waseda et al., 2011). For example, Xin et al. (2005) used powder XRD to analyse the TiO_2 samples with Ag doped into their lattices. The results (Fig. 2.13 and Table 2.3) clearly showed that both the shift and broadening of the peaks of TiO_2 were observed in the diffraction patterns, indicating that the lattice spacing of TiO_2 was non-uniformly changed by the Ag dopant.

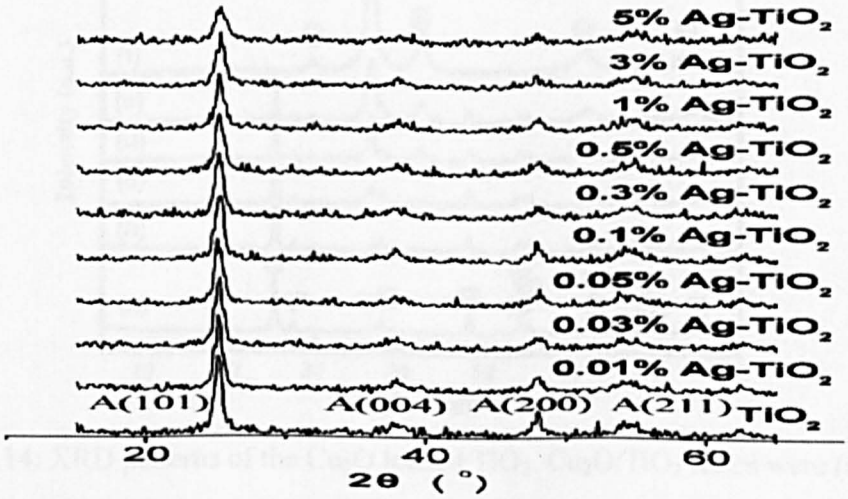

Fig. 2.13: XRD patterns of Ag doped TiO_2 with different doping ratios, (Xin et al., 2005).

Table 2.3: XRD shift of Ag doped TiO_2 with different doping ratios, (Xin et al., 2005).

Ag doping ratio (mol %)	0	0.01	0.05	0.5	3
2θ (deg)	25.36	25.32	25.26	25.2	25.06

On the other hand, when the added metal is loaded on the surface of TiO_2, the metal will not change the crystalline structure of TiO_2 leading to no variation on both the positions and shapes of the peaks presented in the diffraction pattern of TiO_2. For example, Huang et al. (2009) studied on the preparation and characterization of the Cu_2O loaded TiO_2, and Fig. 2.14 illustrates the XRD patterns of their samples. It can be seen that the presence of Cu_2O did not change the positions and shapes of the characteristic peaks of TiO_2 in the diffraction patterns, even when the ratio of Cu_2O:TiO_2 was as high as 50 %.

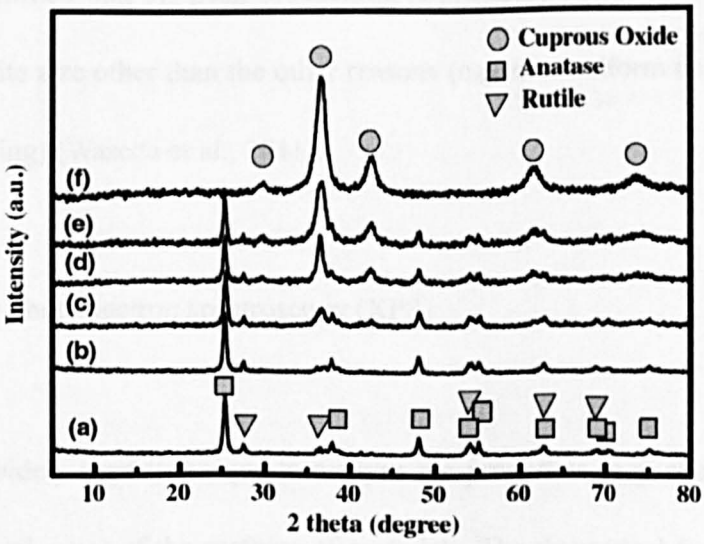

Fig 2.14: XRD patterns of the Cu_2O loaded TiO_2. Cu_2O/TiO_2 ratios were (a): 0 %, (b): 2 %, (c): 10 %, (d): 30 %, (e): 50 %, and (f): 100 %, respectively (Huang et al., 2009).

Furthermore, the average crystallite size of TiO_2 can be calculated by using the data of powder XRD via Scherrer Formula:

$$D = \frac{K \cdot \lambda}{\beta \cdot \cos\theta} \qquad \text{Eq. 2.2}$$

where D refers to the average diameter of crystallite, K is a constant in the range of 0.8-1.39, λ is the wavelength of the incident X-ray, β is the full width at half maximum (FWHM, in radians) of the peak presented in the diffraction pattern, and θ is the position of the same peak which is usually the one with the maximum intensity (Jenkins and Snyder, 1996). Scherrer Formula can estimate the crystallite size of the analysed sample with the error of around 5 % (Waseda et al., 2011). It must be noted that Scherrer Formula is applicable only if it is confirmed that the peak broadening is primarily due to the decrease of the crystallite size other than the other reasons (e.g. non-uniform change of the lattice spacing) (Waseda et al., 2011).

2.4.2 X-ray photoelectron spectroscopy (XPS)

XPS is a widely used technique to analyse the properties (e.g. chemical state and elemental ratio) of the surfaces of materials. The theoretical foundation of this technique dates back to 1905, when Einsein wrote his well-known photoeffect equation:

$$h\nu = E_b + E_{kin} \qquad \text{Eq. 2.3}$$

where $h\nu$ is quantum energy, E_b is the binding energy of the electron in matter, and E_{kin} is the kinetic energy of the ejected electron (Nefedov, 1988). The definition of binding energy is "the energy required to eject an electron from a certain orbital of a substance", which is a characteristic value of a substance. Photoeffect equation indicates that such value can be calculated by knowing the energy of the photon impinging upon the electron and the kinetic energy of this electron when it is ejected. Basing on this theory, K. Siegbahn and his research group developed the practical XPS technique in the 1960s (Nefedov, 1988).

In a typical XPS analysis, a beam of X-ray with known photon energy strikes the surface of the analysed substance, and the incident photons will impinge upon and eject electrons from a certain orbital of the substance (e.g. O 1s, Ti $2p_{3/2}$). The escape depth of the ejected electrons is usually not larger than 5 nm (which is the reason for XPS to be considered as a surface analysis technique), and the kinetic energies of these ejected electrons are recorded to determine the binding energies of these electrons (Nefedov, 1988). At the end of the XPS analysis, the peaks of the binding energies corresponding to certain elements will be presented in the resulting spectrum. Such spectrum is usually plotted in

the form of the measured intensity of the ejected electrons as the dependent variable versus the binding energy as the independent variable (example shown in Fig. 2.15). It should be noted that the analysed materials (e.g. semiconductors) become positively charged during the XPS analysis, which leads to the shift of the binding energy of the analysed material. Therefore, it is necessary to correct the shifted binding energy when processing XPS data (Bhattacharya et al., 1997). This phenomenon is called "charge correction", which can be done by setting an element with well proven value of binding energy as reference. For example, O 1s can be set as the referencing element for charge correction when processing the XPS data of anatase, because the value of the binding energy of O 1s of anatase has been well proven to be 530 eV in the previous study (Rensmo et al., 1997).

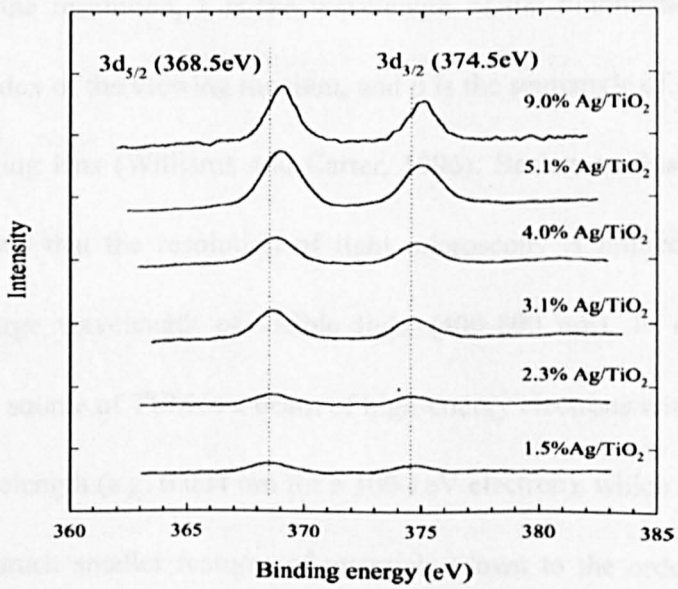

Fig. 2.15: Example of the XPS spectra of Ag 3d, (Tseng and Wu, 2004).

2.4.3 Transmission electron microscopy (TEM)

TEM is a type of electron microscopy that was firstly built by M. Knoll and E. Ruska in 1932 (Williams and Carter, 1996). It is able to offer significantly higher image resolution than light microscope and widely used for material characterization (e.g. to study the material morphology).

The term "resolution" of a microscope is defined as the distance between two details just separable from one another, which can be expressed by Rayleigh criterion as:

$$\delta = \frac{0.61 \cdot \lambda}{\mu \cdot \sin \beta} \qquad \text{Eq. 2.4}$$

where δ is the resolution, λ is the wavelength of the illumination, μ is the refractive index of the viewing medium, and β is the semiangle of collection of the magnifying lens (Williams and Carter, 1996). Basing on this criterion, it can be known that the resolution of light microscopy is limited due to the relatively large wavelength of visible light (400-800 nm). In contrast, the illumination source of TEM is a beam of high-energy electrons with drastically smaller wavelength (e.g. 0.004 nm for a 100-keV electron), which allows TEM to observe much smaller features of materials (down to the order of several nanometers) than light microscopy (Williams and Carter, 1996; Zlateva and

Martinova, 2008).

In a conventional TEM, a beam of electrons is accelerated in a high-voltage field (up to 1000 kV) in vacuum. These high-energy electrons then impinge upon the analysed sample, which is thin enough to allow a portion of the incident electrons to transmit through it. During this process, a variety of interactions between the incident electrons and the analysed sample take place and generate various signals (Fig. 2.16, Williams and Carter, 1996). Such signals can be utilized by a variety of techniques for material characterization. For example, the backscattered electrons and secondary electrons can be used by scanning electron microscopy (SEM) for imaging, and the auger electrons can be used by auger electron spectroscopy (AES) to characterize the elemental composition of the material surface (Gao, 2008).

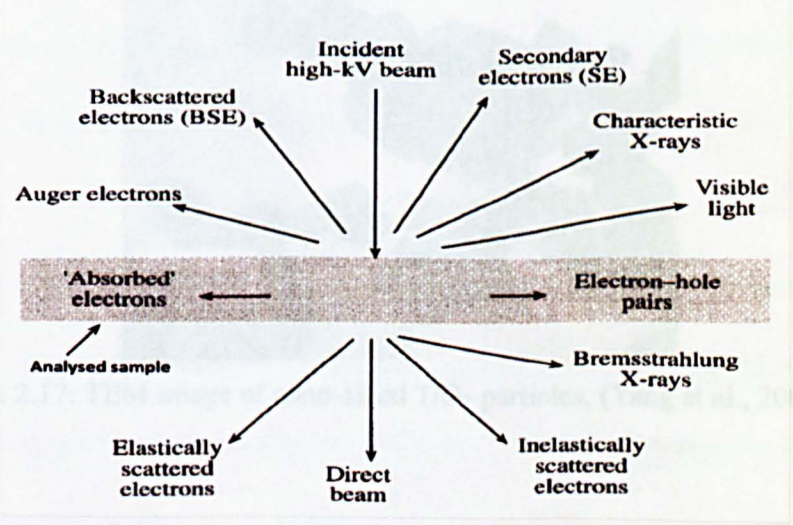

Fig 2.16: Signals generated when a high-energy beam of electrons interacts with a thin specimen, modified from (Williams and Carter, 1996).

For TEM, the direct beam (the electron beam that comes through the analysed sample, parallel to the direction of the incident electron beam) and the forwardscattered electrons (electrons scattered through < 90°, including elastically scattered ones with no loss of energy and inelastically scattered ones with measurable loss of energy) are used for the formation of image (Williams and Carter, 1996), wherein the image with better quality formed by using the direct beam is termed "bright field image" and the one formed by using the forwardscattered electrons is termed "dark field image" (Williams and Carter, 1996). TEM can be used to study the morphology (e.g. particle size) of the nano-sized TiO_2. Fig. 2.17 shows a typical TEM image of the particles of a nano-sized TiO_2 sample. It can be seen that the particles of TiO_2 were clearly observed in the image.

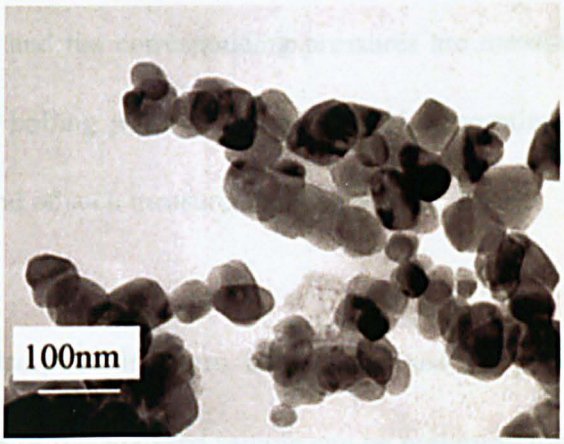

Fig. 2.17: TEM image of nano-sized TiO_2 particles, (Yang et al., 2001).

2.4.4 Nitrogen (N_2) adsorption isotherms

N_2 adsorption isotherms are widely used for determining the surface area and pore size distribution of solid materials (Sing et al., 1985). This technique reveals the surface properties of the analysed sample via the study on its N_2 adsorption process. The term "adsorption isotherm" was defined by Sing et al (1985) as "the relation, at constant temperature, between the amount adsorbed and the equilibrium pressure of the gas".

When measuring a N_2 adsorption isotherm, the analysed sample firstly undergoes an outgassing process (usually under a high vacuum at elevated temperature) in order to remove the existing physisorbed species from its surface. Then N_2 is introduced to the analysed samples, where the quantities of the N_2 adsorbed and the corresponding pressures are measured at a constant temperature (the boiling point of N_2) and the N_2 adsorption isotherm can be obtained at the end of such measurement (Sing et al., 1985).

After the N_2 adsorption isotherm of the analysed sample is obtained, the surface properties of the analysed sample can be preliminarily evaluated by the classification of such N_2 adsorption isotherm. There are six types of adsorption isotherms, which are shown in Fig. 2.18. These different isotherms stand for different surface properties of the solid materials. The indications of different

types of isotherms have been summarised in previous studies (Sing et al., 1985; Kruk and Jaroniec, 2001). For example, the types IV and V isotherms featured by the presence of hysteresis loops indicate the adsorption on mesoporous solid materials proceeds via multilayer adsorption (the adsorption space accommodates more than one layer of molecules) followed by capillary condensation (the residual pore space which remains after multilayer adsorption has occurred is filled with condensate separated from the gas phase) (Kruk and Jaroniec, 2001).

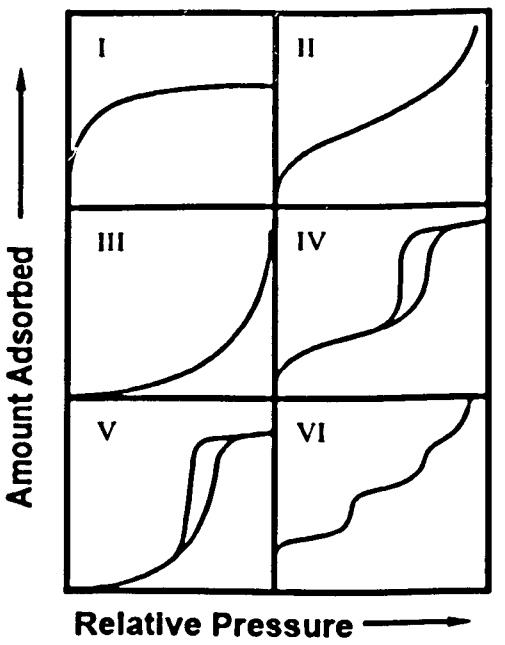

Fig. 2.18: Types of adsorption isotherms, modified from Sing et al. (1985).

The data of N_2 adsorption isotherms can be also used to determine the surface area of the analysed sample via Brunauer-Emmett-Teller (BET) theory (Brunauer et al., 1938) by calculating the monolayer capacity of the analysed

sample (the amount of adsorbate needed to cover the surface with a complete monolayer of molecules) (Sing et al., 1985). The equation used in such calculation is shown as:

$$\frac{P}{V\cdot(P_0 - P)} = \frac{1}{V_m\cdot C} + \frac{C-1}{V_m\cdot C}\cdot\left(\frac{P}{P_0}\right) \qquad \text{Eq. 2.5}$$

where V is the volume of N_2 adsorbed by the analysed sample at the relative pressure of P/P_0, V_m is the monolayer capacity, P is the actual N_2 pressure, P_0 is the vapour or saturation pressure of the N_2 at the analysis temperature, and C is a constant related to the enthalpy of adsorption in the first adsorbed layer (Sing et al., 1985). The total and specific surface areas of the analysed sample can be calculated by using the value of its monolayer capacity via equations:

$$A_s = V_m \cdot L \cdot a_m \qquad \text{Eq. 2.6}$$

and

$$a_s = \frac{A_s}{m} \qquad \text{Eq. 2.7}$$

where A_s and a_s are the total and specific surface areas, respectively, of the analysed sample (of mass m), L is the Avogadro constant, and a_m is the molecular cross-sectional area of N_2 (0.162 nm^2 at 77 K) (Sing et al., 1985).

Furthermore, the total pore volume of the analysed sample can also be calculated from the amount of the N_2 adsorbed at a relative pressure close to the saturation vapour pressure (e.g. at a relative pressure P_0/P of 0.99) by converting such amount of the adsorbed N_2 to the corresponding volume of the liquid N_2 at the temperature of the adsorption measurement (Kruk and Jaroniec, 2001).

N_2 adsorption isotherms have been widely used to measure the specific surface area of TiO_2. Such parameter is important to affect the activity of TiO_2. The specific surface area of the most well-known TiO_2 powder, Degussa P25, has been measured by N_2 isotherms to be 49 m^2/g (Ohno et al., 2001). It has been reported that increasing the specific surface area of TiO_2 was able to increase the activity of TiO_2 (Jung et al., 2000; Tian et al., 2007). This is because a large specific surface area can supply more active sites and number of substrates adsorbed on the surface of TiO_2 (Zhang et al., 1998). However, the enhancement of the activity of TiO_2 will not be significant unless the extent of the surface area increase was great enough. For example, Jung et al. (2000) were able to increase the surface area of TiO_2 by enclosing the TiO_2 powders into porous silica. But they found that the activities of the TiO_2 catalysts were not significantly enhanced (increased by around 30 %) until the specific surfaces of these catalysts increased by 200 % (from around 50 m^2/g to around 150 m^2/g) (Jung et al., 2000). Tian et al. (2007) also conducted investigation on

the relation between the specific surface area of TiO_2 and its activity. They reported that the activity of the TiO_2 catalysts were greatly improved (increased by 40 %) when their specific surface areas increased by 266.15 % (from 65 m^2/g to 238 m^2/g) (Tian et al., 2007).

2.4.5 Copper (Cu) surface area measurement

The surface area of metal oxide-supported Cu can be measured by using nitrous oxide (N_2O) as adsorbate (Chinchen et al., 1987). In contrast to N_2 adsorption measurement which involves physisorption process (Sing et al., 1985), this technique measures the Cu surface area via chemisorption process. And N_2O is chosen as the adsorbate for chemisorption process. This is because it has been confirmed that, at temperatures below 100 °C, the oxidation of Cu by N_2O is sufficiently mild that only the surface Cu atom is oxidized and that only to the Cu(I) oxidation state (Narita et al., 1982).

The basic principle of such measurement is to determine the numbers of the oxygen (O) atoms chemisorbed on the surface Cu atoms. This is based on the process of the decomposition of N_2O molecules on the surface of Cu to produce chemisorbed O atoms which generate gas phase N_2 according to the process:

$$N_2O_{(g)} + 2Cu_{(s)} \rightarrow N_{2(g)} + Cu_2O_{(s)} \qquad \text{Reaction 2.17}$$

where s denotes surface atoms (Chinchen et al., 1987). According to the stoichiometry presented in N_2O decomposition reaction, the number of chemisorbed O atoms can be determined by knowing the number of N_2 molecules produced after the reaction (which can be quantified by e.g. mass spectrometer). Since one O atom is adsorbed per two surface Cu atoms, the chemisorbed O atoms forms a half-monolayer on the surface of Cu with a value of 2×10^{-19} m^2/oxygen atom (Scholten and Konvalinka, 1969). Therefore, the total Cu surface area can be calculated via multiplying the total number of the chemisorbed O atoms by 2×10^{-19} (Chinchen et al., 1987). Moreover, the Cu dispersion (the ratio between the number of the surface Cu atoms and the number of the total Cu atoms) can also be evaluated by using the data obtained during the Cu surface area measurement, because the number of the surface Cu atoms could be calculated via multiplying the total number of the chemisorbed O atoms by 2 (according to the stoichiometry presented in reaction 2.17).

Chinchen et al. (1987) validated the technique of using N_2O as adsorbate to determine Cu surface area. Their study measured the surface area of the unsupported Cu by both N_2 adsorption isotherms and N_2O chemisorptions process. The average values of the Cu specific surface areas measured by these two measurements (N_2: 4.98 m^2/g, N_2O: 4.62 m^2/g) were generally consistent

with each other. Currently, the technique of Cu surface area measurement has not been used on the TiO_2 supported Cu.

2.4.6 Inductively coupled plasma mass spectrometry (ICP-MS)

ICP-MS is a trace element technique (mainly for metal) developed in 1980s, which can offer extremely low detection limits in the sub parts per trillion (ppt) range (Thomas, 2008).

The term "plasma" refers to quasi-neutral assemblies of charged particles (Sturrock, 1994). Plasma can be generated by heating a gas and ionizing its molecules or atoms (Sturrock, 1994). The fundamental principle of ICP-MS is to use a high-temperature (approximately 6000-7000 K) argon plasma to convert the analysed samples into positively charged ions. These ions are then separated and quantified by a mass spectrometer (Thomas, 2008).

In a typical ICP-MS analysis, first of all the analysed sample (usually in liquid form) is converted into aerosol by a nebulizer. Such aerosol is then delivered to a high-temperature argon plasma torch, where the aerosol is firstly atomized into ground-state atoms and then ionized (via removing electrons from the atoms) into positively charged ions by the highly energized argon ions (Thomas, 2008). The resulting positively charged ions are then brought into a

mass spectrometer. These ions are firstly separated in the mass spectrometer by an electrostatic filter due to their different values of mass-to-charge ratio (a value determining the motion of a charged particle in a vacuum when it is subjected to an electrostatic field) (Thomas, 2008). At last, the separated ions arrive the detector of the mass spectrometer, and are converted into electrical pulses which can be used for trace element quantitation (Thomas, 2008).

ICP-MS has not been reported to be used for the elemental analysis of TiO_2. This is because ICP-MS requires the analysed sample to be well dissolved prior to the analysis, but TiO_2 is extremely chemically stable. Therefore, special dissolution process is required before analysing TiO_2 by ICP-MS. The process of dissolving TiO_2 in this work is described in Section 3.2.7.

2.4.7 Diffuse reflectance ultraviolet-visible (DR UV-Vis) spectroscopy

DR UV-Vis spectroscopy is a convenient technique to study the heterogeneous catalyst in the form of solid powder. This technique is able to probe both d-d transition and charge transfer transition within the analysed sample. Therefore, DR UV-Vis spectroscopy is often used to spectroscopically estimate the band-gap energy of the semiconductor catalyst and identify the chemical state of the supported metal on the catalyst surface (Weckhuysen and Schoonheydt, 1999).

In contrast to the conventional UV-Vis spectroscopy that extract the UV-Vis absorption properties of the analysed sample (usually in liquid form) from the transmitted light, DR UV-Vis spectroscopy characterizes the solid powdered sample basing on the reflection of light by the analysed sample in the UV-Vis region (Weckhuysen and Schoonheydt, 1999).

The base quantity that characterizes the process of the light reflection during the DR UV-Vis spectroscopy analysis is the reflectance, which is defined as the ratio of the reflected light flux to the incident light flux (Torrent and Barron, 2008). In a typical DR UV-Vis spectroscopy analysis, a beam of incident light with the wavelength varying from 200 to 800 nm impinges upon the analysed powdered sample, whose layer is thick enough to ensure that a further increase in thickness will not change the reflectance (Torrent and Barron, 2008). The incident light is then partially absorbed and partially scattered. The scattered light diffusely reflected by the powdered sample is measured by an integration sphere, and the reflectance (R) of light can be recorded. After the analysis, the DR UV-Vis absorption spectrum (absorbance versus incident wavelength) of the analysed sample can be obtained. It should be noted that the "absorbance" presented in such DR UV-Vis absorption spectrum is, in fact, the "apparent absorbance" (equal to log(1/R)) which is used as a proxy for the actual absorbance (Torrent and Barron, 2008).

DR UV-Vis spectroscopy analysis can be used to determine the band-gap energies of the TiO_2 samples. The band-gap energy (E_g) can be calculated by using equation:

$$E_g = \frac{1240}{\lambda} \qquad \text{Eq. 2.8}$$

where λ is the threshold wavelength (wavelength that provides photon energy just sufficient to overcome the band-gap of semiconductor) of the semiconductor (Usubharatana et al., 2006). Such threshold wavelength can be determined in the DR UV-Vis absorption spectrum by using the method reported by Zhang et al. (2008). Fig. 2.19 illustrates the method of Zhang et al. (2008) to determine the threshold wavelengths of their TiO_2 nanotube samples. It can be seen that the trendlines of the portion of the graph reflecting the main absorption arising and the portion reflecting non-significant absorption arising were firstly drawn. Then the threshold wavelength can be determined by the position of the cross point of those two trendlines.

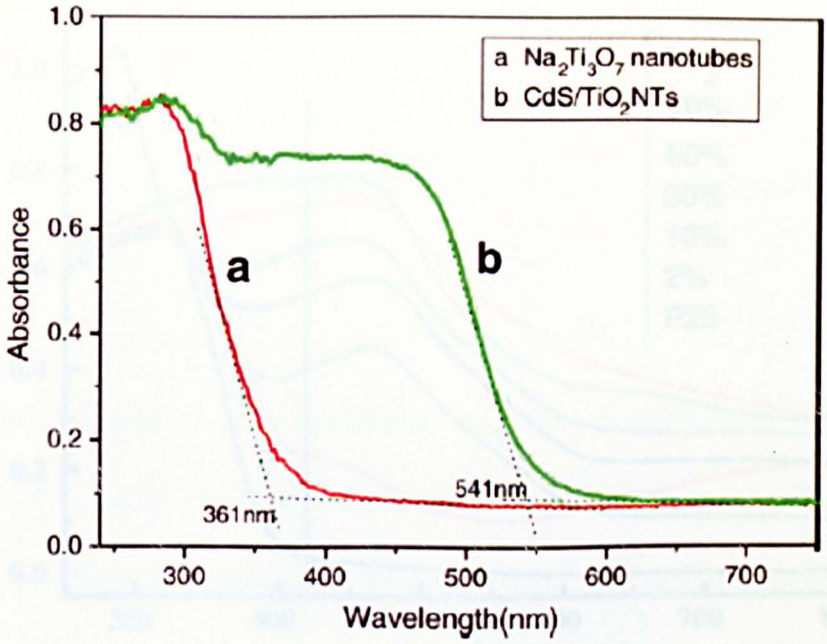

Fig. 2.19: DR UV-Vis absorption spectra showing how to determine the threshold wavelength (Zhang et. al., 2008).

Furthermore, the chemical state of the metal added to the surface of TiO_2 can be also determined by DR UV-Vis spectroscopy. For example, Fig. 2.20 shows the DR UV-Vis absorption spectra of the Cu_2O loaded TiO_2 samples in the study of Huang et al. (2009). It can be seen that the presence of Cu_2O on TiO_2 surface leads to the appearance of the characteristic absorption band at the wavelength between 400-600 nm.

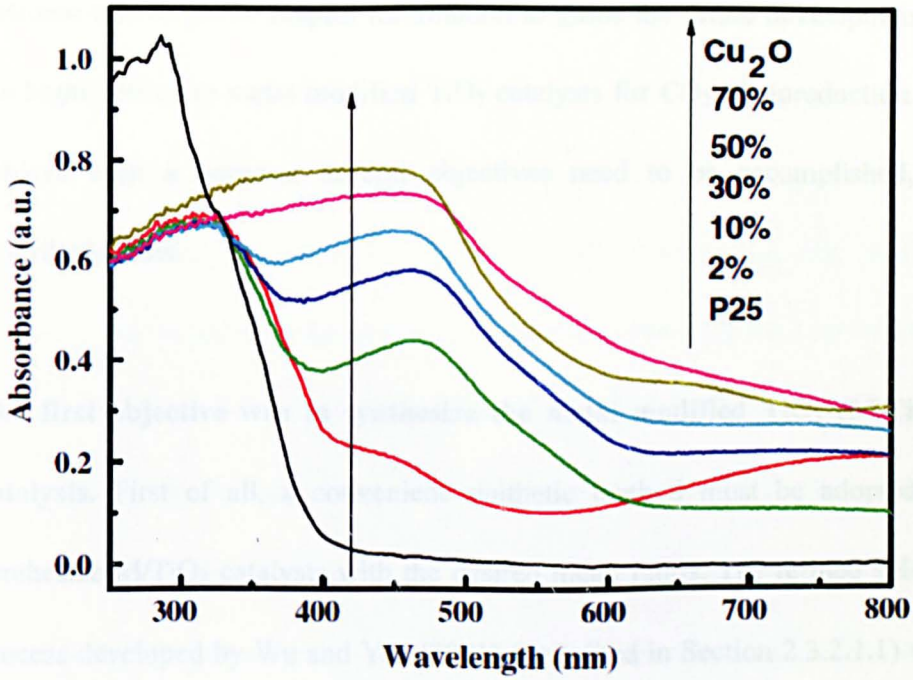

Fig: 2.20: DR UV-Vis absorption spectra of Cu_2O loaded TiO_2, (Huang et al., 2009).

2.5 Aim and objectives

As presented in Section 2.3, the primary problems for TiO_2 to be the practical catalyst for CO_2 photoreduction are its relatively low activity and poor photocatalytic performance under visible light. This work mainly focused on the improvement of the activity of TiO_2 for CO_2 photoreduction. As described in Section 2.3.1, metal modification is one of the most widely used methods for such purpose, but the understanding on how the added metal affects the activity of TiO_2 for CO_2 photo-reduction is still insufficient (e.g. examples described in Sections 2.3.1.3.1 and 2.3.1.3.2). **This work aimed to systemically study the effects of the metal modification on TiO_2 for CO_2 photoreduction.** The

outcome was to gather helpful information to guide the future development of the highly efficient metal modified TiO_2 catalysts for CO_2 photoreduction. To achieve such a purpose, several objectives need to be accomplished, as described below.

The first objective was to synthesize the metal modified TiO_2 (M/TiO_2) catalysts. First of all, a convenient synthetic method must be adopted to synthesize M/TiO_2 catalysts with the desired metal ratios. The refined sol-gel process developed by Wu and Yep (2001) (described in Section 2.3.2.1.1) was chosen for such purpose because this method was proven to be able to conveniently synthesize M/TiO_2 catalysts that could successfully catalyze CO_2 photoreduction (Tseng et al., 2002). After the synthesis method was selected, a series of metals were chosen to modify TiO_2. This work chose Cu, Zn, and Rh. This is because Cu had been reported to be one of the most promising metals to improve the TiO_2 activity for CO_2 photoreduction (Tseng et. al. 2002, 2004; Nguyen and Wu, 2008b; Wu and Chen, 2004; Yang et al., 2011). However, the detailed relation between the dispersion of the added Cu and the activity of Cu/TiO_2 has not been investigated. Zn was chosen because of the different positions of the CB and VB of ZnO comparing to Cu_2O. Therefore, Zn could be act as a contrast to Cu. Finally, Rh was chosen because it has been reported to improve the activity of TiO_2 for CO_2 photoreduction, but those previous studies did not clarify whether Rh was loaded or doped to TiO_2 (Kohno et al.,

1999; Solymosi et al., 1994). The process and results of M/TiO_2 synthesis are presented in Chapters 3 and 4, respectively.

The second objective was to comprehensively characterize the M/TiO_2 catalysts synthesized in this work. This was to obtain sufficient information on the properties of these M/TiO_2 catalysts. The properties investigated during the catalyst characterization process were expected to be crucial to determine the activity of M/TiO_2 catalyst for CO_2 photoreduction. These properties included the elemental ratio, crystalline structure, particle size, surface area, and absorption spectrum of M/TiO_2; and the chemical state, and dispersion of its added metal. The studies of the catalyst characterization are presented in Chapter 4.

The third objective was to evaluate the activities of the M/TiO_2 catalysts for CO_2 photoreduction. To achieve this objective, an experimental system to conduct the CO_2 photoreduction experiments was developed and set up. Such system should involve a reactor to initiate the CO_2 photoreduction reaction, and an analytical instrument that could measure the product from CO_2 photoreduction. The description of such CO_2 photoreduction experimental system is presented in Chapter 3.

The final objective was to ascertain how the added metal influences the activity of TiO_2. After the data of both the catalyst characterization and activities of the M/TiO_2 catalysts for CO_2 photoreduction were obtained, a detailed analysis and discussion regarding the relations between the activity and physic/chemical properties of the M/TiO_2 catalyst was conducted (Chapter 5).

References

Augustynski, J. (1993). The role of the surface intermediates in the photoelectrochemical behaviour of anatase and TiO_2. *Electrochimica Acta* **38**: 43.

Anpo, M., Yamashita, H., Ichihashi, Y., Fujii, Y., Honda, M. (1997), Photocatalytic reduction of CO_2 with H_2O on titanium oxides anchored within micropores of zeolites: effects of the structure of the active sites and the addition of Pt. *Journal of Physical Chemistry B* **101**: 2632-2636.

Anpo, M., Yamashita, H., Ikeue, K., Fujii, Y., Zhang, S. G., Ichihashi, Y., Park, D. R., Suzuki, Y., Koyano, K., Tatsumi, T. (1998) Photocatalytic reduction of CO_2 with H_2O on Ti-MCM-41 and Ti-MCM-48 mesoporous zeolite catalysts. *Catalysis Today* **44**: 327-332.

Asahi, R., Morikawa, T., Ohwaki, T., Aoki, K., Taga, Y. (2001). Visible-light photocatalysis in nitrogen-doped titanium oxides. *Science* **293**: 269.

Anderson, C., Bard, A. J. (1995). An improved photocatalyst of TiO_2/SiO_2 prepared by a sol-gel synthesis. *Journal of Physical Chemistry* **99**: 9882-9885.

Bhatkhande, D. S., Pangarkar, V. G., Beenackers, A. ACM. (2001). Photocatalytic degradation for environmental application: A review. *Journal of Chemical Technology & Biotechnology* **77**: 102.

Bellusi, G., Carati, A., Clerici, M. G., Meddinelli, G., Millini, R. (1992). Reaction of titanium silicalite with protic molecules and hydrogen peroxide. *Journal of Catalysis* **133**: 220.

Brinker, C. J., Scherer, G. W. (1990). Sol-gel science: the physics and chemistry of sol-gel processing. Academic Press. United Kingdom and San Diego.

Boone, J. M. (2000). *X-ray production, interaction, and detection in diagnostic imaging*. SPIE Press, Bellingham.

Bhattacharya, A. K., Pyke, D. R., Reynolds, R., Walker, G. S., Werrett, C. R. (1997). The use of O 1s charge referencing for the X-ray photoelectron spectroscopy of Al/Si, Al/ Ti and Al/Zr mixed oxides. *Journal of Materials Science Letters* **16**: 1-3.

Brunauer, S., Emmett, P. H., Teller, E. (1938). Adsorption of gases in multimolecular layers. *Journal of American Chemical Society* **60** (2): 309-319.

Barrett, C. S., Massalski, T. B. (1980). *Structure of metals, 3rd ed.* Pergamon Press. Oxford, New York, Ontario, Potts Point, Paris, and Hammerweg.

Cong, Y., Zhang, J., Chen, F., Anpo, M., He, D. (2007a). Preparation, photocatalytic activity, and mechanism of nano-TiO_2 codoped with nitrogen and iron. *Journal of Physical Chemistry C* **111**: 10618-10623.

Cong, Y., Zhang, J., Chen, F., Anpo, M. (2007b). Synthesis and characterization of nitrogen-doped TiO_2 nanophotocatalyst with high visible light activity. *Journal of Physical Chemistry C* **111**: 6976-6982.

Chen, X., Mao, S. S., (2007). Titanium dioxide nanomaterials: synthesis, properities, modifications, and applications. *Chemical Reviews* **107**: 2891-2959.

Choi, W., Termin, A., Hoffmann, M. R. (1994). The role of metal ion dopants in quantum-sized TiO_2: correlation between photoreactivity and charge carrier recombination dynamics. *Journal of Physical Chemistry* **98**: 13669-13679.

Corma, A. (1997). From microporous to mesoporous molecular sieve materials and their use in catalysis. *Chemical Reviews* **97**: 2373-2419.

Ciesla, U., Schuth, F. (1999). Ordered mesoporous materials. *Micoporous and Mesoporous Materials* **27**: 131-149.

Clerici, M. C. (1991). Oxidation of saturated hydrocarbons with hydrogen peroxide, catalysed by titanium silicalite. *Applied Catalysis* **68**: 249.

Chinchen, G. C., Hay, C. M., Vandervell, H. D., Waugh, K. C. (1987). The measurement of copper surface areas by reactive frontal chromatography. *Journal of Catalysis* **103**: 79-86.

Christopher, V., Thompson, E., Cornell, S. (2011). Carbon dioxide emission scenarios: limitation of the fossil fuel resource. *Procedia Environmental Sciences* **6**: 206-215.

Di Valentin, C., Pacchioni, G., Selloni, A., (2004). Origin of the different photoactivity of N-doped anatase and rutile TiO_2. *Physical Review B* **70**: 85116.

Diwald, O., Thompson, T. L., Zubkov, T., Goralski, E. G., Walck, S. D., Yates, J. T. (2004) Photochemical activity of nitrogen-doped rutile TiO_2(110) in visible light. *Journal of Physical Chemistry B* **108**: 6004.

Dey, G. R. (2007). Chemical reduction of CO_2 to different products during photo catalytic reaction on TiO_2 under diverse condition: an overview. *Journal of Natural Gas Chemistry* **16**: 217-226.

Debye, P., Scherrer, P. (1916). Interferenzen an regellos orientierten Teilchen im Rontgenlight. *Phys. Z.* **17**: 277.

de_Richter, R., Caillol, S. (2011). Fighting global warming: The potential of photocatalysis against CO_2, CH_4, N_2O, CFCs, tropospheric O_3, BC and other major contributors to climate change. *Journal of Photochemistry and Photobiology C* **12**: 1-19.

Fujishima, A., Rao, T. N., Tryk, D. A. (2000). Titanium dioxide photocatalysis. *Journal of Photochemistry and Photobiology C* **1**: 1-21.

Feng, X., Shankar, K., Varghese, O. K., Paulose, M., Latempa, T. J., Crimes, C. A. (2008). Vertically aligned single crystal TiO_2 nanowire arrays grown directly on transparent conducting oxide coated glass: synthesis details and applications. *Nano Letters* **8**: 3781-3786.

Gratzel, M. (1987). *Heterogeneous Photochemical Electron Transfer Reactions*. CRC Press: Boca Raton, FL.

Gao, B. (2008). The synthesis and characterization of TiO_2 and CNTs/TiO_2 nano-catalysts. Thesis for the degree of PhD, University of Nottingham.

Hamal, D. B., Klabunde, K. J. (2007). Synthesis, characterization, and visible light activity of new nanoparticle photocatalysts based on silver, carbon, and sulfer-doped TiO_2. *Journal of Colloid and Interface Science* **311**: 514-522.

Ho, W., Yu, J. C., Lee, S. (2006). Low-temperature hydrothermal synthesis of S-doped TiO_2 with visible light photocatalytic activity. *Journal of Solid State Chemistry* **179**: 1171-1176.

Hara, M., Kondo, T., Komoda, M., Ikeda, S., Shinohara, K., Tanaka, A., Kondo, J. N., Domen, K. (1998). Cu_2O as a photocatalyst for overall water splitting under visible light irradiation. *Chemical Communications*: 357.

Hamidipour, M., Mostoufi, N., Sotudeh-Gharebagh, R. (2005). Modeling the synthesis section of an industrial urea plant. *Chemical Engineering Journal* **106**: 249-260.

Hwang, J. S., Chang, J. S., Park, S. E., Ikeue, K., Anpo, M. (2005). Photoreduction of carbon dioxide on surface functionalized nanoporous catalysts. *Topics in Catalysis* **35**: 311.

Hull, A. W. (1919). A new method of chemical analysis. *Journal of American Chemical Society* **41**: 1168.

Hanawalt, J. D., Rinn, H. W., Frevel, L. K. (1938). Chemical analysis by X-ray diffraction. *Industrial Engineering Chemistry, Analytical Edition* **10**: 457.

Henry, D., Eby, N., Goodge, J., Mogk, D. (2010). *X-ray reflection in accordance with Bragg's law.* (Online). Integrating Research and Education. Avaiable at: <http://serc.carleton.edu/research_education/geochemsheets/BraggsLaw.html> (Accessed Nov. 2011).

Huang, L., Peng, F., Wang, H., Yu, H., Li, Z. (2009). Preparation and characterization of $C_{u2}O/TiO_2$ nano-nano heterostructure photocatalysts. *Catalysis Communications* **10**: 1839-1843.

Inoue, T., Fujishima, A., Konishi, S., Honda, K. (1979). Photoelectrocatalytic reduction of carbon dioxide in aqueous suspensions of semiconductor powders. *Nature* **277**: 637.

Indrakanti, V. P., Kubicki, J. D., Schobert, H. H. (2009). Photoinduced activation of CO_2 on Ti-based heterogeneous catalysts: Current state, chemical physics-based insights and outlook. *Energy & Environmental Science* **2**: 745-758.

Ishitanij, O., Inoue, C., Suzuki, Y., Ibusuki, T. (1993). Photocatalytic reduction of carbon dioxide to methane and acetic acid by an aqueous suspension of metal-deposited TiO_2. *Journal of Photochemistry and Photobiology A* **72**: 269-271.

Ikeue, K., Yamashita, H., Anpo, M., Takewaki, T. (2001). Photocatalytic Reduction of CO_2 with H_2O on Ti–β Zeolite Photocatalysts: Effect of the Hydrophobic and Hydrophilic Properties. *Journal of Physical Chemistry B* **105**: 8350–8355.

Ikeue, K., Nozaki, S., Ogawa, M., Anpo, M. (2002a). Characterization of self-standing Ti-containing porous silica thin films and their reactivity for the photocatalytic reduction of CO_2 with H_2O. *Catalysis Today* **74**: 241-248.

Ikeue, K., Nozaki, S., Ogawa, M., Anpo, M. (2002b). Photocatalytic reduction of CO_2 with H_2O on Ti-containing porous silica thin film photocatalysts. *Catalysis Letters* **80**: 111.

Irie, H., Watanabe, Y., Hashimoto, K. (2003a). Carbon-doped anatase TiO_2 powders as a visible-light sensitive photocatalyst. *Chemistry Letters* **32**: 772.

Irie, H., Watanabe, Y., Hashimoto, K. (2003b). Nitrogen-concentration dependence on photocatalytic activity of $TiO_{2-x}N_x$ powders. *Journal of Physical Chemistry B* **107**: 5483.

Jiang, Z., Xiao, T., Kuznetsov, V. L., Edwards, P. P. (2010). Turning carbon dioxide into fuel. *Philosophical Transactions of Royal Society A* **368**: 3343-3364.

Jenkins, R., Snyder, R. L. (1996). *Introduction to X-ray powder diffractometry*. John Wiley & Sons Inc. New York.

Jung, K. Y., Park, S. B. (2000). Park, Enhanced photoactivity of silica-embedded titania particles prepared by sol-gel process for the decomposition of trichloroethylene. *Applied Catalysis B* **25**: 249-256.

Kohno, Y., Hayashi, H., Takenaka, S., Tanaka, T., Funabiki, T., Yoshida, S. (1999) Photo-enhanced reduction of carbon dioxide with hydrogen over Rh/TiO_2. *Journal of Photochemistry and Photobiology A* **126**: 117-123.

Kohno, Y., Yamamoto, T., Tanaka, T., Funabiki, T. (2001). Photoenhanced reduction of CO_2 by H_2 over Rh/TiO_2 characterization of supported Rh species by means of infrared and X-ray absorption spectroscopy. *Journal of Molecular Catalysis A* **175**: 173-178.

Kaneco, S., Shimizu, Y., Ohta, K., Mizuno, T. (1998). Photocatalytic reduction of high pressure carbon dioxide using TiO_2 powders with a positive hole scavenger. *Journal of Photochemistry and Photobiology A* **115**: 223.

Kaneco, S., Kurimoto, H., Shimizu, Y., Ohta, K., Mizuno, T. (1999). Photocatalytic reduction of CO_2 using TiO_2 powders in supercritical fluid CO_2. *Energy* **24**: 21.

Koci, K., Obalova, L., Matejova, L., Placha, D., Lacny, Z., Jirkovsky, J., Solcova, O. (2009). Effect of TiO_2 particle size on the photocatalytic reduction of CO_2. *Applied Catalysis B* **89**: 494-502.

Koci, K., Mateju, K., Obalova, L., Krejcikova, S., Lacny, Z., Placha, D., Capek, L., Hospodkova, A., Solcova, O. (2010). Effect of silver doping on the TiO_2 for photoccatalytic reduction of CO_2. *Applied Catalysis B* **96**: 239-244.

Kresge, C. T., Leonowicz, M. E., Roth, W. J., Vartuli, J. C., Beck, J. S. (1992) Ordered mesoporous molecular sieves synthesized by a liquid-crystal template mechanism. *Nature* **359**: 22.

Khan, S. U. M., Al-Shahry, M., Ingler, W. B. (2002). Efficient photochemical water splitting by a chemically modified n-TiO_2. *Science* **297**: 2243.

Kruk, M., Jaroniec, M. (2001). Gas adsorption characterization of ordered organic-inorganic nanocomposite materials. *Chemistry of Materials* **13**: 3169-3183.

Lin, X., Rong, F., Ji, X., Fu, D. (2011). Carbon-doped mesoporous TiO_2 film and its photocatalytic activity. *Microporous and Mesoporous Materials* **142**: 276-281.

Lin, W., Han, H., Frei, H. (2004). CO_2 splitting by H_2O to CO and O_2 under UV light in TiMCM-41 silicate sieve. *Journal of Physical Chemistry B* **108**: 18269-18273.

Lindgren, T., Mwabora, J. M., Avendano, E., Jonsson, J., Granqvist, C. G., Lindquist, S. E. (2003). Photoelectrochemical and optical properties of nitrogen doped titanium dioxide films prepared by reactive DC magnetron sputtering. *Journal of Physical Chemistry A* **107**: 5709.

Linsebigler, A. L., Lu, G., Yates, J. T. (1995). Photocatalysis on TiO_2 surface: principles, mechanisms, and selected results. *Chemical Reviews* **95**: 735-758.

Li, Y., Wang, W. N., Zhan, Z., Woo, M. H., Wu, C. Y., Biswas, P. (2010). Photocatalytic reduction of CO_2 with H_2O on mesoporous silica supported Cu/TiO_2 catalysts. *Applied Catalysis B* **100**: 386-392.

Li, B., Wang, X., Yan, M., Li, L. (2003). Preparation and characterization of nano-TiO_2 powder. *Materials Chemistry and Physics* **78**: 184-188.

Luo, D., Bi, Y., Kan, W., Zhang, N., Hong, S. (2011). Copper and cerium co-doped titanium dioxide on catalytic photo reduction of carbon dioxide with water: Experimental and theoretical studies. *Journal of Molecular Structure* **994**: 325-331.

Lee, J. E., Oh, S., Park, D. (2004). Synthesis of nano-sized Al doped TiO_2 powders using thermal plasma. *Thin Solid Films* **457**: 230-234.

Lee, K., Lee, N. H., Shin, S. H., Lee, H. G., Kim, S. J. (2006). Hydrothermal synthesis and photocatalytic characterizations of transition metals doped nano TiO_2 sols. *Materials Science and Engineering: B* **129**: 109-115.

Li, W., Frenkel, A. I., Woicik, J. C., Ni, C., Ismat Shah, S. (2005). Dopant location identification in Nd^{3+}-doped TiO_2 nanoparticles. *Physical Review B* **72**: 155315.

Ni, M., Leung, M., Leung, D. Y. C., Sumathy, K. (2007). A review and recent developments in photocatalytic water-splitting using TiO_2 for hydrogen production. *Renewable and Sustainable Energy Reviews* **11**: 401-425.

Nagaveni, K., Sivalingam, G., Hegde, M. S., Madras, G. (2004). Solar photocatalytic degradation of dyes: high activity of combustion synthesized nano TiO_2, *Applied Catalysis B* **48**: 83-93.

Nguyen, T. V., Wu, J. C. S. (2008a). Photoreduction of CO_2 in an optical-fiber photoreactor: Effects of metals addition and catalyst carrier. *Applied Catalysis A* **335**: 112-120.

Nguyen, T. V., Wu, J. C. S. (2008b). Photoreduction of CO_2 to fuels under sunlight using optical-fiber reactor. *Solar Energy Materials & Solar Cells* **92**: 864-872.

Noworyta, K., Augustynski, J. (2004). Spectral photoresponses of carbon-doped TiO_2 film Electrodes. *Electrochemical and Solid–State Letters* **7**: 31.

Nefedov, V. I. Translated by Shartse, N. G. (1988). *X-ray photoelectron spectroscopy of solid surfaces*. VSP BV. Utrecht, Netherlands.

Narita, K., Takeyawa, N., Kobayashi, H., Toyoshima, I. (1982). Adsorption of nitrous oxide on metallic copper catalysts. *Reaction Kinetics and Catalysis Letters* **19**: 91.

Metz, B., Davidson, O., de Coninck, H. C., Loos, M., Meyer, L. A. (2005). *IPCC Special Report on Carbon Dioxide Capture and Storage*. Cambridge University Press. United Kingdom and New York.

Mikkelsen, M., Jorgensen, M., Krebs, F. C. (2010). The teraton challenge. A review of fixation and transformation of carbon dioxide. *Energy & Environmental Science* **3**: 43-81.

Ohno, T., Sarukawa, K., Tokieda, K., Matsumura, M. (2001). Morphology of a TiO_2 photocatalyst (Degussa, P25) consisting a anatase and rutile crystalline phases. *Journal of Catalysis* **203**: 82-86.

Park, J. H., Kim, S., Bard, A. J., Novel carbon-doped TiO_2 nanotube arrays with high aspect ratio for efficient solar water splitting. *Nano Letters* **6**: 24-28.

Pecharsky, V. K., Zavalij, P. Y. (2009). *Fundamentals of powder diffraction and structural characterization of materials*. Springer Science + Business Media. New York.

Rhoderick, E. H., Williams, R. H. (1988). *Metal-Semiconductor Contacts*, 2nd ed. Oxford University Press, New York.

Rensmo, H., Lindstrom, H., Hagfeldt, A., Lindquist, S. (1997). Lithium intercalation in nanoporous anatase TiO2 studies with XPS. *Journal of Physical Chemistry B* **101**: 3087-3090.

Sathish, M., Viswanathan, B., Viswanath, R. P., Gopinath, C. S. (2005). Synthesis, characterization, electronic structyre, and photocatalytic activity of nitrogen-doped TiO_2 nanocatalyst. *Chemistry Materials* **17**: 6349-6353.

Sakthivel, S., Janczarek, M., Kisch, H. (2004). Visible light activity and photoelectrochemical properties of nitrogen-doped TiO_2. *Journal of Physical Chemistry B* **108**: 19384-19387.

Serpone, N. (2006). Is the band gap of pristine TiO_2 narrowed by anion- and cation-doping of titanium dioxide in second-generation photocatalysts? *Journal of Physical Chemistry B* **110**: 24287-24293.

Serpone, N., Lawless, D., Khairlutdinov, R., Pelizzetti, E. (1995). Size effects on the photophysical properties of colloidal anatase TiO_2 particles: Size quantization versus direct transitions in this indirect semiconductor? *Journal of Physical Chemistry* **99**: 16655.

Shioya, Y., Ikeue, K., Ogawa, M., Anpo, M. (2003). Synthesis of transparent Ti-containing mesoporous silica thin film meterials and their unique photocatalytic activity for the reduction of CO_2 with H_2O. *Applied Catalysis A* **254**: 251-259.

Solymosi, F., Tombacz, I. (1994). Photocatalytic reaction of $H_2O + CO_2$ over pure and doped Rh/TiO_2. *Catalysis Letters* **27**: 61-65.

Sclafani, A. (1996). Comparison of the photoelectronic and photocatalytic activities of various anatase and rutile forms of titania in pure liquid organic phases and in aqueous solutions. *Journal of Physical Chemistry* **100**: 13655-13661.

Sakakura, T., Choi, J., Yasuda, H. (2007). Transformation of carbon dioxide. *Chemical Reviews* **107**: 2365-2387.

Sing, K. S. W., Everett, D. H., Haul, R. A. W., Moscou, L., Pierotti, R. A., Rouquerol, J., Siemieniewska, T. (1985). Reporting physisorption data for gas/solid systems with special reference to the determination of surface area of porosity. *Pure & Applied Chemistry* **57**: 603-619.

Sturrock, P. A. (1994). Plasma physics: an introduction to the theory of astrophysical, geophysical, and laboratory plasmas. Cambridge University Press. Cambridge, New York, and Oakleigh.

Scholten, J. J. F., Konvalinka, J. A. (1969). Reaction of nitrous oxide with copper surfaces. *Transactions of the Faraday Society* **65**: 2465.

Turchi, C. S., Ollis, D. (1990). Photocatalytic degradation of organic water contaminants: Mechanisms involving hydroxyl radical attack. *Journal of Catalysis* **122**: 178-192.

Tan, S. S., Zou, L., Hu, E. (2006). Photocatalytic reduction of carbon dioxide into gaseous hydrocarbon using TiO_2 pellets. *Catalysis Today* **115**: 269-273.

Tseng, I. H., Chang, W. C., Wu, J. C. S. (2002). Photoreduction of CO_2 using sol-gel derived titania and titania-supported copper catalysts. *Applied Catalysis B* **37**: 37-48.

Tseng, I. H., Wu, J. C. S. (2004). Chemical states of metal-loaded titania in the photoreduction of CO_2. *Catalysis Today* **97**: 113-119.

Trentler, T. J., Denler, T. E., Bertone, J. F., Agrawal, A., Colvin, V. (1999). Synthesis of TiO_2 nanocrystals by nanhydrolytic solution-based reactions. *Journal of American Chemical Society* **121**: 1613-1614.

Thomas, R. (2008). *Practical guide to ICP-MS: A tutorial for beginners*. CRC Press, USA.

Torrent, J., Barron, V. (2008). Diffuse reflectance spectroscopy. In: Ulery, A. L., Drees, L. R., ed. (2008). *Methods of soil analysis part 5-Mineralogical methods*. Soil Science Society of America, Madison, Wisconsin, USA. Ch. 13.

Tian, G. H., Fu, H. G., Jing, L. Q., Xin, B. F., Pan, K. (2008). Preparation and characterization of stable biphase TiO_2 photocatalyst with high crystallinity, large surface area, and enhanced photoactivity. *Journal of Physical Chemistry C* **112**: 3083-3089.

United States Environmental Protection Agency (EPA). (2010). *Natural sources and sinks of carbon dioxide*. (Online). EPA. Available at: <http://www.epa.gov/climatechange/emissions/co2_natural.html> (Accessed Nov. 2011).

Umebayashi, T., Yamaki, T., Tanaka, S., Asai, K. (2003a). Visible light-induced degradation of methylene blue on S-doped TiO_2. *Chemistry Letters* **32**: 330.

Umebayashi, T., Yamaki, T., Yamamoto, S., Miyashita, A., Tanaka, S., Sumita, T., Asai, K. (2003b). Sulfur-doping of rutile-titanium dioxide by ion implantation: Photocurrent spectroscopy and first-principles band calculation studies. *Journal of Applied Physics* **93**: 5156.

Umebayashi, T., Yamaki, T., Itoh, H., Asai, K. (2002). Band gap narrowing of titanium dioxide by sulphur doping. *Applied Physics Letters* **81**: 454.

Usubharatana, P., McMartin, D., Veawab, A., Tontiwachwuthikul, P. (2006) Photocatalytic process for CO_2 emission reduction from industrial flue gas stream. *Industrial & Engineering Chemistry Research* **45**: 2558-2568.

Varghese, O. K., Paulose, M., LaTempa, T. J., Crimes, C. A. (2009). High-rate solar photocatalytic conversion of CO_2 and water vapour to hydrocarbon fuels. *Nano Letters* **9**: 731-737.

Wang, H., Lewis, J. P. (2006). Second-generation photocatalytic materials: anion-doped TiO_2. *Journal of Physics: Condensed Matter* **18**: 421-434.

Wang, H., Lewis, J. P. (2005). Effects of dopant states on photoactivity in carbon-doped TiO_2. *Journal of Physics: Condensed Matter* **17**: 209.

Wu, J. C. S., Chen, C. H. (2004). A visible-light response vanadium-doped titania nanocatalyst by sol-gel method. *Journal of Photochemistry and Photobiology A* **163**: 509-515.

Wu, J. C. S., Yeh, C. Y. (2001). Sol-gel-derived photosensitive TiO_2 and Cu/TiO_2 using homogeneous hydrolysis technique. *Journal of Materials Research* **16**: 2.

Wu, J. C. S., Lin, H. M., Lai, C. L. (2005). Photo reduction of CO_2 to methanol using optical-fiber photoreactor. *Applied Catalysis A* **296**: 194-200.

Waseda, Y., Matsubara, E., Shinoda, K. (2011). X-ray diffraction crystallography. Springer. Verlag, Berlin, and Heidelberg.

Williams, D. B., Carter, C. B. (1996). *Transmission electron microscopy: A textbook for materials science*. Plenum Press. New York, London.

Weckhuysen, B. M., Schoonheydt, R. A. (1999). Recent progress in diffuse reflectance spectroscopy of supported metal oxide catalysts. *Catalysis Today* **49**: 441-451.

Xu, Y., Schoonen, M. A. A. (2000). The absolute energy positions of conduction and valence bands of selected semiconducting minerals. *American Mineralogist* **85**: 543-556.

Xie, T. F., Wang, D. J., Zhu, L. J., Li, T. J., Xu, Y. J. (2001). Application of surface photovoltage technique in photocatalysis studies on modified TiO_2 photo-catalysts for photo-reduction of CO_2. *Materials Chemistry and Physics* **70**: 103-106.

Xin, B., Jing, L., Ren, Z., Wang, B., Fu, H. (2005). Effects of simultaneously doped and deposited Ag on the photocatalytic activity and surface states of TiO_2. *Journal of Physical Chemistry B* **109**: 2805-2809.

Yamamoto, T., Yamashita, Y., Tanaka, I., Matsubara, F., Muramatsu, A. (2004). Electronic states of sulphur doped TiO_2 by first principles calculations, *Materials Transactions* **45**: 1987.

Yamashita, H., Fujii, Y., Ichihashi, Y., Zhang, S. G., Ikeue, K., Park, D. R., Koyano, K., Tatsumi, T., Anpo, M. (1998). Selective formation of CH_3OH in the photocatalytic reduction of CO_2 with H_2O on titanium oxides highly dispersed within zeolites and mesoporous meolecular sieves. *Catalysis Today* **45**: 221-227.

Yamashita, H., Fujii, Y., Ichihashi, Y., Zhang, S. G., Ikeue, K., Park, D. R., Koyano, K., Tatsumi, T., Anpo, M. (1994a). Photocatalytic reduction of CO_2 with H_2O on Ti-MCM-41 and Ti-MCM-48 mesoporous zeolite catalysts. *Catalysis Today* **45**: 221.

Yamashita, H., Kamada, N., He, H., Tanaka, K., Ehara, S., Anpo, M. (1994b). Reduction of CO_2 with H_2O on $TiO_2(100)$ and $TiO_2(110)$ Single Crystals under UV-irradiation. *Chemistry Letters* **23**: 855–858.

Yang, X., Xiao, T., Edwards, P. (2011). The use of products from CO_2 photoreduction for improvement of hydrogen evolution in water splitting. *International Journal of Hydrogen Energy* **36**: 6546-6552.

Yang, Y. Z., Chang, C. H., Idriss, H. (2006). Photo-catalytic production of hydrogen from ethanol over M/TiO_2 catalysts (M = Pd, Pt or Rh). *Applied Catalysis B* **67**: 217-222.

Yahaya, A. H., Gondal, M. A., Hameed, A. (2004). Selective laser enhanced photocatalytic conversion of CO_2 into methanol. *Chemical Physics Letters* **400**: 206-212.

Yang, H. C., Lin, H. Y., Chien, Y. S., Wu, J. C. S., Wu, H. H. (2009). Mesoporous TiO_2/SBA-15, and Cu/TiO_2/SBA-15 composite photocatalysts for photoreduction of CO_2 to methanol. *Catalysis Letters* **131**: 381-387.

Yu, J., Zhao, X., Zhao, Q. (2001). Photocatalytic activity of nanometer TiO_2 thin films prepared by the sol-gel method. *Materials Chemistry and Physics* **69**: 25-29.

Yang, J., Mei, S., Ferreira, J. M. F. (2001). Hydrothermal synthesis of TiO_2 nanopowders from tetraalkylammonium hydroxide peptized sols. *Materials Science and Engineering C* **15**: 183.

Zhang, Q., Li, Y., Ackerman, E. A., Gajdardziska-Josifovska, M., Li, H. (2011). Visible light responsive iodine-doped TiO_2 for photocatalytic reduction of CO_2 to fuels. *Applied Catalysis A* **200**: 195-202.

Zhao, Z., Fan, J., Xie, M., Wang, Z. (2009). Photo-catalytic reduction of carbon dioxide with in-situ synthesized CoPc/TiO_2 under visible light irradiation. *Journal of Cleaner Production* **17**: 1025-1029.

Zhang, Q. H., Han, W. D., Hong, Y. J., Yu, J. G. (2009a). Photocatalytic reduction of CO_2 with H_2O on Pt-loaded TiO_2 catalyst. *Catalysis Today* **148**: 335-340.

Zhang, J., Xiao, X., Nan, J. (2009b). Hydrothermal-hydrolysis synthesis and photocatalytic properties of nano-TiO_2 with an adjustable crystalline structure. *Journal of Hazardous Materials* **176**: 617-622.

Zhao, D., Feng, J., Huo, Q., Melosh, N., Fredrickson, G. H., Chmelka, B. F., Stucky, G. D. (1998). Triblock copolymer syntheses of mesoporous silica with periodic 50 to 300 angstrom pores. *Science* **279**: 23.

Zhang, Z., Wang, C. C., Zakaria, R., Ying, J. Y. (1998). Role of particle size in nanocrystalline TiO_2-based photocatalysts. *Journal of Physical Chemistry B* **102**: 10871-10878.

Zlateva, G., Martinova, Z. (2008). *Microstructure of metals and alloys: An atlas of transmission electron microscopy images*. CRC Press. Boca Raton, London, and New York.

Zhang, Y. J., Yan, W., Wu, Y. P., Wang, Z. H. (2008). Synthesis of TiO_2 nanotubes coupled with CdS nanoparticles and production of hydrogen by photocatalytic water decomposition, *Materials Letters* **62**: 3846-3848.

Zhu, J., Chen, F., Zhang, J., Chen, H., Anpo, M. (2006). Fe^{3+}-TiO_2 photocatalysts prepared by combining so-gel method with hydrothermal treatment and their characterization. *Journal of Photochemistry and Photobiology A* **180**: 196-204.

Chapter 3: Methodology

This chapter describes the methodology of this work, which includes the catalyst synthesis procedure (Section 3.1), sample preparation procedure and analytical conditions for the catalyst characterization (Section 3.2), photo-reactor design (Section 3.3), and methodology involved in conducting the CO_2 photoreduction experiments (Section 3.4).

3.1 Catalyst synthesis procedure

As described in Section 2.5, this work chose titanium dioxide (TiO_2), one of the most practical and widely used semiconductors, to be the photocatalyst for CO_2 photoreduction. These TiO_2 were modified with different metals (e. g. copper (Cu), rhodium (Rh), and zinc (Zn)) to investigate the effects of metal modification on TiO_2 for CO_2 photoreduction. Sol-gel process was used to prepare the nano-sized pure and metal modified TiO_2 (SG TiO_2 and M/TiO_2) in this work. This is because the TiO_2 catalysts derived from such process had been proven to be able to effectively initiate CO_2 photoreduction (Wu and Yeh, 2001; Tseng et al., 2002; Nguyen and Wu, 2008). This section describes the procedure of the sol-gel process adopted in this work for the TiO_2 synthesis.

The sol-gel process adopted in this work was developed by Wu et al. (Wu and Yeh, 2001; Wu et al., 2001). The mechanism of this sol-gel process has been described in Section 2.3.2.1.1. In comparison to the traditional sol-gel processes that add water directly into the titanium alkoxide to initiate the hydrolysis, the hydrolyzing water of this process was homogeneously and slowly released by the esterification of n-butanol and acetic acid. This method of releasing hydrolyzing water avoids the rapid precipitation or formation of the unstable colloidal sols during the condensation step of the sol-gel process, which allows the synthesis of uniform nano-sized TiO_2 particles (Wu et al., 2001).

In this study, titanium(IV) n-butoxide ($Ti(OC_4H_9)_4$, Acros Organics, 99%) was used as the titanium precursor. The metal precursors included copper(II) chloride dihydrate ($CuCl_2 \cdot 2H_2O$, CertiFied AR, 99%), zinc chloride ($ZnCl_2$, Acros Organics, 99.99%), and rhodium(II) acetate ($C_8H_{16}O_{10}Rh_2$, Aldrich, 99.99%). In a typical procedure of M/TiO_2 synthesis (shown in Fig. 3.1), the desired amount of metal precursor was firstly homogeneously dissolved in 0.08 mol of n-butanol (C_4H_9OH, CertiFied AR, 99.5%). Then such n-butanol was homogeneously mixed with 0.08 mol of acetic acid (CH_3COOH, Acros Organics, glacial 99.8%) and 0.02 mol of titanium(IV) n-butoxide in a disposable 75 ml glass vial. Such vial was tightly closed in order to avoid the titanium precursor being hydrolysed by ambient moisture. Then the precursor solution was stirred by magnetic stirrer at 70 RPM for 6 hr. The hydrolysis reaction was completed during this 6-hr stirring, and this was proven by the

monitoring of the pH value of the precursor solution (conducted by a Fisher Scientific AR10 pH meter, data shown in Section 4.1.1). After the hydrolysis, the precursor solution was heat treated in air by using a furnace (Carbolite, chamber furnace CWF model). The temperature was firstly increased at a rate of 3 °C/min to 150 °C and held isothermally at this temperature for 2 hr to dry the precursor. The temperature was then increased again at 5 °C/min to 500 °C and held isothermally for 1 hr to burn off the organic residues and transform the titanium precursor into TiO_2. A thermo-gravimetric analysis (TGA) was conducted to confirm that if the organic residues had been truly burned off. Such analysis was conducted at a TA Q600 TGA within an air flow at 100 ml/min (data shown in Section 4.1.2). After the heat treatment, the TiO_2 samples were crushed in a mortar for 20 min into powder form.

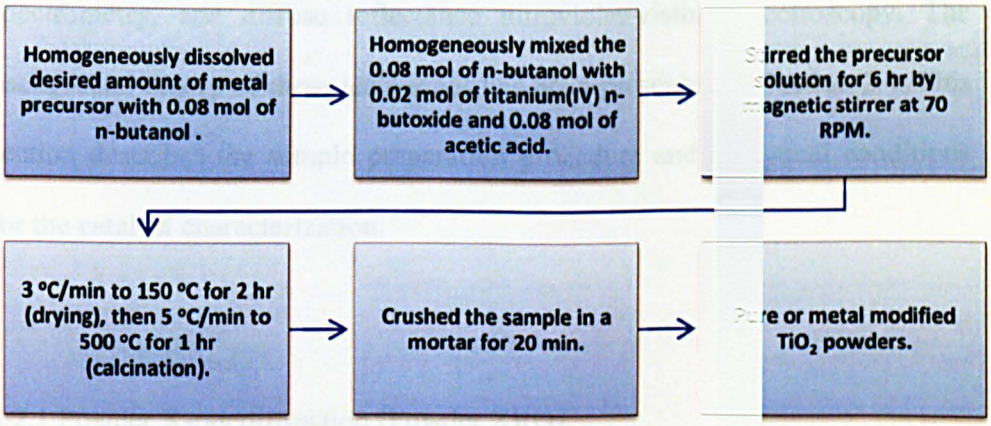

Figure 3.1: Sol-gel synthesis procedure of pure or metal modified TiO_2 catalysts (SG TiO_2 or M/TiO_2). The metal precursor was dissolved in n-butanol beforehand, only if it was to synthesize M/TiO_2.

A series of M/TiO_2 with different mass ratios ($\frac{\text{Mass of metal}}{\text{Mass of } TiO_2} \times 100$) were synthesized in this work. They included Cu/TiO_2 (ratio ranged from 0.006 wt% to 0.5 wt%), Rh/TiO_2 (ratio ranged from 0.003 wt% to 0.5 wt%), Zn/TiO_2 (ratio ranged from 0.05 wt% to 0.5 wt%), and $Cu/Rh/TiO_2$ (with fixed 0.03 wt% Cu and 0.003 wt%-0.02 wt% Rh).

3.2 Sample preparation procedure and analytical conditions for catalyst characterization

A series of techniques were used to analyse the TiO_2 synthesized in this work. These analytical techniques included powder X-ray diffraction, X-ray photoelectron spectroscopy, transmission electron microscopy, N_2 adsorption measurement, Cu surface area measurement, inductively coupled plasma mass spectrometry, and diffuse reflectance ultraviolet-visible spectroscopy. The background theory of these techniques has been presented in Section 2.4. This section describes the sample preparation procedure and analytical conditions for the catalyst characterization.

3.2.1 Powder X-ray diffraction (Powder XRD)

In this study, powder XRD was used to determine the crystalline structures of TiO_2 in order to identify if the TiO_2 samples synthesized in this work were

anatase or rutile, and whether the added metals were doped into the lattices or loaded on the surfaces of M/TiO_2. Meanwhile, the crystalline sizes of TiO_2 were calculated by Scherrer Formula (Equation and example are introduced in Section 2.4.1).

The powder XRD analysis was conducted by Mr. David Clift in the Department of Chemical and Environmental Engineering, University of Nottingham. In a typical analysis, the catalyst powder sample was loaded onto an indented stainless steel plate and scanned by the powder XRD instrument (HILTONBROOKS X-ray powder diffraction) with Cu Kα radiation at 1.5406 Å. The scanning was run over a 2θ range of 5-65° with a scanning speed of 2° per min. The result of the analysis was assessed by Jade 5.0 software to identify the crystalline structure of the analyte by comparing the XRD pattern of the sample with the JCPDS database. The position and full width at half maximum (FWHM) of the most intense peak within the XRD pattern was recorded to estimate the crystallite size and to assess if the crystalline structures of the M/TiO_2 was modified by the added metal.

3.2.2 Transmission electron microscopy (TEM)

In this work, TEM was used to study the morphology of TiO_2 (e.g. particle size). Before the TEM analysis, the analysed samples needed to be prepared, and such sample must be thin enough to allow the incident electron beam to

penetrate it. The sample preparation was conducted by the author of this thesis. Firstly, 0.003 g of the catalyst sample (in powder form) was placed in 5 ml of acetone and ultrasonically shaked for 2 min to allow the sample to be fully suspended. Then a copper grid (Agar Scientific) was marinated in the suspension and then dried at ambient temperature. This process could allow ultra thin sample to be mounted on the copper grid for the TEM analysis.

The TEM analysis was conducted by Dr. Michael Fay at the Nanoscience and Nanotechnology Centre, University of Nottingham. When conducting the analysis, the TEM instrument (JEOL 2100F) was operated with an acceleration voltage at 200 kV, and the images were obtained by a Gatan Orius camera. The resulting TEM images were processed by ImageJ software (Version 1.43u).

3.2.3 Inductively coupled plasma mass spectrometry (ICP-MS)

ICP-MS was used in this study to measure the elemental ratios of M/TiO_2 in order to find out whether the actual elemental ratios of these samples were consistent with their nominal values.

The analysed M/TiO_2 needed to be homogenously dissolved before ICP-MS analysis, and it was reported by DuPont (2011) that TiO_2 was dissolvable by hot concentrated sulphuric acid. The TiO_2 dissolution was conducted by the

author of this thesis. First of all, 0.003 g of the M/TiO_2 powders was suspended in 10 ml of concentrated sulphuric acid (Fisher Scientific, Trace-Metal) within a test tube. Such test tube was heated at 180 °C for 5 min by a test tube heater. After the heat treatment, the suspension inside the test tube became transparent and the M/TiO_2 powders were homogenously dissolved by the hot concentrated sulphuric acid. The sulphuric acid solution of the M/TiO_2 was then diluted to 2 % with deionized water. Such diluted sample was ready for ICP-MS analysis.

The ICP-MS analysis was conducted by Dr. Scott Young at the School of Bioscience, University of Nottingham. The analysed sample was introduced via an autosampler (Cetac ASX-520) into the ICP-MS instrument (Thermo-Fisher Scientific X-Series^{II}) for the analysis. The data were processed by Plasmalab software (Thermo-Fisher Scientific) and the ratios of the different elements in the analysed sample could be calculated.

3.2.4 X-ray photoelectron spectroscopy (XPS)

The M/TiO_2 of this study were analysed by XPS. Such analysis was conducted to determine the chemical states of the added metals and measure the elemental ratios of the surfaces of M/TiO_2.

The XPS analysis was conducted by Prof. Adam Lee and Dr. Karen Wilson at the School of Chemistry, Cardiff University. The analysed sample powders were mounted into an indented stainless steel plate at ambient conditions. The sample was then scanned by the XPS instrument (Kratos AXIS HSi) equipped with a charge neutraliser and Mg Kα X-ray source. Spectra were recorded using an analyser with the pass energy of 40 eV and X-ray power of 225 W. The XPS data were processed by CasaXPS software (Version 2.3.15).

3.2.5 Diffuse reflectance ultraviolet-visible spectroscopy (DR UV-Vis)

DR UV-Vis spectroscopy analysis was conducted to determine the band-gap energies of the TiO_2 samples. Meanwhile, the chemical states of the metals added to the surfaces of M/TiO_2 could be also determined by such analysis.

The DR UV-Vis spectroscopy of this work was conducted by the author of this thesis at the Department of Chemical and Environmental Engineering, University of Nottingham by using a diffuse reflective UV-Vis spectrometer (Varian, Cary 300). In a typical analysis, the TiO_2 powders synthesized in this work was loaded into an indented flat quartz sample holder. The sample holder was then inserted into the instrument and scanned by a beam of light with wavelength ranging from 200 to 800 nm. The resulting graph of the UV-Vis spectroscopy was then saved and processed by Cary WinUV software (Version 3.1).

3.2.6 N_2 adsorption measurement

The N_2 adsorption measurements were conducted mainly to evaluate the specific surface areas of the TiO_2 samples synthesized in this work. Such measurements were conducted at the Department of Chemical Engineering, National Taiwan University. The N_2 isotherms were determined at 196.15 °C (77 K). The analysed TiO_2 was dried at 80 °C and evacuated under vacuum overnight in an ASAP 2020 sorptometer before the measurement. The specific surface area of the analysed sample was then calculated by the BET model using the adsorption data in the relative pressure range of 0.05-0.35, and the amount of the N_2 adsorbed at the relative pressure of 0.974 was used to determine the total pore volume.

3.2.7 Cu surface area measurement

In this study, Cu was loaded on the surface of TiO_2 (proven by XRD, Section 4.2.2.2) in order to improve the catalytic performance of TiO_2 for CO_2 photoreduction. The specific surface area (m^2/g) of the loaded Cu and the Cu dispersion (the ratio between the number of the surface Cu atoms and the number of the total Cu atoms) on the TiO_2 surface were evaluated by using N_2O as adsorbate (as introduced in Section 2.4.5).

This measurement was conducted by Mr. Christopher Parlett and Prof. Adam Lee at the School of Chemistry, Cardiff University using a Quantachrome ChemBET™ TPR/TPD pulse-chemisorption system connected with a MKS LM80 mass spectrometer. Because the loaded Cu on Cu/TiO_2 catalysts of this work was at the chemical state of Cu_2O (proven via powder XRD and XPS, Sections 4.2.2.2 and 4.2.3.2), it needed to be reduced into metallic Cu by H_2 before reacting with N_2O. The process is described as follow: (1) First of all, 0.2 g of the analysed catalyst with known ratio of Cu loading was outgassed at 110 °C for 30 min in the flowing helium with a flow rate of 20 ml/min. (2) The catalyst was then reduced at 280 °C for 30 min in flowing 10 % H_2 in He with a flow rate of 20 ml/min. (3) After the reduction, the catalyst was cooled to 65 °C, then pure N_2O (Air Products) was pulsed over the catalyst to react with the surface of the loaded Cu which had been reduced into metallic Cu and the resulting N_2O and N_2 were monitored by the mass spectrometer. (4) The measurement was stopped when the peak of N_2O recorded by mass spectrometer was constant which indicated that the surface of the loaded Cu had been fully oxidized by N_2O.

After the analysis, the number of N_2O molecules adsorbed by the surface of the loaded Cu could be determined and such value could be used to determine the specific surface area and dispersion of Cu.

3.3 Photo-reactor design

The CO_2 photoreduction experiments were conducted in a photo reactor. The design of this reactor was modified from the one reported by Tseng et al. (2002). Comparing the reactor of Tseng et al., the reactor of this work had smaller capacity (316.93 ml comparing to 500 ml) and the reactor lid of this study was made of a material with better chemical stability (Teflon compared to poly(methyl methacrylate) (PMMA)). This section describes the design of the reactor used in this work.

Fig 3.2 shows the diagram and actual picture of the reactor used in this study. The primary components of the photo-reactor included a lid made of Teflon with a quartz tube fixed in the centre, and a flat bottom quartz vessel which was used to contain the photocatalysts and the reactants for CO_2 photoreduction. The quartz vessel was placed on an indented hard plastic base covered by a soft silicone septum. Such soft septum was used to prevent the quartz vessel from being damaged when the reactor was tightly locked. A magnetic stirrer bar was placed inside the reactor to keep the TiO_2 powders suspended in water during CO_2 photoreduction experiments.

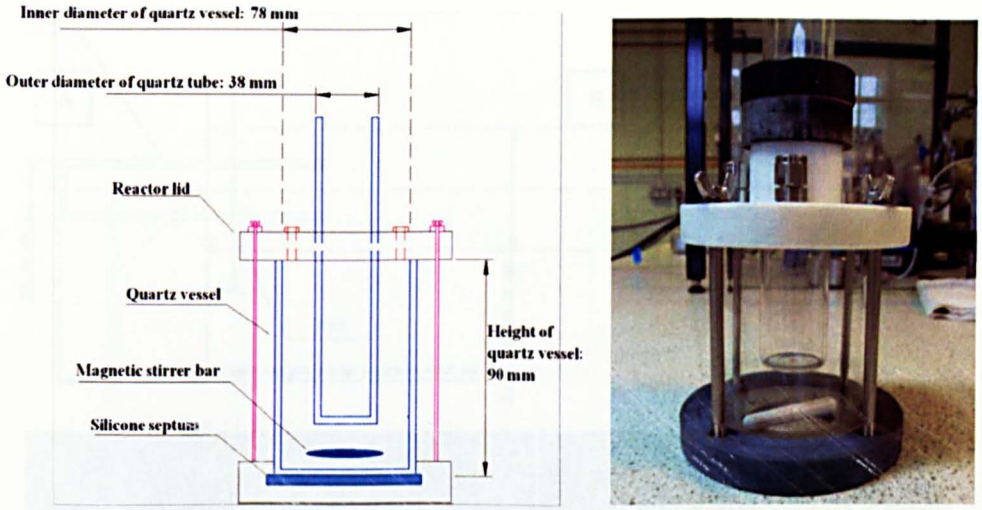

Fig. 3.2: Diagram (left) and actual picture (right) of the quartz photo-reactor.

Fig. 3.3 shows the horizontal and vertical views of the reactor lid. To guarantee that the reactor was inert to the chemicals and ultraviolet irradiation involved in the CO_2 photoreduction experiments, the primary body of the lid was made of Teflon, the O-ring and septum used to maintain the gas tightness were made of silicone, and the ports on the lid were made of stainless steel. There were four ports on the reactor lid (Fig 3.3 D), one was a gas inlet, one was a sampling port covered by a rubber septa to allow sampling by syringe during CO_2 photoreduction experiment, and the other two were for the connection of pressure gauge and thermometer. There was a quartz tube fixed on the centre of the lid that could be used to place an additional ultraviolet lamp in it and, if necessary, to place cooling water to control the temperature during experiments. This quartz tube could also be replaced by a sensor for dissolved oxygen.

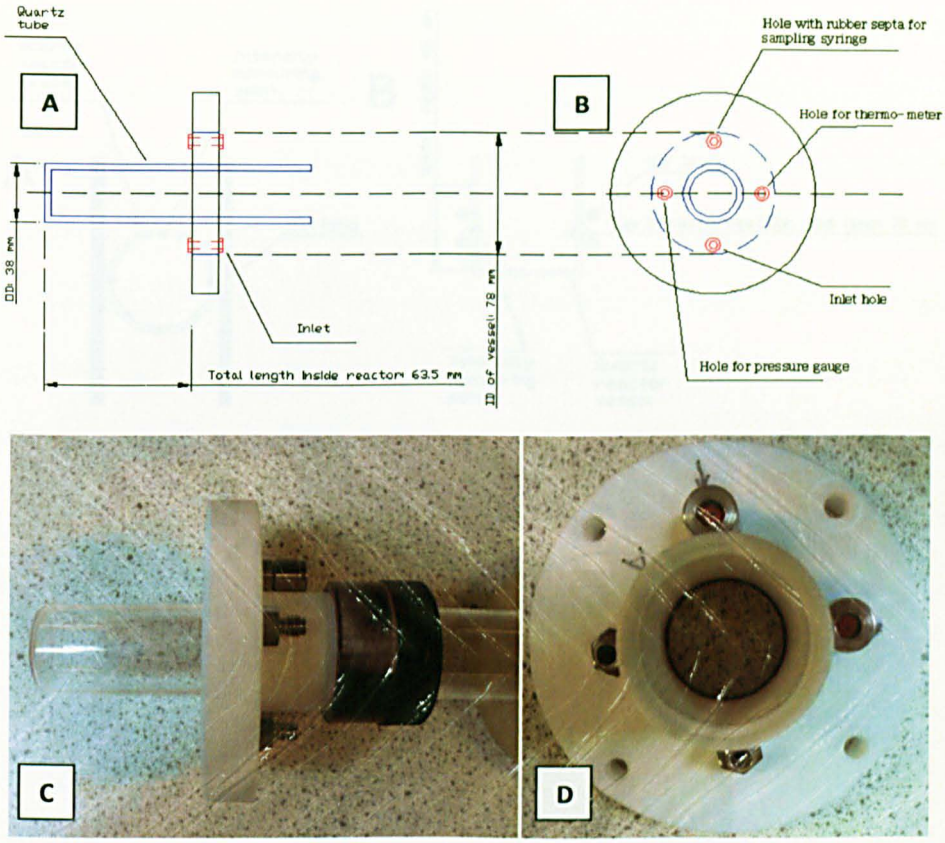

Fig. 3.3: Profiles and pictures of the reactor lid. A: Profile diagram of the lid, B: Cross-sectional diagram of the lid, C: Vertical view of the lid, D: Horizontal view of the lid.

As shown in Fig. 3.2, the flat bottom quartz vessel of the reactor, served as the container of catalysts and reactants, has a height of 90 mm and a diameter of 78 mm. The vessel was made of quartz to allow high transparency for the ultraviolet light. Four 8 watt ultraviolet lamps (T5 fluorescent blacklight blue, 8 watt, with primary wavelength at 365 nm) were equally located on two sides of the quartz vessel to provide the irradiation energy for the photocatalyst excitation during the CO_2 photo-reduction experiments (Fig. 3.4).

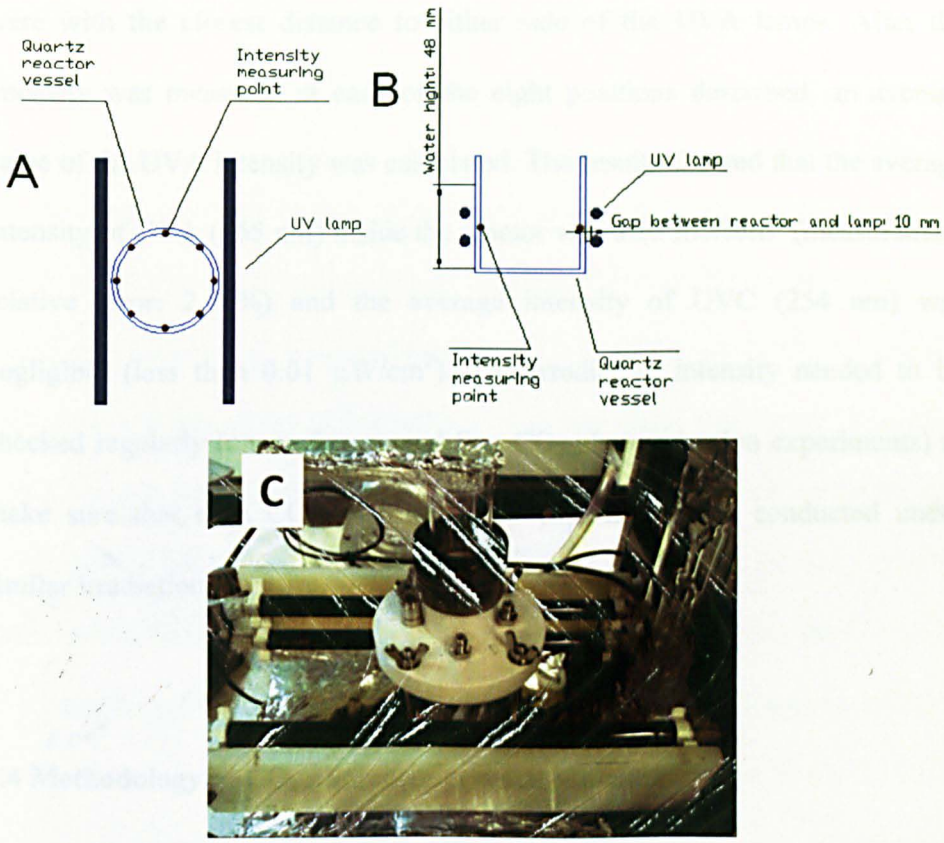

Fig. 3.4: Locations of the reactor vessel, UVA lamps and irradiation intensity measuring points. A: Cross-sectional diagram, B: Profile diagram, C: actual picture of reactor and UVA lamps.

Due to the fact that the irradiation intensity has a great effect on the photocatalysis process, it was important to measure the irradiation intensity inside the reactor before starting to run the CO_2 photoreduction experiments (Hoffmann et al., 1995). The measurements were conducted by using a UV meter equipped with UVA and UVC probes (UVP, UVX radiometer). Fig. 3.4 illustrates the points chosen to measure the irradiation intensity, wherein the irradiation intensity measurements were conducted at eight different positions inside the reactor vessel and each position clockwisely rotated 45 °C compared to the previous intensity measuring position. Two of the measuring positions

were with the closest distance to either side of the UVA lamps. After the intensity was measured at each of the eight positions described, an average value of the UVA intensity was calculated. The results showed that the average intensity of UVA (365 nm) inside the reactor was 3.25 mW/cm^2 (measurement relative error: 2.46%) and the average intensity of UVC (254 nm) was negligible (less than 0.01 $\mu W/cm^2$). The irradiation intensity needed to be checked regularly (once after around five CO_2 photoreduction experiments) to make sure that each CO_2 photoreduction experiment was conducted under similar irradiation intensity.

3.4 Methodology of CO_2 photoreduction experiment

The TiO_2 synthesized in this work were tested for CO_2 photoreduction. The experiments were conducted in the photo-reactor described in Section 3.3. The products (e.g. methane and methanol) of CO_2 photoreduction were measured by a gas chromatograph equipped with a flame ionization detector (GC/FID, Thermo-Fisher, Trace GC). This section introduces the procedure and conditions of CO_2 photoreduction experiment, and the methods to analyse methane and methanol by GC/FID.

3.4.1 Procedure and conditions of CO_2 photoreduction experiment

Fig. 3.5 represents the typical procedure of a CO_2 photoreduction experiment in this work. Firstly, 200 ml of deionized water and 1 g of TiO_2 powders were added into the reactor. A magnetic stirrer (at 120 RPM) was used to keep the TiO_2 powders suspended in the water during the entire experiment. The ultra pure CO_2 (Air Products, 99.995 %) was bubbled through the reactor for 20 min to remove the air inside the reactor. The absolute pressure of the regulator outlet of the CO_2 cylinder was maintained to be 1.4 atm during the bubbling. The dissolved oxygen (DO) concentration of the aqueous suspension was monitored by a sensor for dissolved oxygen (Mettler Toledo, SevenGo SG6-ELK). The DO concentration of the aqueous suspension was around 6.88 mg/L and decreased to be 0.00 mg/L after 20-min CO_2 bubbling. After the CO_2 purging, the reactor was pressurized with CO_2 up to the absolute pressure of 2 atm and held at this pressure for 15 min to ensure the saturation of CO_2 in the liquid phase inside the reactor. Afterwards the samples (from both the liquid and gas phases) in the reactor were taken by syringes from the sampling port of the reactor. These samples were injected into a GC/FID to confirm that there were no organic contaminants inside the reactor. It should be noted that the sampling and the injection of the gaseous samples were conducted by a gas-tight syringe (Hamilton, 1000-μl gas-lock syringe). Four UVA lamps equally located on the two sides of the reactor were then turned on to provide UVA irradiation (wavelength: 365 nm) to activate the TIO_2 and initiate the CO_2 photoreduction reaction inside the photo-reactor. The whole reactor and irradiation system were placed in a protective rig enclosed by black curtains to

avoid the harm of UV irradiation to the personnel in laboratory and the temperature and pressure in the reactor were monitored during the experiment. Typically after 1.5 hr, the UV lamps were turned off and the liquid and gaseous samples from the reactor were taken and injected into the GC/FID to measure the concentration of the organic products of the CO_2 photoreduction reaction. Methane and methanol were possible products produced by the reaction.

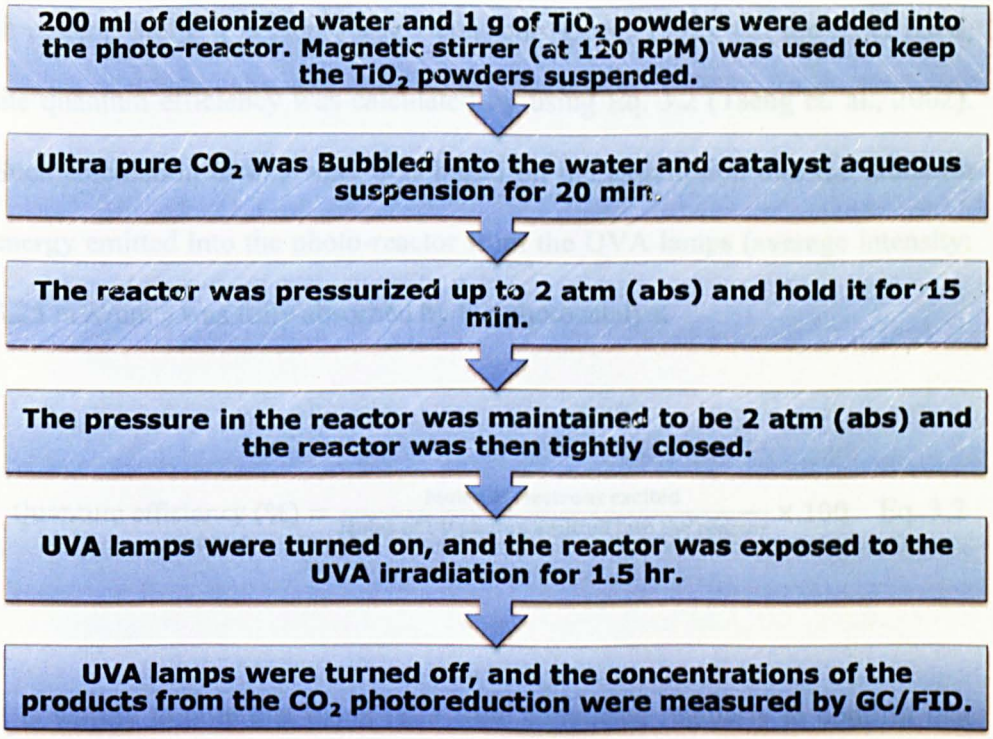

Fig. 3.5: Procedure of a typical CO_2 photoreduction experiment in this work.

After the CO_2 photoreduction experiment; the conversion of CO_2 during the reaction; the turnover number (TON), and quantum efficiency of the catalyst were calculated. For the calculation of conversion of CO_2, the amount of CO_2

dissolved in the water phase of the reactor was required to be known. The solubility of CO_2 was calculated via Henry's law, expressed as:

$$c = k^{o}_{H} \times p \qquad \text{Eq. 3.1}$$

where c is the concentration of CO_2 in water, p is the absolute pressure of CO_2 in reactor, and k^{o}_{H} is Henry's law constant (Dean, 1992). On the other hand, the quantum efficiency was calculated by using Eq. 3.2 (Tseng et. al., 2002). Such calculation in this work was based on the assumption that the radiation energy emitted into the photo-reactor from the UVA lamps (average intensity: 3.25 mW/cm^2) was fully absorbed by the photocatalyst.

$$\text{Quantum efficiency (\%)} = \frac{\text{Moles of electrons excited}}{\text{Moles of UV photon emitted into the reactor}} \times 100 \qquad \text{Eq. 3.2}$$

It is worthy to note that blank tests were conducted regularly to confirm that the organic products found after the experiments were indeed derived from CO_2 photoreduction, rather than from the decomposition of the organic contaminants. The first blank test used pure Helium instead of CO_2; the second one operated the reactor in a dark environment; and the final one omitted the photocatalyst. No products were observed in any of these blank tests.

3.4.2 GC/FID Analytical method

It has been reported that methane and methanol were the potential organic products from the CO_2 photoreduction (Inoue et al., 1979; Tseng et al., 2002; Kohno et al., 2001; Nguyen and Wu, 2008). Therefore, this work assessed the activity of TiO_2 for CO_2 photoreduction by measuring the productions of methane and methanol after the reaction. A GC/FID was used to for such purpose. This GC/FID equipped with two different columns for methane and methanol analysis, respectively. This section introduces the GC/FID analytical methods.

3.4.2.1 Methane analysis

The column used for methane analysis was a Molecular Sieve 5A (Restek). As described in Section 3.4.1, the gas samples were taken from the photo-reactor by a gas-tight sampling syringe. The volume of the sample for each injection was 400 μl. The temperature of the inlet and detector of GC/FID were 60 °C and 180 °C, respectively. The temperature of the GC oven was kept constant at 50 °C. The carrier gas through the column was helium at a flow rate of 20 ml/min. The analysis started once the sample was injected and the duration for each analysis was 2 min.

Figures 3.6 and 3.7 show the results of the GC/FID analysis for the methane standards (Trace methane in CO_2, with methane concentration ranged from 1 ppm to 15 ppm), and the corresponding methane calibration curve. It can be seen in Fig. 3.6 that clear methane peaks were obtained at the retention time of around 1.34 min, and the peak area increased as the methane concentration increased. It should be noted that the position of the methane peak shifted to slightly earlier retention time after the repetitious injections (around 20 times) of CO_2 and methane mixtures. This was because Molecular Sieve column was packed with porous zeolite material, which could adsorb both CO_2 and methane (Restek Corporation, 2007; Chang and Wu, 2009). As a large volume of CO_2 (compared to the amount of methane) was introduced in each injection, some of the CO_2 remained in the column occupying a fraction of the pore space of the packed material in the column and, therefore, accelerated the desorption of methane during the analysis. This resulted in earlier retention time of methane. In an attempt to minimize the shift of the retention time of methane, a method was developed and conducted regularly (once a day). The method consisted of increasing both the temperature of the GC oven (up to 180 °C) and flow rate of the carrier gas (up to 25 ml/min) for 20 min to remove the residual CO_2 in the column.

Fig. 3.7 further shows the methane calibration curve. It can be seen that such curve was linear. And it should be noted that the highest methane concentration presented in this curve (15 ppm) was higher than that of the methane measured in the experiments in this work (12.15 ppm). Therefore, the methane calibration curve was reliable.

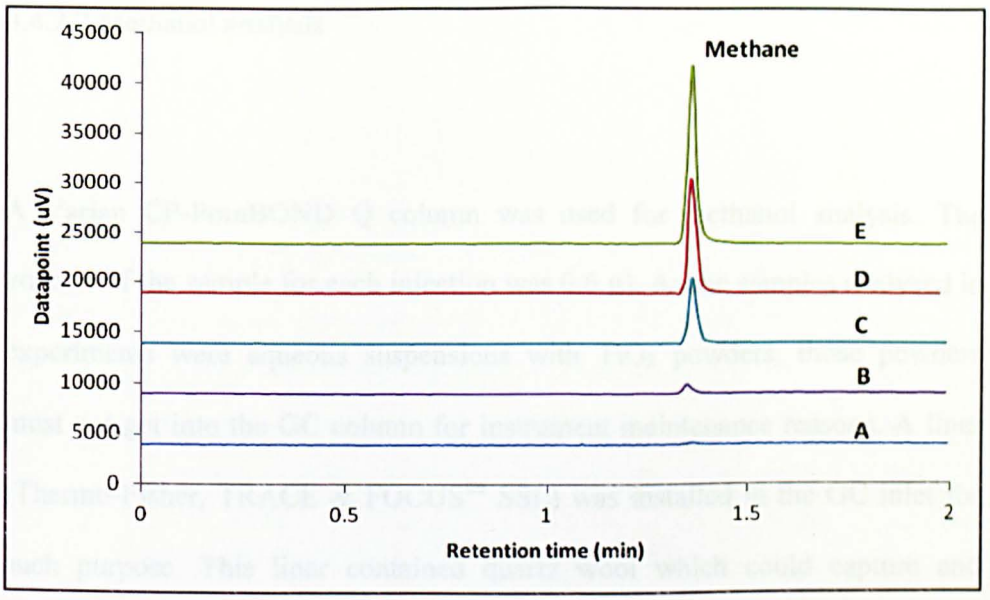

Fig. 3.6: GC/FID analysis for methane standards. A: pure CO_2, B: 1 ppm methane, C: 5 ppm methane, D: 10 ppm methane, E: 15 ppm methane.

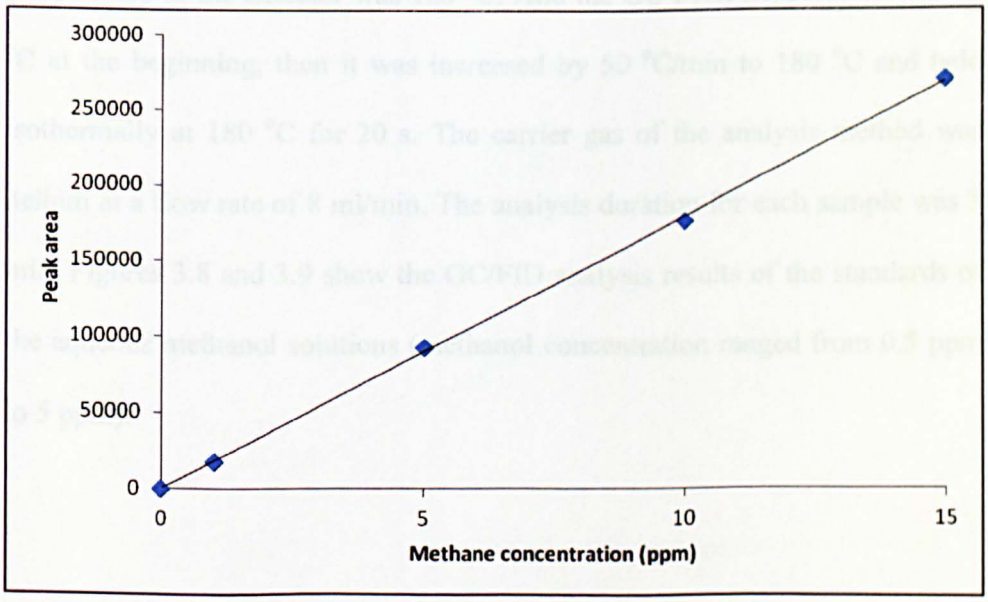

Fig. 3.7: Methane calibration curve.

3.4.2.2 Methanol analysis

A Varian CP-PoraBOND Q column was used for methanol analysis. The volume of the sample for each injection was 0.6 μl. As the samples analysed in experiments were aqueous suspensions with TiO_2 powders, those powders must not get into the GC column for instrument maintenance reasons. A liner (Thermo-Fisher, TRACE & FOCUS^{tm} SSL) was installed in the GC inlet for such purpose. This liner contained quartz wool which could capture and prevent the ungasifiable materials from getting into the GC column. In a typical methanol analysis process, the temperature of the GC inlet was 200 °C, which was able to gasify the liquid sample once it got into the inlet. The temperature of the detector was 180 °C. And the GC oven temperature was 45 °C at the beginning, then it was increased by 50 °C/min to 180 °C and held isothermally at 180 °C for 20 s. The carrier gas of the analysis method was helium at a flow rate of 8 ml/min. The analysis duration for each sample was 3 min. Figures 3.8 and 3.9 show the GC/FID analysis results of the standards of the aqueous methanol solutions (methanol concentration ranged from 0.5 ppm to 5 ppm).

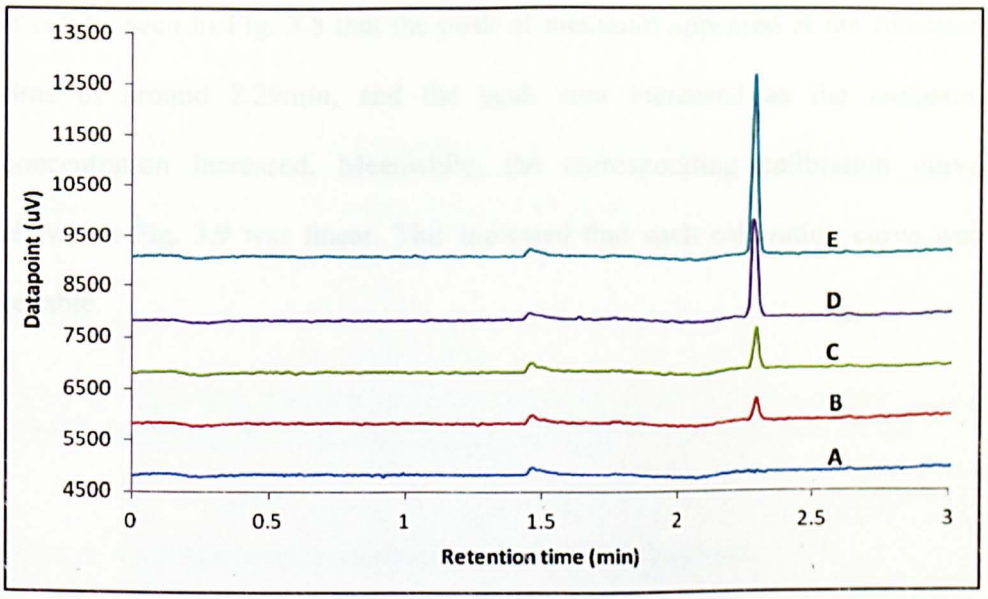

Fig. 3.8: GC/FID analysis for the standards of aqueous methanol solutions. A: pure deionized water, B: 0.5ppm methanol, C: 1 ppm methanol, D: 3 ppm methanol, E: 5 ppm methanol.

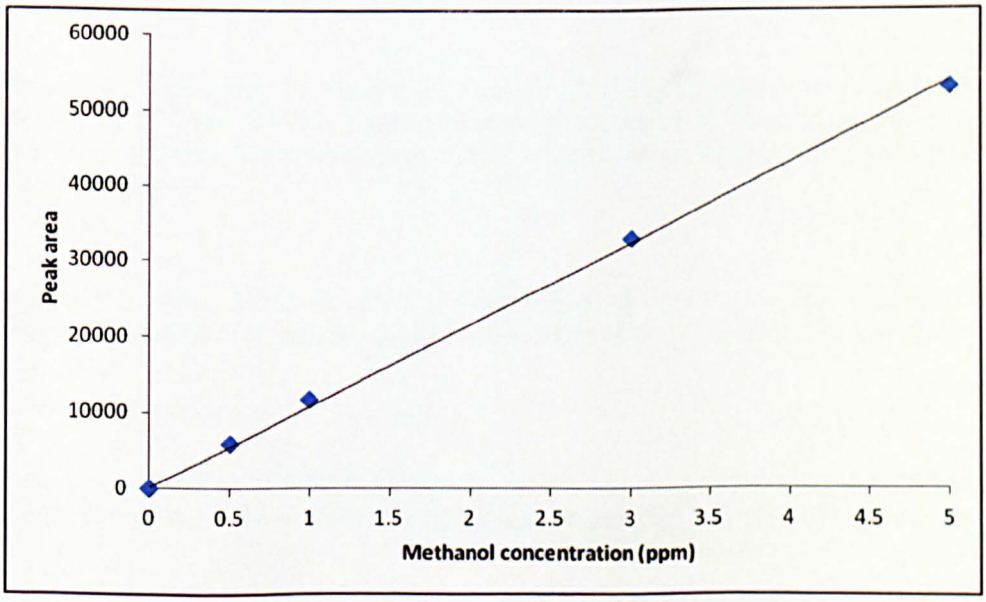

Fig. 3.9: Methanol calibration curve.

It can be seen in Fig. 3.8 that the peak of methanol appeared at the retention time of around 2.29min, and the peak area increased as the methanol concentration increased. Meanwhile, the corresponding calibration curve shown in Fig. 3.9 was linear. This indicated that such calibration curve was reliable.

References

Chang, H., Wu, Z. X. (2009). Experimental study on adsorption of carbon dioxide by 5A molecular sieve for helium purification of high-temperature gas-cooled reactor. *Industrial & Engineering Chemistry Research* **48**: 4466-4473.

DuPont. (2011). Determination of acid solubility of TiO_2. (Online). DuPont. Available at: <http://www2.dupont.com/Titanium_Technologies/en_US/tech_info/test_methods/CONCENTRATED_ACID_SOLUBILITY_OF_TiO2.pdf> (Accessed Nov. 2011).

Deam, J. A. (1992). *Lange's handbook of chemistry*. McGraw-Hill.

Hoffmann, M. R., Martin, S. T., Choi, W., Bahnemann, D. W. (1995). Environmental applications of semiconductor photocatalysis. *Chemical Reviews* **95**: 69-96.

Inoue, T., Fujishima, A., Konishi, S., Honda, K. (1979). Photoelectrocatalytic reduction of carbon dioxide in aqueous suspensions of semiconductor powders. *Nature* **277**: 637-638.

Kohno, Y., Yamamoto, T., Tanaka, T., Funabiki, T. (2001). Photoenhanced reduction of CO_2 by H_2 over Rh/TiO_2 characterization of supported Rh species by means of infrared and X-ray absorption spectroscopy. *Journal of Molecular Catalysis A* **175**: 173-178.

Nguyen, T., Wu, J. C. S. (2008). Photoreduction of CO_2 in an optical-fiber photoreactor: Effect of metals addition and catalyst carrier. *Applied Catalysis A* **335**: 112-120.

Restek Corporation. (2007). Molecular sieve 5A and 13X. (Online). Restek Corporation. Available at <http://www.restek.com/pdfs/59538A.pdf> (Accessed Dec. 2011).

Tseng, I., Chang, W., Wu, J. C. S. (2002). Photoreduction of CO_2 using sol-gel derived titania and titania-supported copper catalyst. *Applied Catalysis B* **37**: 37-48.

Wu, J. C. S., Yeh, C. Y. (2001). Sol-gel derived photosensitive TiO_2 and Cu/TiO_2 using homogeneous hydrolysis technique. *Journal of Materials Research* **16**: 2.

Wu, J. C. S., Tseng, I. H., Chang, W. C. (2001). Synthesis of titania-supported copper nanoparticles via refined alkoxide sol-gel process. *Journal of Nanoparticle Research* **3**: 113-118.

Chapter 4: Catalyst synthesis and characterization

As described in Chapter 2, titanium dioxide (TiO_2) was chosen to be the photocatalyst for CO_2 photoreduction in this work. Chapter 3 described the sol-gel process adopted in this work to synthesize the TiO_2 catalysts, including pure and metal modified TiO_2; which were referred as SG TiO_2 and M/TiO_2, respectively. Chapter 3 also reported that these TiO_2 catalysts were characterized by a series of analytical techniques. This chapter presents the data and the related discussions of the TiO_2 catalyst synthesis and characterization.

4.1 Catalyst synthesis

The TiO_2 catalysts of this work were synthesized via a refined sol-gel process developed by Wu et al. (Wu and Yeh, 2001; Wu et al., 2001). During the synthesis process, a few measurements were conducted in order to guarantee that the TiO_2 synthesis was successful. Such measurements included the monitoring of the pH value of the precursor solution to ensure the completion of hydrolysis, thermo-gravimetric analysis (TGA) after the calcination to confirm that all organic residues had been burned off, and the observation on the colours of the synthesized TiO_2 catalysts.

4.1.1 pH monitoring on precursor solution

As described in Section 3.1, the titanium precursor (titanium(IV) n-butoxide) was homogeneously mixed with n-butanol and acetic acid at the beginning of the sol-gel synthesis process. The esterification of the later two chemicals within such precursor solution then slowly released water to initiate the hydrolysis of the titanium precursor. To measure the necessary time for the completion of the hydrolysis, the pH value was monitored on a typical batch of the precursor solution (consisted of 0.02 mol titanium(IV) n-butoxide, 0.08 mol n-butanol, and 0.08 mol acetic acid). This is because the variation of the pH value could indicate whether the esterification of n-butanol and acetic acid was completed, indicating when the hydrolysis was completed. Wu and Yeh (2001), who used the same sol-gel process to synthesized TiO_2, also used the same method to identify the necessary time for the hydrolysis. They reported that the pH value of their precursor solution (also consisted of 0.02 mol titanium(IV) n-butoxide, 0.08 mol n-butanol, and 0.08 mol acetic acid) was stabilized at 3.56 after around 6 hr, which indicated the completion of hydrolysis.

Fig. 4.1 shows the pH variation of a typical batch of the sol-gel precursor solution. The conditions of such precursor solution were the same as the typical sol-gel process described in Section 3.1. It can be seen that the pH value of the precursor solution was initially as low as 2.45 because of the presence of acetic acid. Then the pH value gradually increased, indicating the consumption of the acetic acid via esterification (Wu and Yeh, 2001). Finally, after 5 hr, the pH

value was stabilized at 3.34 and did not significantly change in the next 5 hr. Such pH variation of the sol-gel precursor solution was similar to the one reported by Wu and Yeh (2001), indicating that the hydrolysis could be completed after 5 hr. Therefore, the stirring time of a typical batch of the precursor solution (6 hr, described in Section 3.1) during the sol-gel process in this work was sufficient for the completion of the hydrolysis.

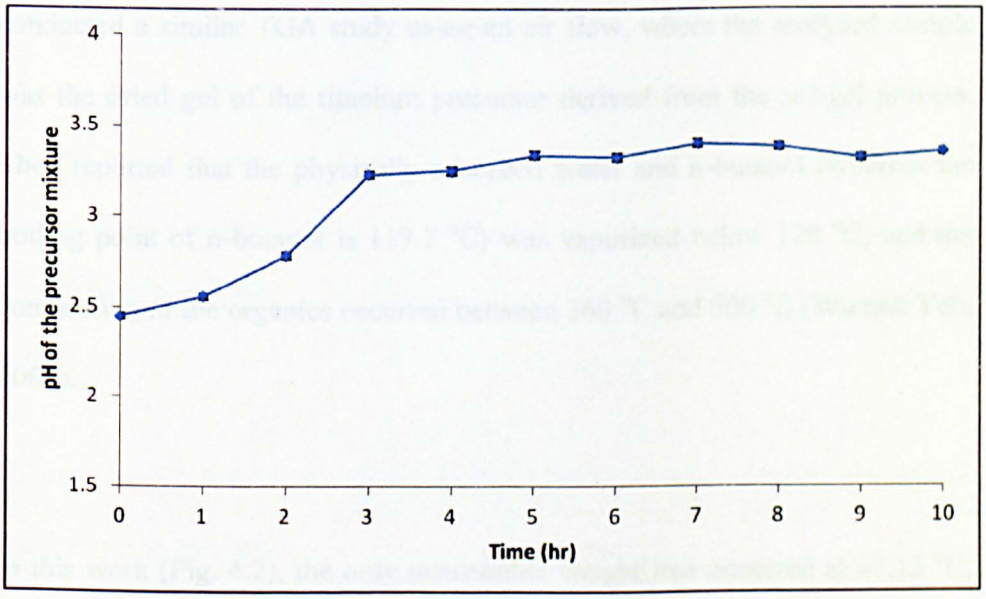

Fig. 4.1: pH variation of a typical batch of the sol-gel precursor solution.

4.1.2 TGA analysis on sol-gel synthesized TiO_2

TGA analysis within an air flow was conducted on a typical sol-gel synthesized TiO_2 (following the procedure described in Section 3.1). Such analysis was to confirm that the calcination in the sol-gel process of this work was sufficient to

burn off the organic residues derived from the precursors. Fig. 4.2 shows the TGA profile of a SG TiO_2 synthesized via a typical batch of the sol-gel process.

It can be seen from Fig. 4.2 that a weight loss appeared when the temperature exceed 47.15 °C, and no other distinguishable weight loss was observed during the rest of the analysis. The total weight loss of the analysed SG TiO_2 during the entire TGA analysis (up to 500 °C) was 1.07 %. Wu and Yeh (2001) conducted a similar TGA study using an air flow, where the analysed sample was the dried gel of the titanium precursor derived from the sol-gel process. They reported that the physically adsorbed water and n-butanol (wherein the boiling point of n-butanol is 117.7 °C) was vaporized below 120 °C, and the combustion of the organics occurred between 360 °C and 500 °C (Wu and Yeh, 2001).

In this work (Fig. 4.2), the only measurable weight loss occurred at 47.15 °C, which could be attributed to the physically adsorbed water, and no further weight loss was observed. Therefore, it can be concluded that the calcination in the typical sol-gel process of this work was sufficient to burn off all the organic residues derived from the precursors.

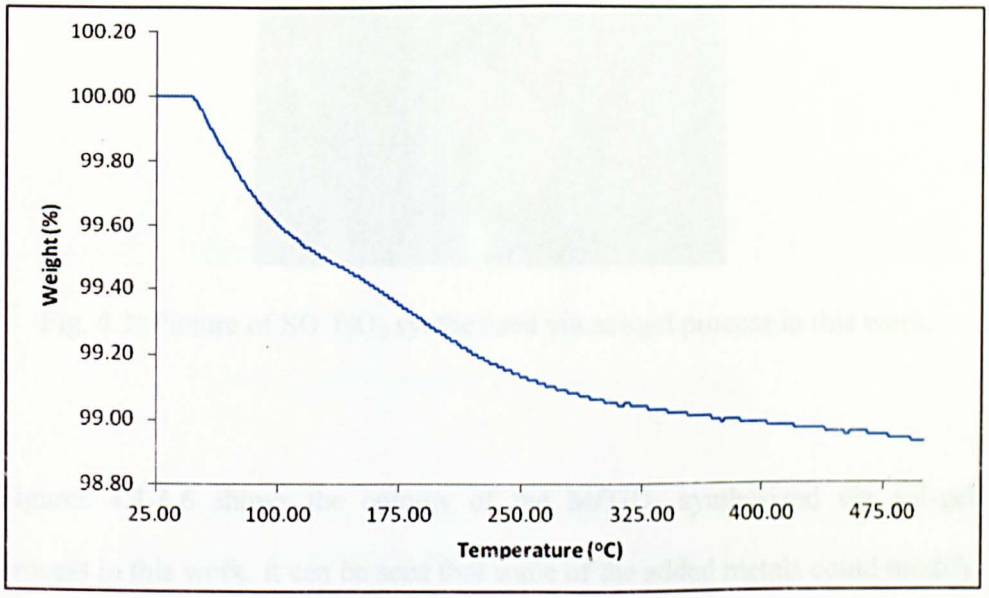

Fig 4.2: TGA analysis on a typical sol-gel synthesized SG TiO_2.

4.1.3 Catalyst colours

Figures 4.3-4.6 present the pictures of the TiO_2 catalysts synthesized via sol-gel process in this work.

The colour of the sol-gel synthesized SG TiO_2 is shown in Fig 4.3. It can be seen that such catalyst appeared to be white. This colour was consistent with the colour of the typical pure TiO_2 (DuPont, 2007). This can be an indication that highly pure TiO_2 was successfully synthesized via sol-gel process in this work.

Fig. 4.3: Picture of SG TiO_2 synthesized via sol-gel process in this work.

Figures 4.4-4.6 shows the colours of the M/TiO_2 synthesized via sol-gel process in this work. It can be seen that some of the added metals could modify the colour of TiO_2.

Fig. 4.4 shows the colour of Cu/TiO_2. It can be seen that those catalysts were yellow (colour became more intense as the Cu ratio increased), which was different from the colour of the Cu precursor. The Cu precursor used in the catalyst synthesis process in this work was copper(II) chloride dihydrate (Section 3.1). Such chemical appears to be blue, and becomes brown when it changes to the anhydrous form (Science Lab, 2010a; Fisher Scientific, 2004). However, the synthesized Cu/TiO_2 appeared neither of these colours. This is expected to be because the Cu precursor had been transformed during the sol-gel synthesis process into copper(I) oxide (Cu_2O) (proven by XRD and XPS, Sections 4.2.2.2 and 4.2.3.2), a chemical that could appear to be yellow (Iowa State University, 2001).

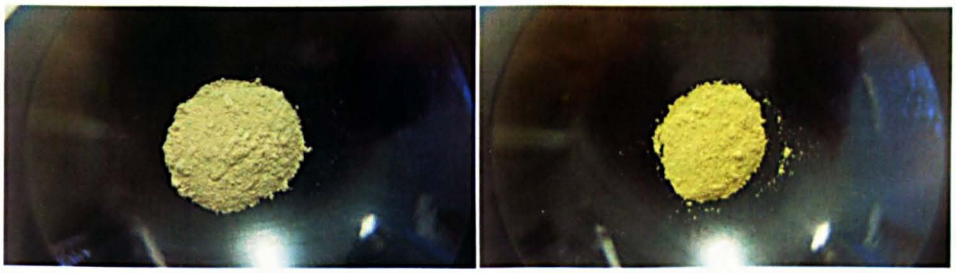

Fig. 4.4: Pictures of Cu/TiO_2 synthesized via sol-gel process in this work. 0.01 wt% Cu/TiO_2 (left), 0.5 wt% Cu/TiO_2 (right).

The pictures of Rh/TiO_2 catalysts are shown in Fig. 4.5. These catalysts appeared to be dark grey, wherein such colour became deeper as the Rh ratio increased. The Rh precursor was rhodium(II) acetate, and such chemical appears to be green (Fisher Scientific, 2009). However, the colour of Rh/TiO_2 was different from that of rhodium(II) acetate. This indicates that the Rh precursor was transformed during the sol-gel synthesis process. The results of XRD and XPS (Sections 4.2.2.3 and 4.2.3.3) further prove that the added Rh was doped into the lattice of Rh/TiO_2 with its chemical state to be Rh^{3+} in this work.

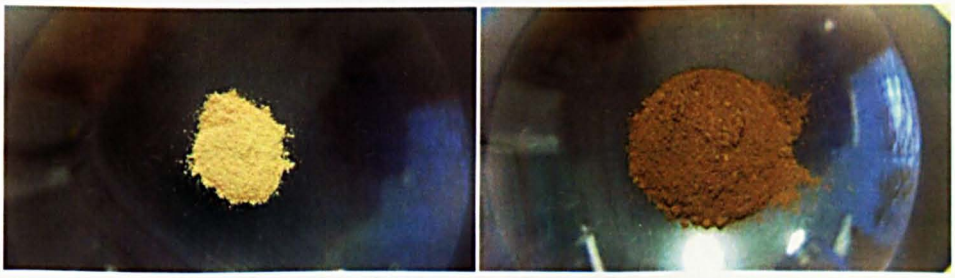

Fig. 4.5: Pictures of Rh/TiO_2 synthesized via sol-gel process in this work. 0.01 wt% Rh/TiO_2 (left), 0.5 wt% Rh/TiO_2 (right).

Fig. 4.6 shows that the presence of the added Zn did not change the colour of TiO_2 (white). The Zn precursor used in this study was zinc chloride that is known to be white (Science Lab, 2010b). Such chemical was transformed into zinc oxide (ZnO) which is also white (Science Lab, 2010c) and located on the surface of Zn/TiO_2 (proven by XRD and XPS, Sections 4.2.2.4 and 4.2.3.4) in this work. Therefore, the colour of the Zn/TiO_2 was the same as that of SG TiO_2.

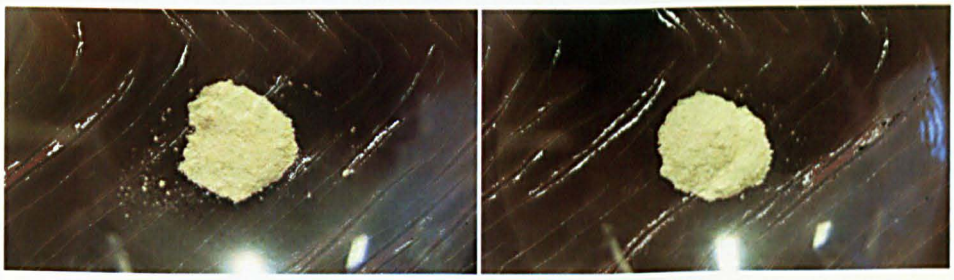

Fig. 4.6: Pictures of Zn/TiO_2 synthesized via sol-gel process in this work. 0.1 wt% Zn/TiO_2 (left), 0.5 wt% Zn/TiO_2 (right).

4.2 Catalyst characterization

The sol-gel synthesized TiO_2 catalysts were analysed by a series of analytical techniques, including inductively coupled plasma mass spectrometry, powder X-ray diffraction, transmission electron microscopy, photoelectron spectroscopy, N_2 adsorption isotherms, Cu surface area measurement, and diffuse reflectance ultraviolet-visible spectroscopy. This section presents the data obtained via these analytical techniques and the related discussions.

4.2.1 Inductively coupled plasma mass spectrometry (ICP-MS)

As described in Section 3.1, M/TiO_2 were synthesized via sol-gel process in this work. . Comparing to the previous studies that only reported the nominal elemental ratios of their metal modified TiO_2 catalysts (e.g. Wu and Yeh, 2001; Wu et al., 2001; Tseng et al., 2002 and 2004), this work confirmed the actual elemental ratios of M/TiO_2 ($\frac{\text{Mass of metal}}{\text{Mass of } TiO_2} \times 100$) by using ICP-MS.

The method to prepare the samples for the ICP-MS analysis was presented in Section 3.2.3. Tables 4.1-4.3 show the results of this analysis. The standard error of ICP-MS analysis is within 1 %. It should be noted that some of the M/TiO_2 catalysts were prepared in triplicates and each catalyst was then tested by ICP-MS in order to assess the errors of the elemental ratios of these catalysts. These catalysts included 0.03 wt% Cu/TiO_2, 0.006 wt% Rh/TiO_2, 0.1 wt% Zn/TiO_2 and 0.006 wt% Rh/0.03 wt% Cu/TiO_2. The errors of the elemental ratios of these catalysts are presented in the footnotes of Tables 4.1-4.3.

It can be seen in Tables 4.1-4.3 that the actual elemental ratios of the M/TiO_2 measured by ICP-MS generally matched their nominal elemental ratios. Moreover, the low error values of the triplicate tests indicate that the elemental ratios of M/TiO_2 were reliable. Therefore, this ICP-MS analysis confirmed that

M/TiO_2 with desired ratios of metals were successfully synthesized via sol-gel process in this work.

Table 4.1: Elemental ratios of Cu/TiO_2 measured by ICP-MS.

Nominal elemental ratio	Elemental ratio (ICP-MS)
2 wt% Cu/TiO_2	1.7641 wt% Cu/TiO_2
1 wt% Cu/TiO_2	0.8123 wt% Cu/TiO_2
0.5 wt% Cu/TiO_2	0.4644 wt% Cu/TiO_2
0.1 wt% Cu/TiO_2	0.0973 wt% Cu/TiO_2
0.07 wt% Cu/TiO_2	0.0721 wt% Cu/TiO_2
0.05 wt% Cu/TiO_2	0.0483 wt% Cu/TiO_2
0.04 wt% Cu/TiO_2	0.0417 wt% Cu/TiO_2
0.03 wt% Cu/TiO_2	0.0316 wt% Cu/TiO_2
0.02 wt% Cu/TiO_2	0.0214 wt% Cu/TiO_2
0.01 wt% Cu/TiO_2	0.0139 wt% Cu/TiO_2

Error of the elemental ratio of 0.03 wt% Cu/TiO_2 was 1.48 %.

Table 4.2: Elemental ratios of Rh/TiO_2 and Zn/TiO_2 measured by ICP-MS.

Nominal elemental ratio	Elemental ratio (ICP-MS)
0.5 wt% Rh/TiO_2	0.4892 wt% Rh/TiO_2
0.1 wt% Rh/TiO_2	0.0947 wt% Rh/TiO_2
0.03 wt% Rh/TiO_2	0.0297 wt% Rh/TiO_2
0.02 wt% Rh/TiO_2	0.0202 wt% Rh/TiO_2
0.01 wt% Rh/TiO_2	0.0101 wt% Rh/TiO_2
0.006 wt% Rh/TiO_2	0.0059 wt% Rh/TiO_2
0.003 wt% Rh/TiO_2	0.0031 wt% Rh/TiO_2
0.5 wt% Zn/TiO_2	0.4256 wt% Zn/TiO_2
0.1 wt% Zn/TiO_2	0.0927 wt% Zn/TiO_2

The errors of the elemental ratios of 0.006 wt% Rh/TiO_2 and 0.1 wt% Zn/TiO_2 were 0.79 % and 2.46 %, respectively.

Table 4.3: Elemental ratios of Rh/Cu/TiO_2 measured by ICP-MS.

Nominal elemental ratio	Elemental ratio (ICP-MS)
0.02 wt% Rh/0.03 wt% Cu/TiO_2	0.0197 wt% Rh/0.0309 wt% Cu/TiO_2
0.01 wt% Rh/0.03wt% Cu/TiO_2	0.0100 wt% Rh/0.0315 wt% Cu/TiO_2
0.006 wt% Rh/0.03wt% Cu/TiO_2	0.0059 wt% Rh/0.0297 wt% Cu/TiO_2
0.003 wt% Rh/0.03 wt% Cu/TiO_2	0.0030 wt% Rh/0.0321 wt% Cu/TiO_2

The errors of the Cu and Rh ratios of 0.03 wt% Cu/0.006 wt% Rh/TiO_2 were 1.63 % and 0.62 %, respectively.

4.2.2 Powder X-ray diffraction (powder XRD)

The crystalline structures of the TiO_2 catalysts synthesized via the sol-gel process were analysed by using powder XRD. Such analysis was conducted not only to determine the crystalline phases of these TiO_2 catalysts (anatase or rutile), but also to identify if the added metals were doped or loaded to their TiO_2 supports. An anatase reference (Acros Organics, 99%) was identically scanned for three times to assess the precision of this powder XRD analysis. The result indicates that the errors of such analysis (peak position and FWHM) were 0.34 % and 0.37 %, respectively.

4.2.2.1 Diffraction patterns of SG TiO_2 and anatase reference

A high purity anatase (Acros Organics, 99 %) was used as the anatase reference in the powder XRD analysis. Fig. 4.7 shows the diffraction patterns of the anatase reference and SG TiO_2. It can be seen from Fig. 4.7 that all the

peaks in the diffraction pattern of SG TiO_2 fully matched those of the anatase reference. This indicates that SG TiO_2 was in the crystalline phase of anatase.

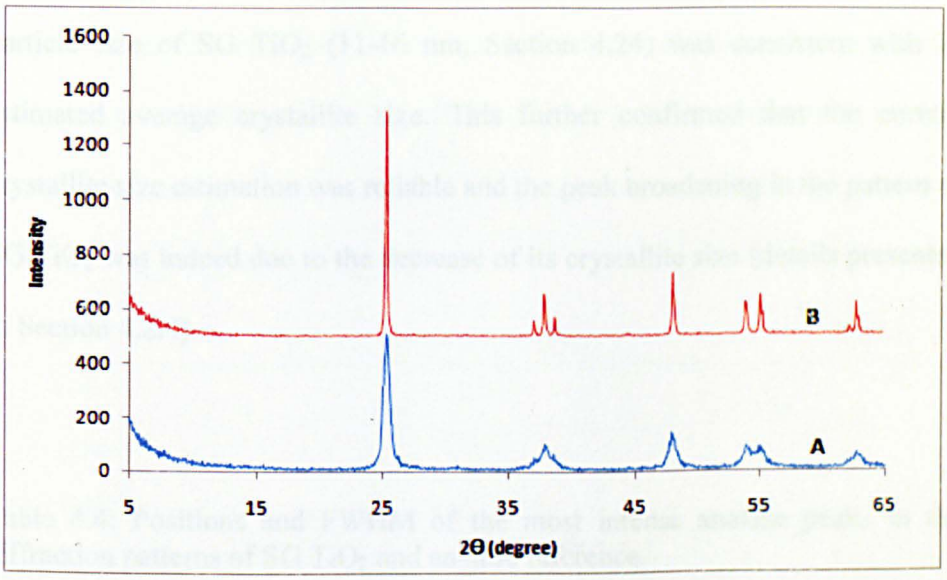

Fig. 4.7: Diffraction patterns of the pure TiO_2 samples. A: SG TiO_2, B: anatase reference.

Table 4.4 further shows the positions and full width at half maximum (FWHM) of the most intense anatase peaks within the diffraction patterns of SG TiO_2 and anatase reference. It is shown that the peak position of SG TiO_2 was consistent with that of the anatase reference. Meanwhile, the peak width of SG TiO_2 was broader than that of the anatase reference. As introduced in Section 2.4.1, the peak broadening appeared in the diffraction pattern can be attributed to the decrease of the crystallite size (basing on Scherrer Formula; Jenkins and Snyder, 1996); or the non-uniform change of the lattice spacing (normally accompanied with the peak shift; Waseda et al., 2011). Since only peak broadening occurred (no peak shift), it can be expected that such peak

broadening was primarily due to the smaller crystallite size of SG TiO_2 compared to that of the anatase reference. The average crystallite sizes of SG TiO_2 and anatase reference were estimated, via Scherrer Formula, to be 13.29 nm and 44.77 nm, respectively. The later TEM analysis confirmed that the particle size of SG TiO_2 (11-16 nm, Section 4.24) was consistent with its estimated average crystallite size. This further confirmed that the current crystallite size estimation was reliable and the peak broadening in the pattern of SG TiO_2 was indeed due to the decrease of its crystallite size (details presented in Section 4.2.4).

Table 4.4: Positions and FWHM of the most intense anatase peaks in the diffraction patterns of SG TiO_2 and anatase reference.

Sample	Peak position (degree)	FWHM (degree)
SG TiO_2	25.31	0.64
Anatase reference	25.31	0.19

4.2.2.2 Diffraction patterns of Cu/TiO_2

The diffraction patterns of Cu/TiO_2 are shown in Fig. 4.8. It can be seen that all the patterns of Cu/TiO_2, regardless the Cu ratio, involved the peaks that fully matched the peaks of SG TiO_2. Since it has been proven in Section 4.2.2.1 that SG TiO_2 was in the crystalline phase of anatase, it can be also concluded that the TiO_2 supports of Cu/TiO_2 were all in the crystalline phase of anatase. Meanwhile, the peak of the added Cu was absent, until the Cu ratio increased up to 10 wt%. The peak of the added Cu appeared at the position of 35.6

degree, which was attributed to Cu_2O (Huang et al., 2009). Previous studies (Sakthivel et. al., 2004; Madikizela-Mnqanqeni and Coville, 2008) normally attributed such poor detection of the added Cu via powder XRD directly to the uniform dispersion of the added Cu on TiO_2. Whereas, the author considered that it was necessary to conduct more detailed investigation on the specific surface area and dispersion of the added Cu of Cu/TiO_2. The results of such investigation are presented in Section 4.2.5.

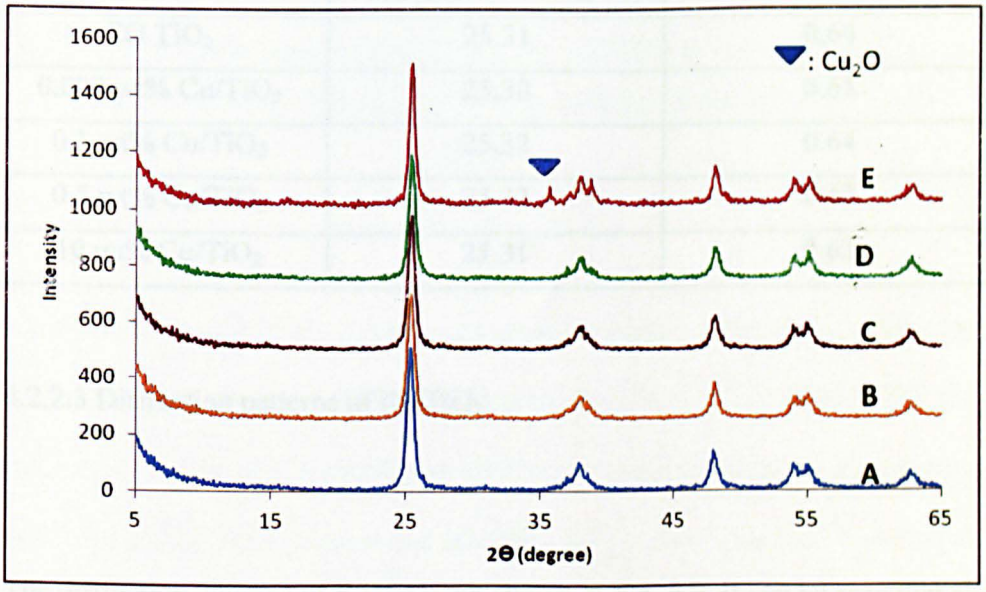

Fig. 4.8: Diffraction patterns of Cu/TiO_2. A: SG TiO_2, B: 0.003 wt% Cu/TiO_2, C: 0.1 wt% Cu/TiO_2, D: 0.5 wt% Cu/TiO_2, E: 10 wt% Cu/TiO_2.

Table 4.5 further presents the positions and FWHM of the most intense anatase peaks in the diffraction patterns of Cu/TiO_2. It can be seen that the presence of the added Cu did not cause any significant peak shift in the diffraction patterns of Cu/TiO_2, even when the Cu ratio increased up to 10 wt%. This indicates that the added Cu did not change the lattice spacing of TiO_2, which means that the

added Cu was loaded to TiO_2 other than doped into the lattice of TiO_2 (as introduced in Section 2.4.1; Huang et al., 2009). Meanwhile, the peak width of Cu/TiO_2 was similar to that of SG TiO_2. This means that Cu/TiO_2 had similar average crystallite sizes (13.09-13.72 nm) as that of SG TiO_2 (13.29 nm) (estimated via Scherrer Formula; Jenkins and Snyder, 1996).

Table 4.5: Positions and FWHM of the most intense anatase peaks in the diffraction patterns of Cu/TiO_2.

Catalyst	Peak position (degree)	FWHM (degree)
SG TiO_2	25.31	0.64
0.003 wt% Cu/TiO_2	25.30	0.65
0.1 wt% Cu/TiO_2	25.32	0.64
0.5 wt% Cu/TiO_2	25.32	0.62
10 wt% Cu/TiO_2	25.31	0.63

4.2.2.3 Diffraction patterns of Rh/TiO_2

The diffraction patterns of Rh/TiO_2 are shown in Fig. 4.9. It can be seen that all the peaks within these patterns, regardless the Rh ratio, fully matched the peaks of SG TiO_2. This indicates that the TiO_2 supports of Rh/TiO_2 were all at the crystalline phases of anatase.

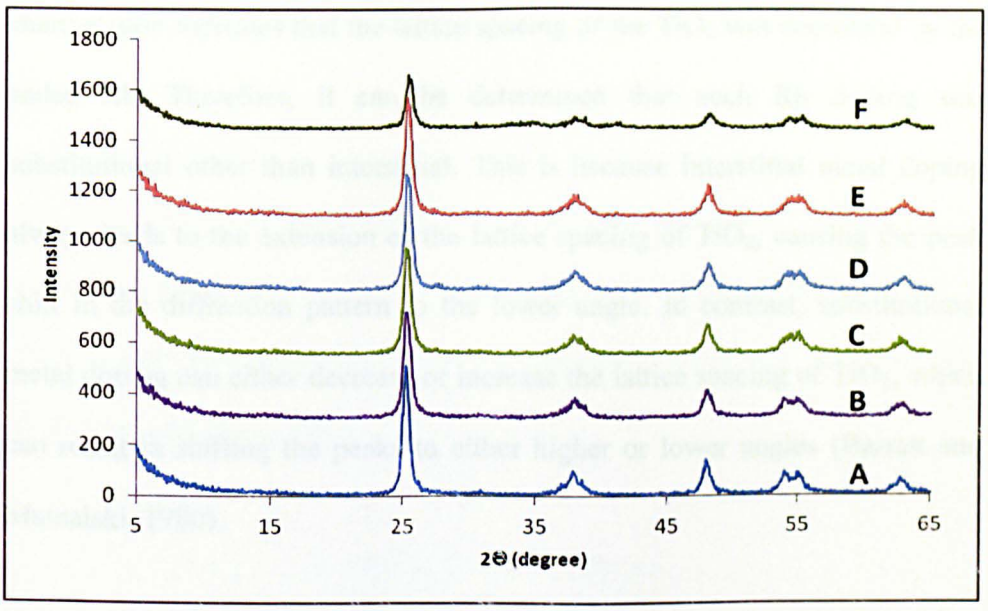

Fig. 4.9: Diffraction patterns of Rh/TiO_2. A: SG TiO_2, B: 0.01 wt% Rh/TiO_2, C: 0.03 wt% Rh/TiO_2, D: 0.1 wt% Rh/TiO_2, E: 0.5 wt% Rh/TiO_2, F: 5 wt% Rh/TiO_2.

The positions and FWHM of the most intense anatase peaks in the diffraction patterns of Rh/TiO_2 are further presented in Table 4.6. It can be seen that the presence of the added Rh simultaneously caused the peak broadening and peak shift in the diffraction patterns of Rh/TiO_2. There was a positive correlation between the extent of the peak shift and Rh ratio. The peak shift was slightly but genuinely enhanced when the Rh ratio increased within 0.01-0.5 wt%, and it became very obvious when the Rh ratio increased up to 5 wt% (Fig. 4.9). This is an indication that the added Rh was doped into the lattice of its TiO_2 support and non-uniformly changed the lattice spacing of TiO_2 (as introduced in Section 2.4.1; Waseda et al., 2011; Xin et al., 2005). It should be noted that the anatase peaks of Rh/TiO_2 were shifted to higher diffraction angle. Based on Bragg's law (presented in Section 2.4.1; Pecharsky and Zavalij, 2009), such

phenomenon indicates that the lattice spacing of the TiO_2 was decreased by the added Rh. Therefore, it can be determined that such Rh doping was substitutional other than interstitial. This is because interstitial metal doping always leads to the extension of the lattice spacing of TiO_2, causing the peak shift in the diffraction pattern to the lower angle. In contrast, substitutional metal doping can either decrease or increase the lattice spacing of TiO_2, which can result in shifting the peaks to either higher or lower angles (Barrett and Massalski, 1980).

Table 4.6: Positions and FWHM of the most intense anatase peaks in the diffraction patterns of Rh/TiO_2.

Catalyst	Peak position (degree)	FWHM (degree)
SG TiO_2	25.31	0.64
0.01 wt% Rh/TiO_2	25.33	0.64
0.03 wt% Rh/TiO_2	25.33	0.65
0.1 wt% Rh/TiO_2	25.35	0.66
0.5 wt% Rh/TiO_2	25.36	0.66
5 wt% Rh/TiO_2	25.56	0.68

Because the peak broadening in the diffraction patterns of Rh/TiO_2 was accompanied with peak shift, such peak broadening can be due to the non-uniform change of the lattice spacing of TiO_2, rather than the decrease of crystallite size (as introduced in Section 2.4.1; Waseda et al., 2011). Therefore, it is not applicable to use Scherrer Formula to estimate the average crystallite sizes of Rh/TiO_2 in this case, and the particle sizes of Rh/TiO_2 were solely assessed by TEM (results presented in Section 4.2.4).

4.2.2.4 Diffraction patterns of Zn/TiO_2

The diffraction patterns of Zn/TiO_2 are shown in Fig. 4.10. It can be seen that all the peaks in the patterns of Zn/TiO_2 fully matched the peaks of SG TiO_2. This phenomenon indicates that the TiO_2 supports of Zn/TiO_2 were all in the crystalline phase of anatase.

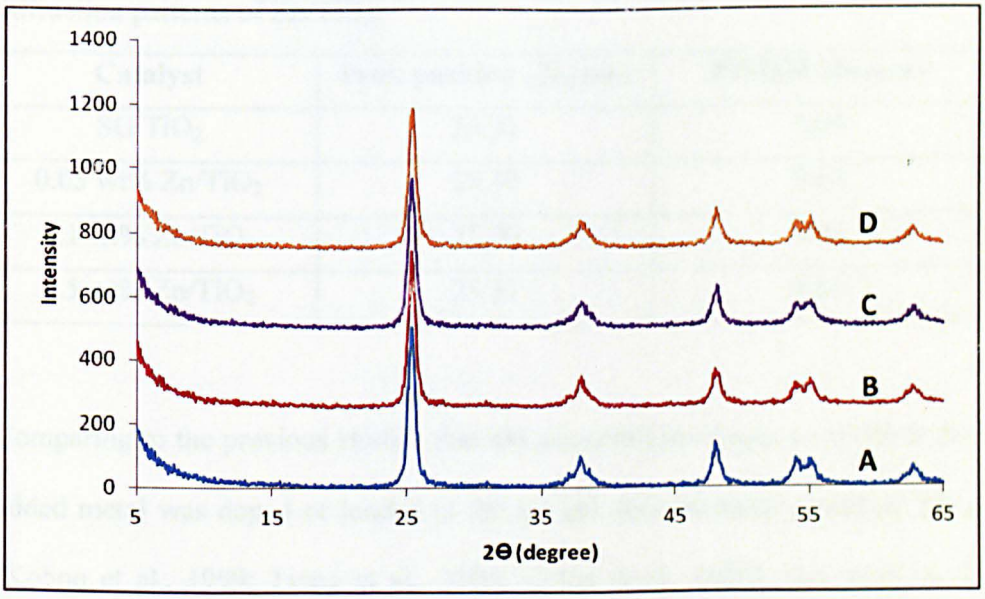

Fig. 4.10: Diffraction patterns of Zn/TiO_2. A: SG TiO_2, B: 0.05 wt% Zn/TiO_2, C: 0.1 wt% Zn/TiO_2, D: 0.5 wt% Zn/TiO_2.

Meanwhile, the parameters shown in Table 4.7 present that the presence of Zn did not lead to any significant peak shift or peak broadening in the diffraction patterns of Zn/TiO_2. This indicates that the added Zn did not change the lattice spacing of TiO_2; which means that the added Zn was loaded, other than doped, to its TiO_2 support. On the other hand, Fig. 4.10 shows that no peaks attributed

to the added Zn could be found in the diffraction patterns of Zn/TiO_2. This is because the Zn ratios of these analysed catalysts were not higher enough (only up to 0.5 wt%) to generate sufficiently aggregated Zn on TiO_2 to be detectable via XRD (as introduced in Section 2.3.1.3.1). Furthermore, the similar peak width of Zn/TiO_2 as that of SG TiO_2 indicates that Zn/TiO_2 had similar average crystallite sizes (13.09-13.50 mn) as that of SG TiO_2 (13.29 nm).

Table 4.7: Positions and FWHM of the most intense anatase peaks in the diffraction patterns of Zn/TiO_2.

Catalyst	Peak position (degree)	FWHM (degree)
SG TiO_2	25.31	0.64
0.05 wt% Zn/TiO_2	25.30	0.63
0.1 wt% Zn/TiO_2	25.30	0.64
0.5 wt% Zn/TiO_2	25.31	0.64

Comparing to the previous studies that did not conclusively prove whether the added metal was doped or loaded to the sol-gel derived metal modified TiO_2 (Kohno et al., 1999; Tseng et al., 2004; Colon et al., 2006), this work used powder XRD to clarify such question. It is interesting to highlight that, although synthesized via the same sol-gel process, the added metals modified their TiO_2 supports differently. Both Cu and Zn were loaded to TiO_2, whereas Rh was substitutionally doped to TiO_2. This is expected to be due to the different ionic sizes of these added metals. As proven in the next section by XPS (Section 4.2.3), the chemical states of the added metals were Cu^{1+}, Zn^{2+}, and Rh^{3+}, respectively, and their ionic radii are 91 pm, 88 pm, and 80.5 pm, respectively (Shannon, 1976). Meanwhile, the percent differences between

these added metal ions (Cu^{1+}, Zn^{2+}, Rh^{3+}) and Ti^{4+} ion (ionic radius: 74.5 pm; Shannon, 1976) are 19.94 %, 16.62 %, and 7.74 %, respectively. As introduced in Section 2.3.1.2, substitutional metal doping to TiO_2 is likely only when the sizes of the added metal ion and Ti^{4+} differ by no more than 15 % (Barrett and Massalski, 1980; Li et al., 2005). Therefore, among the three added metals in this work, Rh in the chemical state of Rh^{3+} was the only one presenting a suitable ionic radius for substitutional doping to TiO_2.

4.2.3 X-ray photoelectron spectroscopy (XPS)

XPS was used to determine the chemical states of the added metals of M/TiO_2 and their elemental ratios on the surfaces of M/TiO_2. Because it had been well proven that the peak of O 1s of anatase should appear at the binding energy of 530.0 eV in a XPS analysis (as introduced in Section 2.4.2; Rensmo et al., 1997), the XPS analysis in this work used such value for the charge correction. The ratios of the added metals of the samples analysed by XPS were all not lower than 0.5 wt%. This is to ensure that the amounts of the added metals of the analysed samples were above the detection limit of the XPS instrument used in this work.

4.2.3.1 Spectrum of SG TiO_2

Fig. 4.11 shows the XPS spectrum of Ti 2p of SG TiO_2. It can be seen that the peak of Ti $2p_{3/2}$ appeared at the binding energy of 458.76 eV, and this was consistent with the binding energy of the Ti $2p_{3/2}$ of anatase of458.8 eV (Prokes et al., 2005). Such result further confirmed the conclusion obtained via XRD analysis (Section 4.2.2.1) that SG TiO_2 was in the crystalline phase of anatase.

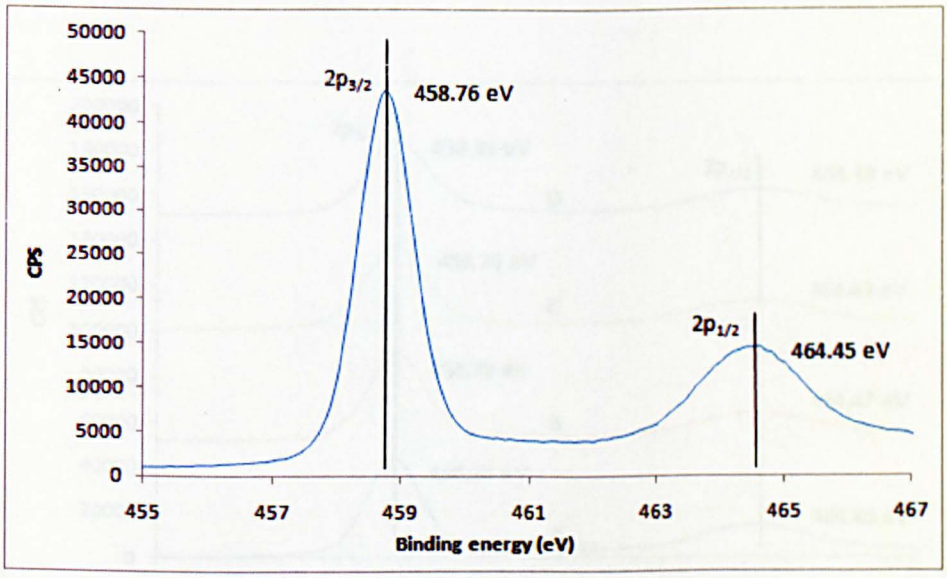

Fig. 4.11: XPS spectrum of Ti 2p of SG TiO_2.

4.2.3.2 Spectra of Cu/TiO_2

Figures 4.12 and 4.13 present the XPS spectra of Ti 2p and Cu 2p of Cu/TiO_2. It can be seen in Fig. 4.12 that the peaks of Ti $2p_{3/2}$ of the analysed Cu/TiO_2 appeared at the position of the binding energies of 458.76-458.81 eV, which were all similar to the binding energy of Ti $2p_{3/2}$ of SG TiO_2. This indicates that the TiO_2 supports of these Cu/TiO_2 were all in the crystalline phase of anatase regardless the Cu ratio. This confirmed the result of powder XRD regarding the crystalline phase of Cu/TiO_2 (Section 4.2.2.2).

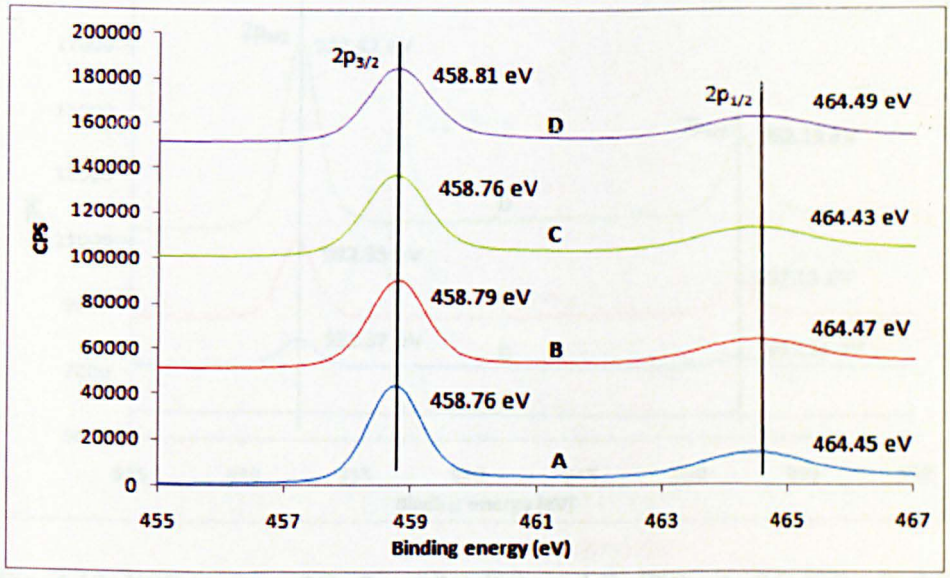

Fig. 4.12: XPS spectra of Ti 2p of SG TiO_2 and Cu/TiO_2. A: SG TiO_2, B: 0.5 wt% Cu/TiO_2, C: 1 wt% Cu/TiO_2, D: 2 wt% Cu/TiO_2.

Fig. 4.13 shows the spectra of Cu 2p of Cu/TiO_2. It can be seen that the peaks of Cu $2p_{3/2}$ appeared at the binding energies of 932.35-932.42 eV. Gan et al.

(2004) reported that the binding energy of Cu $2p_{3/2}$ of Cu_2O was around 932.4 eV, and it has been proven by power XRD that the added Cu of Cu/TiO_2 were loaded to their TiO_2 supports (Section 4.2.2.2). Therefore, it can be concluded that the added Cu of these analysed 0.5-2 wt% Cu/TiO_2 were all loaded to their TiO_2 supports in the chemical state of Cu_2O. Furthermore, because the chemical states of the added Cu of the XPS-analysed Cu/TiO_2 did not change with the Cu ratio, it is expected that the chemical states of the added Cu of the other Cu/TiO_2 synthesized in this work (e.g. 0.01-0.1 wt% Cu/TiO_2) were also Cu_2O.

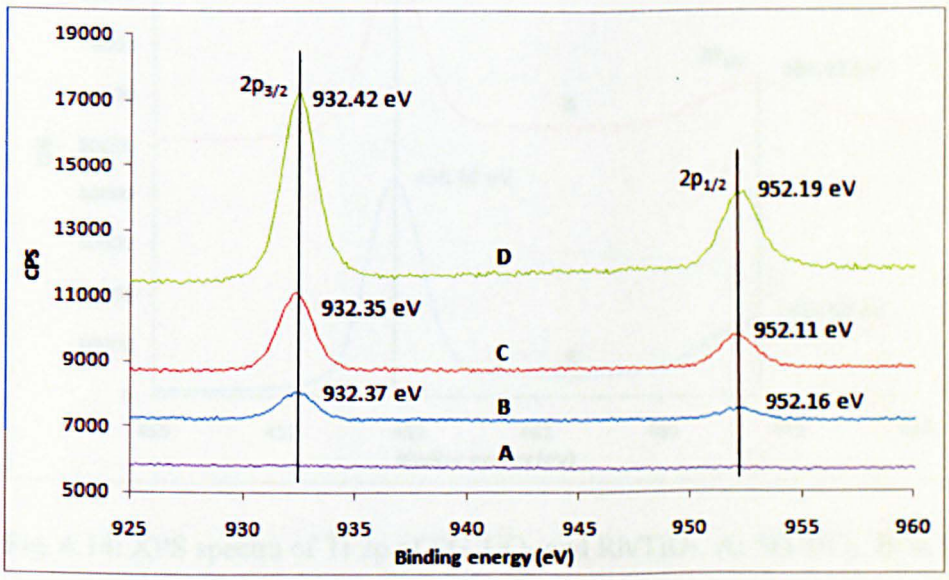

Fig. 4.13: XPS spectra of Cu 2p of SG TiO_2 and Cu/TiO_2. A: SG TiO_2, B: 0.5 wt% Cu/TiO_2, C: 1 wt% Cu/TiO_2, D: 2 wt% Cu/TiO_2.

4.2.3.3 Spectra of Rh/TiO_2

Figures 4.14 and 4.15 present the XPS spectra of Rh/TiO_2. Fig. 4.14 shows the spectrum of Ti 2p of 0.5 wt% Rh/TiO_2, wherein the peak of Ti $2p_{3/2}$ of 0.5 wt% Rh/TiO_2 was at 458.75 eV. Such value was similar to that of SG TiO_2 and further confirms that the crystalline phase of the TiO_2 supports of Rh/TiO_2 was anatase (as proven by powder XRD in Section 4.2.2.3).

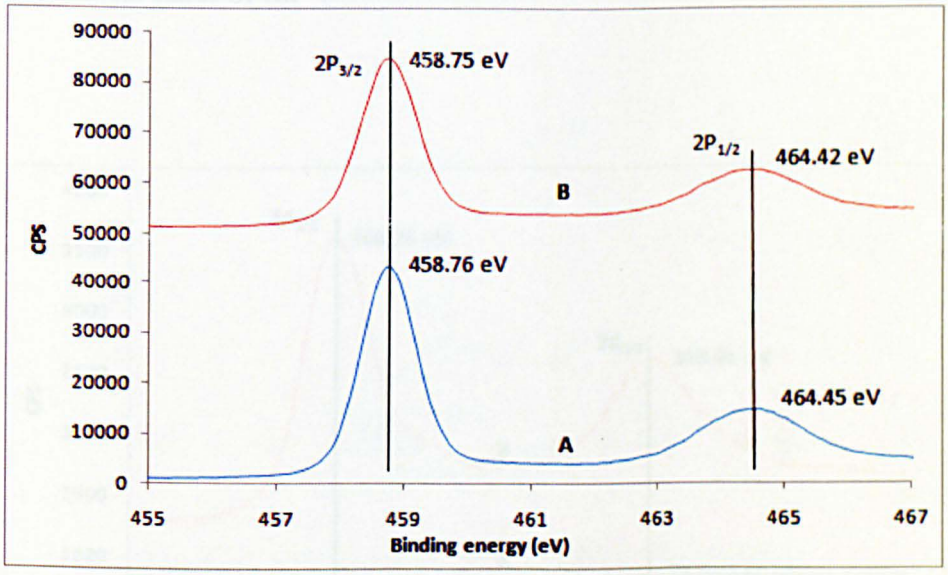

Fig. 4.14: XPS spectra of Ti 2p of SG TiO_2 and Rh/TiO_2. A: SG TiO_2, B: 0.5 wt% Rh/TiO_2.

Fig. 4.15 presents the spectrum of Rh 3d of 0.5 wt% Rh/TiO_2. It can be seen that the peak of Rh $3d_{5/2}$ appeared at the binding energy of 308.26 eV. Such value was consistent with the binding energy of Rh^{3+} (308.3 eV; Weng-Sieh et al., 1997). By combining with the results of powder XRD analysis on Rh/TiO_2

(Section 4.2.2.3), it can be concluded that the added Rh of 0.5 wt% Rh/TiO_2 was doped into the lattice of its TiO_2 support with its chemical state to be Rh^{3+}. It has been reported by Kohno et al. (1999) that the chemical state of the added Rh in the Rh modified TiO_2 could change with increasing the Rh ratio. They reported that the chemical state of the added Rh gradually changed from Rh^{3+} to Rh^0 when the Rh ratio increased from 0.5 wt% to 4 wt% (Kohno et al., 1999). In the case of this work, the chemical state of the added Rh of 0.5 wt% Rh/TiO_2 was Rh^{3+}. Therefore, it can be expected that the added Rh of 0.003-0.1 wt% Rh/TiO_2, the ones with the Rh ratios lower than 0.5 wt%, were also in the chemical states of Rh^{3+}.

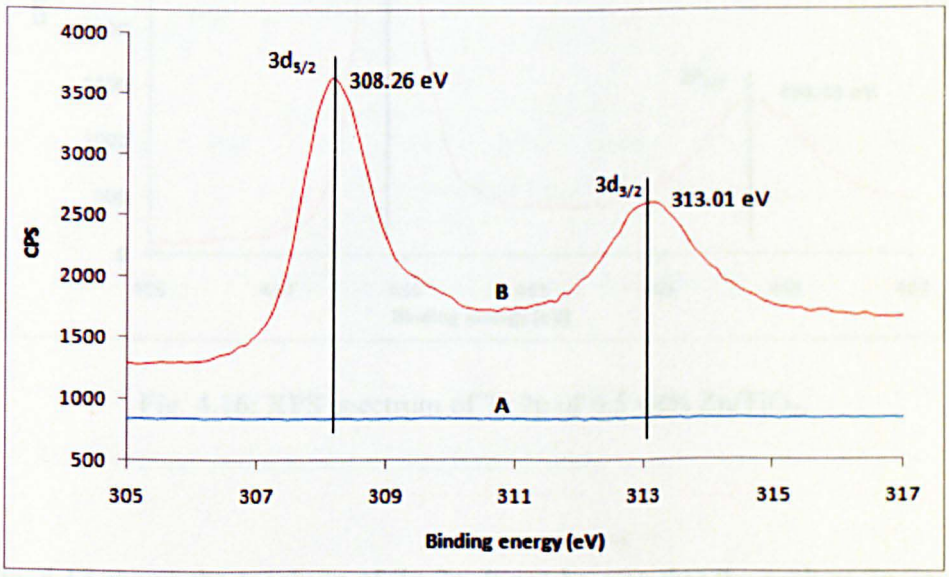

Fig. 4.15: XPS spectra of Rh 3d of SG TiO_2 and Rh/TiO_2. A: SG TiO_2, B: Rh/TiO_2.

4.2.3.4 Spectra of Zn/TiO_2

Figures 4.16 and 4.17 present the XPS spectra of 0.5 wt% Zn/TiO_2. Fig. 4.16 shows that the position of the peak of Ti $2p_{3/2}$ (458.73 eV) was similar to that of SG TiO_2. Therefore, this confirms the crystalline phase of the TiO_2 supports of Zn/TiO_2 to be anatase (as proven by powder XRD, Section 4.2.2.4).

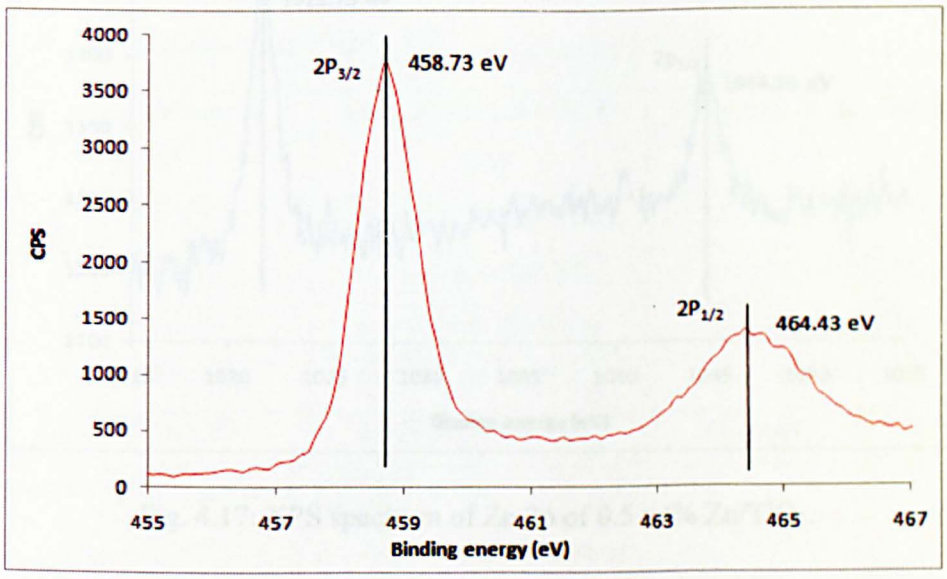

Fig. 4.16: XPS spectrum of Ti 2p of 0.5 wt% Zn/TiO_2.

Fig. 4.17 shows the spectrum of Zn 2p. It can be seen that the peak of Zn $2p_{3/2}$ of 0.5 wt% Zn/TiO_2 appeared at the binding energy of 1021.75 eV. Such value was similar to the binding energy of Zn $2p_{3/2}$ of ZnO (1021.8 eV; Wang et al., 2003). As proven by powder XRD (Section 4.2.2.4), the added Zn of Zn/TiO_2 were loaded to their TiO_2 supports. Therefore, it can be concluded that the added Zn of 0.5 wt% Zn/TiO_2 was loaded to its TiO_2 support with its chemical

state to be ZnO. This indicates that the Zn precursor of 0.5 wt% Zn/TiO_2 could be fully oxidized at the calcination step of the sol-gel synthesis process into ZnO. Hence, it is expected that the Zn precursors of the Zn/TiO_2 with the Zn ratios lower than 0.5 wt% (e.g. 0.05-0.1 wt%) were also fully oxidized into ZnO during the same sol-gel synthesis process.

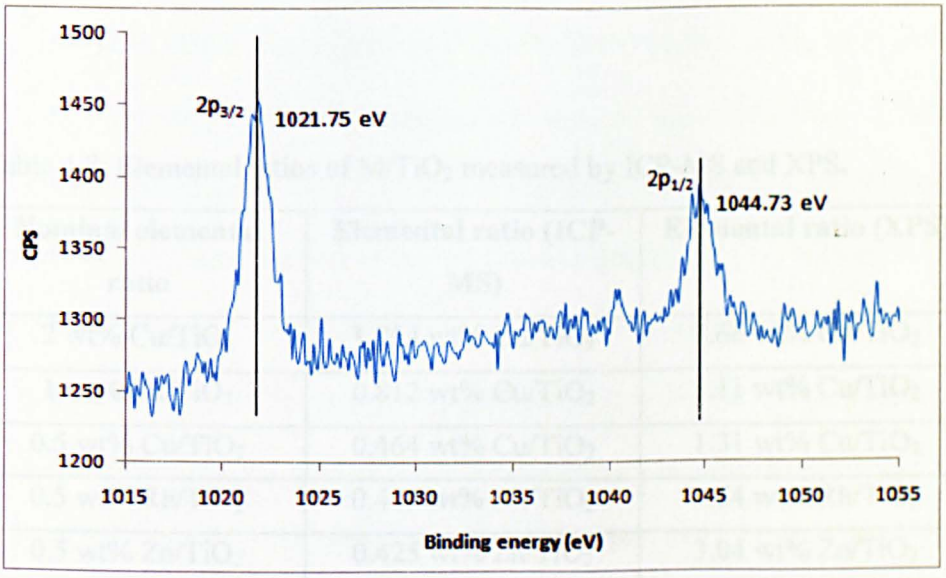

Fig. 4.17: XPS spectrum of Zn 2p of 0.5 wt% Zn/TiO_2.

4.2.3.5 Elemental ratios of the surfaces of M/TiO_2

The elemental ratios of the surfaces of M/TiO_2 were also measured by XPS. Such data are shown in Table 4.8 with the correlated elemental ratios measured by ICP-MS. The standard error of the elemental ratio measurement via XPS is within the range of ± 0.1-0.2 wt%. It can be seen in Table 4.8 that all the surface elemental ratios were significantly higher than those measured by ICP-

MS. This indicates that the added metals were all primarily located on the surfaces of their TiO_2 supports. This is because the added metal precursors were absorbed on the surface of the titanium precursor sol during the hydrolysis step in the sol-gel synthesis process. The added metals were then loaded or doped (depending on the ionic radii of the added metals; Barrett and Massalski, 1980; Li et al., 2005) to the surfaces of TiO_2 after the calcination (Howe, 1998).

Table 4.8: Elemental ratios of M/TiO_2 measured by ICP-MS and XPS.

Nominal elemental ratio	Elemental ratio (ICP-MS)	Elemental ratio (XPS)
2 wt% Cu/TiO_2	1.764 wt% Cu/TiO_2	8.66 wt% Cu/TiO_2
1 wt% Cu/TiO_2	0.812 wt% Cu/TiO_2	3.11 wt% Cu/TiO_2
0.5 wt% Cu/TiO_2	0.464 wt% Cu/TiO_2	1.31 wt% Cu/TiO_2
0.5 wt% Rh/TiO_2	0.489 wt% Rh/TiO_2	4.64 wt% Rh/TiO_2
0.5 wt% Zn/TiO_2	0.425 wt% Zn/TiO_2	3.04 wt% Zn/TiO_2

Elemental ratio was defined as $\frac{\text{Mass of metal}}{\text{Mass of } TiO_2} \times 100$.

4.2.4 Transmission electron microscopy (TEM)

The morphologies of the TiO_2 catalysts were studied by using TEM, and Figures 4.18-4.25 show the images obtained.

Figures 4.18 and 4.19 present the TEM images of the anatase reference and SG TiO_2. It can be seen in Fig. 4.18 that the particles of the anatase reference presented highly irregular sizes ranging from 40 nm up to over 200 nm. In contrast, the particles of SG TiO_2 (Fig. 4.19) presented significantly smaller and more uniform sizes, primarily within the range of 11-16 nm. The average crystallite sizes of the anatase reference (44.77 nm) and SG TiO_2 (13.29 nm) has been estimated by using the Scherrer Formula in Section 4.2.2.1. The particles sizes of the anatase reference and SG TiO_2 obtained in the TEM study indicate that the results of the estimated average crystallite sizes of these catalysts were rational. This is because crystallite is the fine unit composing a particle of a crystalline powder (as introduced in Section 2.3.2.1; Waseda et al., 2011). Therefore, it is reasonable to found that the particle sizes of the anatase reference and SG TiO_2 were not significantly smaller than their estimated average crystallite sizes. Furthermore, the consistency between the particle size (11-16 nm) and estimated average crystallite size (13.29 nm) of SG TiO_2 confirms that the peak broadening in the diffraction pattern of SG TiO_2 was indeed due to the decrease of its crystallite size (Section 4.2.2.1). Otherwise, the crystallite size of SG TiO_2 would be significantly larger than the current estimated one (basing on the Scherrer Formula, Section 2.4.1), which could result in the significantly larger particle size of SG TiO_2 compared to the current TEM-observed one.

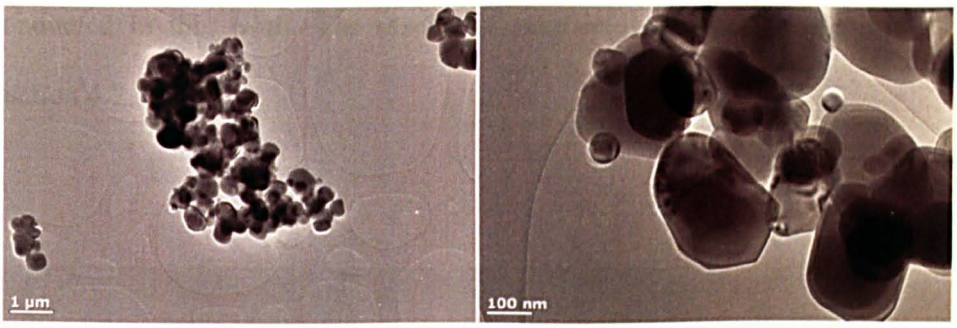

Fig. 4.18: TEM images of the anatase reference.

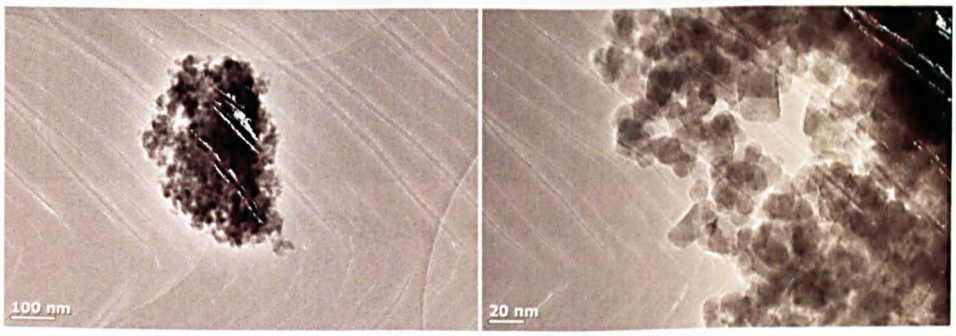

Fig. 4.19: TEM images of SG TiO_2.

Figures 4.20-4.25 show the TEM images of M/TiO_2. It can be seen that their particle sizes, regardless the added metal ratios, were similar to that of SG TiO_2, which were all uniform and primarily within the range of 11-16 nm. Such phenomenon indicates that all the TiO_2 catalysts synthesized via sol-gel process in this work had similar particle sizes.

Furthermore, it is worthy to note that no aggregated metals (example shown in Fig. 2.7; Yang et. al., 2006) were observed in any of the TEM images of the M/TiO_2 presented in this section, even though the results of powder XRD and XPS (Sections 4.2.2 and 4.2.3) have proven that the added Cu and Zn were loaded on the surfaces of their TiO_2 supports. A detailed investigation on the specific surface areas and dispersions of the added Cu of Cu/TiO_2 had been

conducted in this work. The results of such investigation are presented in Section 4.2.5.

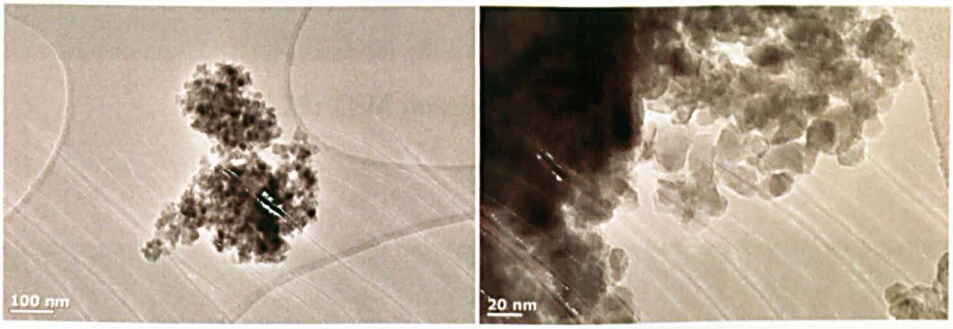

Fig. 4.20: TEM images of 0.03 wt% Cu/TiO_2.

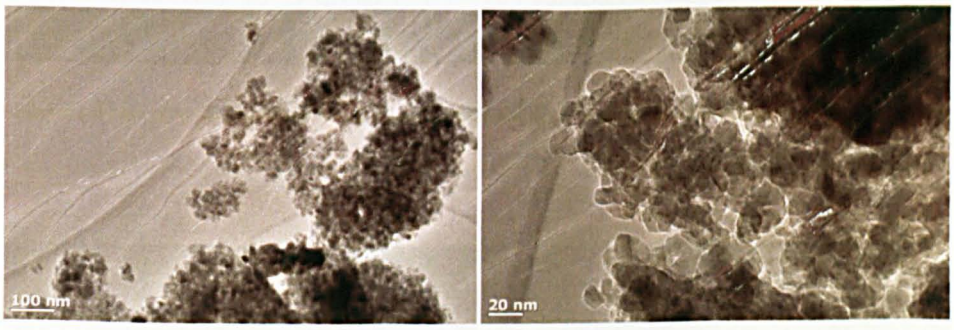

Fig. 4.21: TEM images of 0.5 wt% Cu/TiO_2.

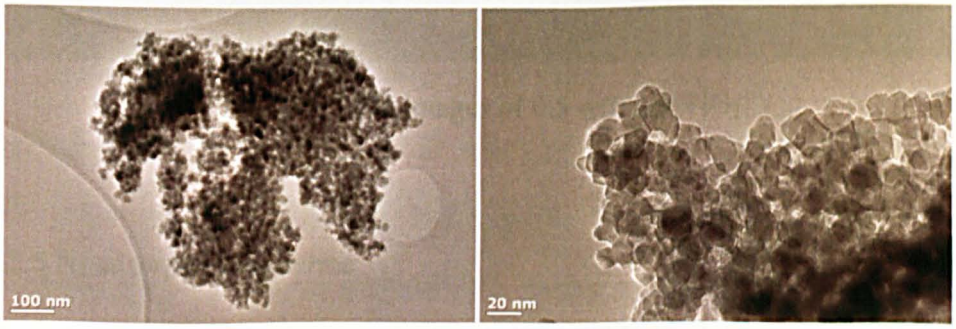

Fig. 4.22: TEM images of 0.01 wt% Rh/TiO_2.

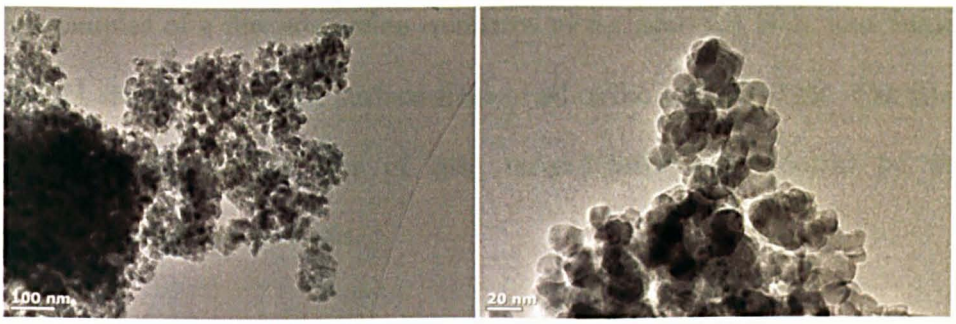

Fig. 4.23: TEM images of 0.5 wt% Rh/TiO_2.

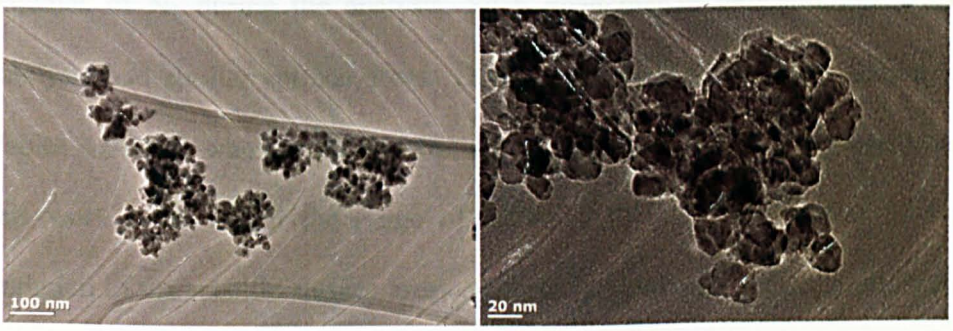

Fig. 4.24: TEM images of 0.1 wt% Zn/TiO_2.

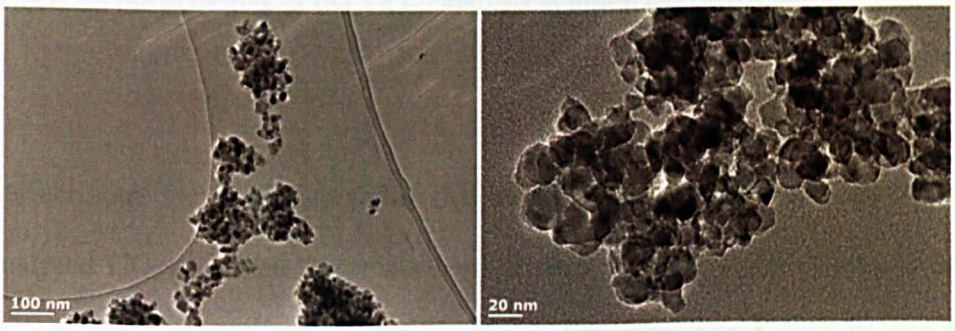

Fig. 4.25: TEM images of 0.5 wt% Zn/TiO_2.

4.2.5 N_2 adsorption isotherms

N_2 adsorption isotherms were used to measure the specific surface areas and porosities of the TiO_2 catalysts synthesized in this work. Fig. 4.26 illustrates

the examples of a few adsorption isotherms of the analysed TiO_2, and Tables 4.9-4.11 shows the specific surface areas of all of the analysed TiO_2. The error of the specific surface area of each measurement was reported by the instrument after each analysis.

It can be seen in Fig. 4.26 that all of these analysed catalysts adsorbed similar volumes of N_2 during the analysis. Such phenomenon indicates that these catalysts had similar surface areas. This is confirmed by the data shown in Tables 4.9-4.11, wherein the specific surface areas of the TiO_2 derived from this work were within the range of 50.24-63.37 m^2/g. The extent of the variation of the specific surface areas of these TiO_2 was small compared to the previous values reported in the literature (65-238 m^2/g; Jung et al., 2000; Tian et al., 2007). It is expected that such surface area variation had no significant effects on the activities of the TiO_2 catalysts synthesized in this work.

Furthermore, Fig. 4.26 also shows that all the N_2 adsorption isotherms of the analysed TiO_2 presented hysteresis loops. Such loop is the typical feature of the N_2 adsorption isotherm of the mesoporous solid material (e.g. type IV and V isotherms, as introduced in Section 2.4.4; Sing et al., 1985; Kruk and Jaroniec, 2001). This means that all the TiO_2 derived from this work were mesoporous. However, the pore volumes of these TiO_2 ranged within 0.0849-0.1022 cm^3/g. Such pore volumes were also too small to effectively affect the activities of the TiO_2 when compared to the values reported previously (not lower than 0.79 cm^3/g; Anpo et al., 1998, Yamashita et al., 1998).

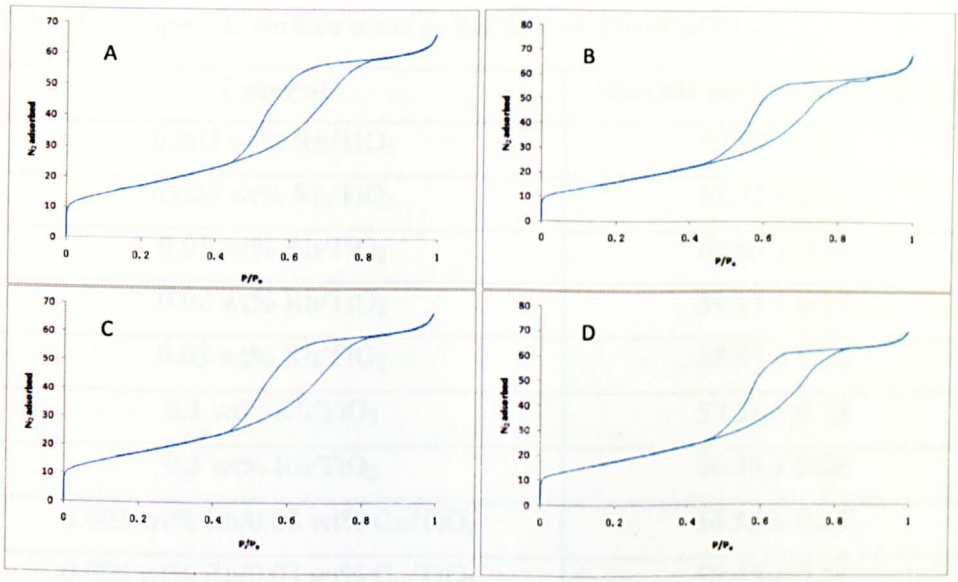

Fig. 4.26: Isotherm graphs of the TiO_2 catalysts. A: SG TiO_2, B: 0.03 wt% Cu/TiO_2, C: 0.01 wt% Rh/TiO_2, D: 0.1 wt% Zn/TiO_2.

Table 4.9: Specific surface areas of SG TiO_2 and Cu/TiO_2.

Catalyst	Specific surface area (m^2/g)
Anatase reference	7.93 ± 0.12
SG TiO_2	54.23 ± 0.17
0.006 wt% Cu/TiO_2	56.07 ± 0.35
0.01 wt% Cu/TiO_2	59.21 ± 0.32
0.02 wt% Cu/TiO_2	55.10 ± 0.26
0.03 wt% Cu/TiO_2	52.99 ± 0.31
0.05 wt% Cu/TiO_2	52.61 ± 0.22
0.07 wt% Cu/TiO_2	52.58 ± 0.29
0.1 wt% Cu/TiO_2	51.75 ± 0.26
0.5 wt% Cu/TiO_2	50.24 ± 0.24

Table 4.10: Specific surface areas of Rh/TiO_2 and $Rh/Cu/TiO_2$.

Catalyst	Specific surface area (m^2/g)
0.003 wt% Rh/TiO_2	53.97 ± 0.11
0.006 wt% Rh/TiO_2	63.37 ± 0.25
0.01 wt% Rh/TiO_2	62.65 ± 0.31
0.02 wt% Rh/TiO_2	59.13 ± 0.25
0.03 wt% Rh/TiO_2	58.93 ± 0.26
0.1 wt% Rh/TiO_2	59.51 ± 0.18
0.5 wt% Rh/TiO_2	56.75 ± 0.28
0.003 wt% Rh/0.03 wt% Cu/TiO_2	54.92 ± 0.33
0.006 wt% Rh/0.03 wt% Cu/TiO_2	58.45 ± 0.34
0.01 wt% Rh/0.03 wt% Cu/TiO_2	60.37 ± 0.18
0.02 wt% Rh/0.03 wt% Cu/TiO_2	59.00 ± 0.32

Table 4.11: Specific surface areas of Zn/TiO_2.

Catalyst	Specific surface area (m^2/g)
0.05 wt% Zn/TiO_2	57.43 ± 0.22
0.07 wt% Zn/TiO_2	62.73 ± 0.22
0.1 wt% Zn/TiO_2	61.36 ± 0.18
0.3 wt% Zn/TiO_2	60.92 ± 0.34
0.5 wt% Zn/TiO_2	59.81 ± 0.28

4.2.6 Specific surface area and dispersion of the added Cu

As proven by XRD and XPS (Sections 4.2.2.2 and 4.2.3), the added Cu of Cu/TiO_2 were loaded on their TiO_2 supports with their chemical states to be Cu_2O in this work. The specific surface areas and dispersions of such added Cu

were measured by using N_2O as adsorbate (background knowledge introduced in Section 2.4.5), and Fig. 4.27 shows the results of such analysis.

It can be seen in Fig. 4.27 that the added Cu presented high values of both specific surface area (926.66-940.83 m^2/g) and dispersion (97.71-99.21 %) when the Cu ratio was within the range of 0.01-0.03 wt%. The extremely high values of the dispersion (almost up to 100 %) indicate that nearly all the atoms of the added Cu of these analysed Cu/TiO_2 were presented on the surface. Such phenomenon means that when the Cu ratio was relatively low, the added Cu was extremely uniformly dispersed on the surfaces of their TiO_2 supports, forming almost 2-dimentional Cu-O-Cu ultra thin films with high specific surface areas.

However, Fig. 4.27 also shows that both the values of the specific surface area and dispersion of the added Cu started to decrease when the Cu ratio exceeded 0.03 wt%. Such values decreased significantly (specific surface area: 24.81 m^2/g, dispersion: 2.62 %) when the Cu ratio increased up to 2 wt%. This phenomenon indicates that when the Cu ratio continued to increase (exceeding 0.03 wt%), the added Cu started to aggregate, forming 3-dimentional Cu particles on the surfaces of their TiO_2 supports.

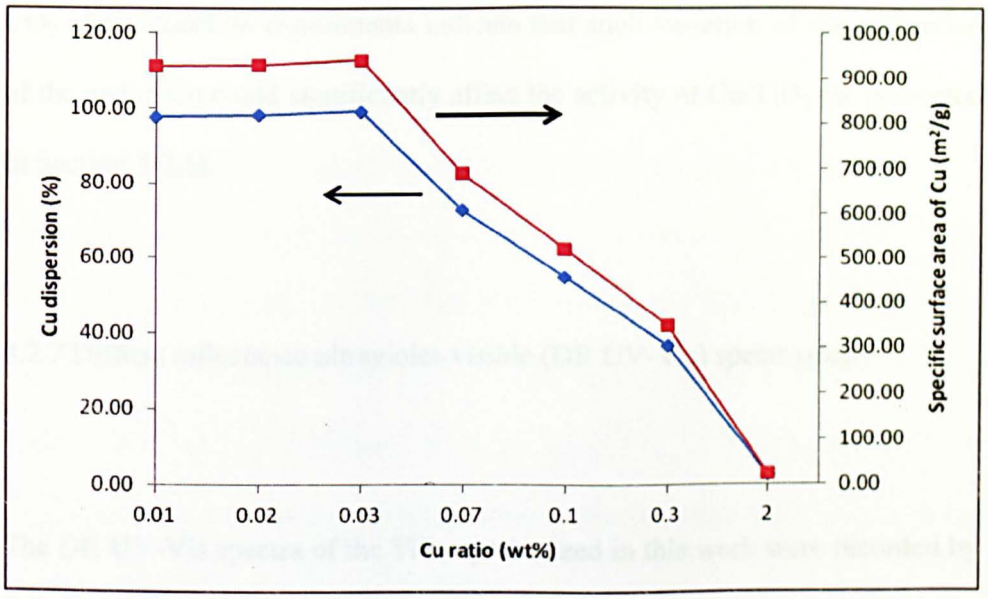

Fig. 4.27: Specific surface areas and dispersions of the added Cu of Cu/TiO_2.

The results presented in this section confirmed that the increase of the Cu ratio of a Cu loaded TiO_2 was indeed able to cause the aggregation of the added Cu (as introduced in Section 2.3.1.3.1; Tseng et al., 2002, 2004). Moreover, when compared to the previous studies that had observed such phenomenon (e.g. Tseng et al., 2002, 2004), this work presents the detailed relation between the Cu ratio increase and the extent of the aggregation of the added Cu. The added Cu of the Cu/TiO_2 (with Cu ratio lower than 2 wt%) analysed by using N_2O as adsorbate were not detectable via powder XRD (as presented in Section 4.2.2.2). Previous studies (Sakthivel et. al., 2004; Madikizela-Mnqanqeni and Coville, 2008) would simply consider such phenomenon as an indication of the uniform dispersion of the added Cu on TiO_2. Whereas, the results presented in this section clearly show that the aggregation of the added Cu had started to occur before such aggregated Cu could be detected via powder XRD or observed via TEM (as presented in Section 4.2.4). The results of the following

CO_2 photoreduction experiments indicate that such variation of the dispersion of the added Cu could significantly affect the activity of Cu/TiO_2 (as presented in Section 5.2.1).

4.2.7 Diffuse reflectance ultraviolet-visible (DR UV-Vis) spectroscopy

The DR UV-Vis spectra of the TiO_2 synthesized in this work were recorded by using a DR UV-Vis spectrometer. Such spectra were used to estimate the threshold wavelengths (measured by using the method introduced in Section 2.4.7; Zhang et. al., 2008) and confirm the chemical states of the added metals of these TiO_2 catalysts. The anatase reference was scanned for three times via the DR UV-Vis spectrometer to assess the precision of this analysis. The result indicates that the error (threshold wavelength) was 0.11 %.

4.2.7.1 DR UV-Vis spectra of the anatase reference and SG TiO_2

Fig. 4.28 shows the DR UV-Vis spectra of the anatase reference and SG TiO_2. The threshold wavelengths of these two catalysts were 388 nm (consistent with the typical value of anatase: 387.5 nm; Xu and Schoonen, 2000) and 406 nm, respectively. It can be seen that, even though the results of powder XRD (Section 4.2.2.1) has well proven that SG TiO_2 was also at the crystalline phase of anatase, the DR UV-Vis spectrum of SG TiO_2 presented an obvious red-shift

compared to that of the anatase reference. Sanchez et al. (1995) reported that this phenomenon was caused by the formation of O vacancies on the surface of TiO_2, which usually occurred during the sol-gel synthesis process under acidic environment. Such O vacancies could be filled by electrons to generate colour centers on the surface of TiO_2 that absorbed visible light (Serpone, 2006). Serpone (2006) reported that the red shift caused by such reason did not indicate a band-gap narrowing of TiO_2. Therefore, it is expected that the formation of the O vacancies, which caused the red-shift, will not affect the activity of SG TiO_2 within visible light.

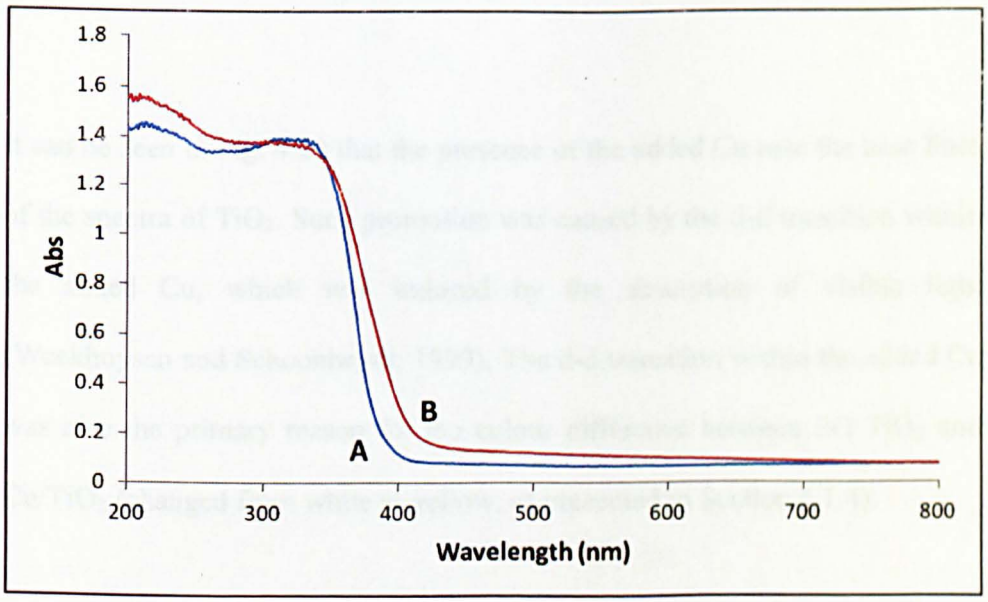

Fig. 4.28: DR UV-Vis spectra of of the pure TiO_2 samples. A: anatase reference and B: SG TiO_2.

4.2.7.2 DR UV-Vis spectra of Cu/TiO_2

The DR UV-Vis spectra of Cu/TiO_2 are shown in Fig. 4.29, and the threshold wavelengths of these analysed catalysts are shown in Table 4.12. It can be seen that the presence of the added Cu caused a significant change for the DR UV-Vis spectra of TiO_2. It is worthy to note that the added Cu was located on the surface of TiO_2 in the chemical state of Cu_2O (proven by powder XRD and XPS; Sections 4.2.2.2 and 4.2.3). Cu_2O is also a widely used semiconductor, and its properties (e.g. band-gap, positions of valence band (VB) and conduction band (CB)) are listed in Table 4.13.

It can be seen in Fig. 4.29 that the presence of the added Cu rose the base lines of the spectra of TiO_2. Such promotion was caused by the d-d transition within the added Cu, which was induced by the absorption of visible light (Weckhuysen and Schoonheydt, 1999). The d-d transition within the added Cu was also the primary reason for the colour difference between SG TiO_2 and Cu/TiO_2 (changed from white to yellow, as presented in Section 4.1.4).

Meanwhile, characteristic absorption bands within the range of 400-600 nm were observed in the spectra of Cu/TiO_2. Previous studies (Golon et al., 2006; Huang et al., 2009) reported that this was caused by the presence of Cu_2O, a semiconductor with relatively smaller band-gap compared to that of anatase, as shown in Table 4.13. This further confirms the chemical state of the added Cu

to be Cu_2O. On the other hand, even though the presence of such added Cu caused red-shift to the DR UV-Vis spectra of TiO_2 (Table 4.12), this did not indicate the band-gap narrowing of TiO_2. This is because the TiO_2 supports of Cu/TiO_2 were all in the crystalline phase of anatase (Section 4.2.2.2), and the position of the CB of Cu_2O is more negative than that of anatase (as shown in Table 4.13). Therefore, the electrons on the CB of Cu_2O generated via the absorption of visible light are not favourable to transfer to that of anatase. Hence, the red-shift of the spectra of TiO_2 caused by the presence of the added Cu did not indicate the band-gap narrowing of TiO_2.

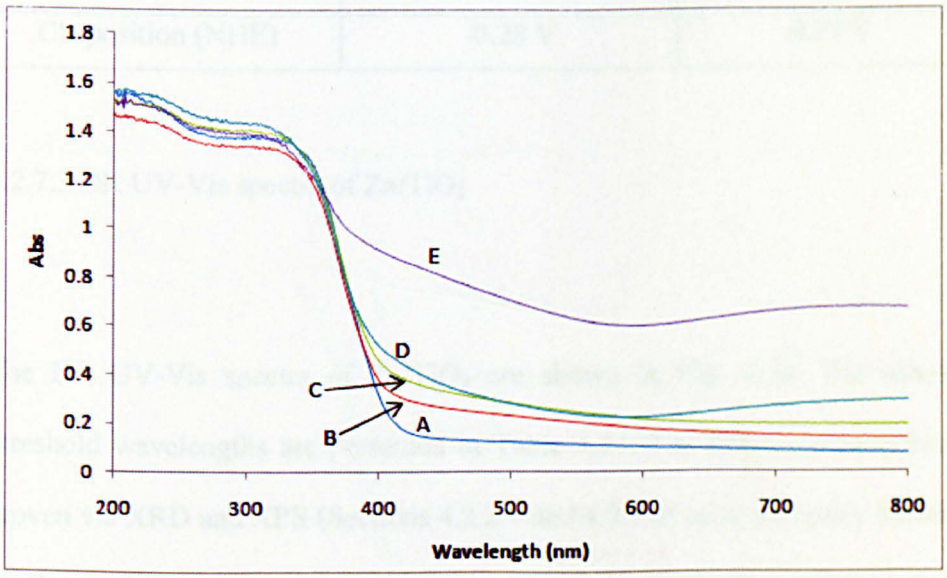

Fig. 4.29: DR UV-Vis spectra of Cu/TiO_2. A: SG TiO_2, B: 0.03wt%Cu/TiO_2, C: 0.1wt%Cu/TiO_2, D: 0.5wt%Cu/TiO_2, E: 10wt%Cu/TiO_2.

Table 4.12: Threshold wavelengths of Cu/TiO_2.

Catalyst	Threshold wavelength (nm)
SG TiO_2	406
0.03 wt% Cu/TiO_2	406
0.1 wt% Cu/TiO_2	407
0.5 wt% Cu/TiO_2	420
10 wt% Cu/TiO_2	455

Table 4.13: Band-gap, threshold wavelength, and VB and CB positions of Cu_2O and anatase (Xu and Schoonen, 2000).

	Cu_2O	Anatase
Band-gap	2.2 eV	3.2 eV
Threshold wavelength	563.64 nm	387.50 nm
VB position (NHE)	1.92 V	2.91 V
CB position (NHE)	-0.28 V	-0.29 V

4.2.7.3 DR UV-Vis spectra of Zn/TiO_2

The DR UV-Vis spectra of Zn/TiO_2 are shown in Fig. 4.30. The related threshold wavelengths are presented in Table 4.14. The added Zn have been proven via XRD and XPS (Sections 4.2.2.4 and 4.2.3.4) to be primarily located on the surfaces of theirs TiO_2 supports in the chemical states of ZnO. It is worthy to note that ZnO is also a semiconductor, and Table 4.15 shows the properties of ZnO.

It can be seen in Fig. 4.30 and Table 4.14 that the presence of the added Zn did not cause any significant changes in the DR UV-Vis spectra of TiO_2, even if

the Zn ratio increased up to 10 wt%. This is because the added Zn was at the chemical state of ZnO. Such material has the same colour (white, presented in Section 4.1.4), and the similar band-gap and band-edge positions (Table 4.15) as its TiO_2 support. The white colour determines that ZnO did not significantly absorb visible light to induce d-d transition (Weckhuysen and Schoonheydt, 1999), leading to no significant rising of the base line of the spectra of Zn/TiO_2 in contrast to that of SG TiO_2. On the other hand, the band-gap and band-edge positions of ZnO are both similar as those of anatase (Table 4.15). This determines that ZnO could present similar DR UV-Vis spectrum as that of its TiO_2 support. Therefore, the presence of the added Zn, in the chemical state of ZnO, was not able to significantly change the DR UV-Vis spectra of TiO_2.

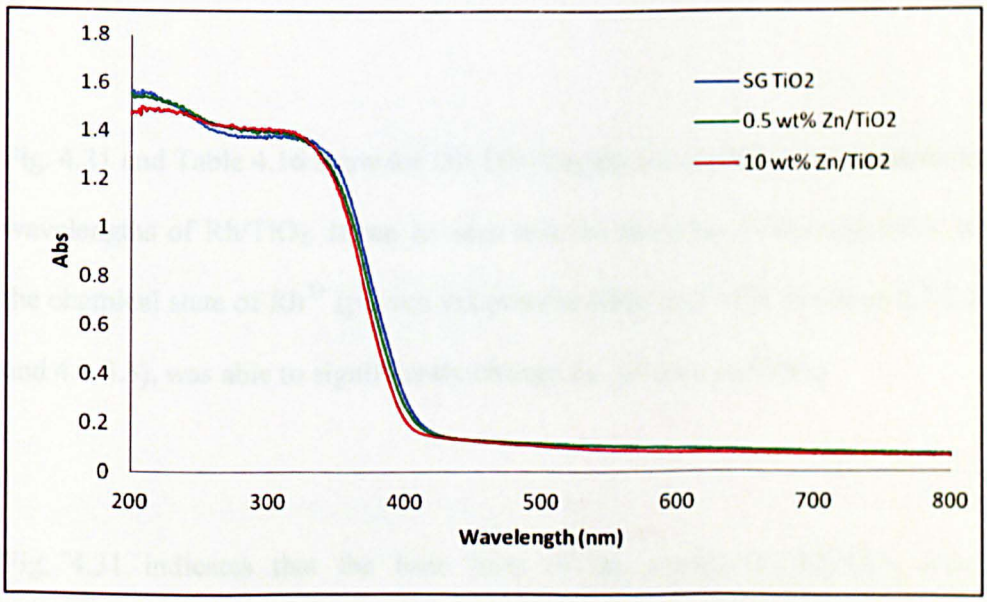

Fig. 4.30: DR UV-Vis spectra of Zn/TiO_2.

Table 4.14: Threshold wavelengths of Zn/TiO_2.

Catalyst	Threshold wavelength (nm)
SG TiO_2	406
0.5wt%Zn/TiO_2	406
10wt%Zn/TiO_2	405

Table 4.15: Band-gaps, threshold wavelengths, and VB and CB positions of ZnO and anatase (Xu and Schoonen, 2000).

	ZnO	Anatase
Band-gap	3.2 eV	3.2 eV
Threshold wavelength	387.50 nm	387.50 nm
VB position (NHE)	2.89 V	2.91 V
CB position (NHE)	-0.31 V	-0.29 V

4.2.7.4 DR UV-Vis spectra of Rh/TiO_2

Fig. 4.31 and Table 4.16 show the DR UV-Vis spectra and the related threshold wavelengths of Rh/TiO_2. It can be seen that the presence of the added Rh, in the chemical state of Rh^{3+} (proven via powder XRD and XPS, Sections 4.2.2.3 and 4.2.3.3), was able to significantly change the spectrum of TiO_2.

Fig, 4.31 indicates that the base lines of the spectra of Rh/TiO_2 were significantly rose, in contrast to that of SG TiO_2. This was caused by the d-d transition within the added Rh induced via the absorption of visible light (Weckhuysen and Schoonheydt, 1999), which also led to the colour change of TiO_2 from white to dark grey (as presented in Section 4.1.4). Meanwhile,

characteristic absorption bands within the range of 400-600 nm were observed in the spectra of Rh/TiO_2. Such absorption band caused the red-shift of the spectra of Rh/TiO_2 in contrast to that of SG TiO_2 (Table 4.16). It is reported that this was attributed to the presence of Rh^{3+} on TiO_2 (Choi et al., 1994; Dai et al., 2009). Such result confirms the chemical state of the added Rh to be Rh^{3+} (as proven by XPS, Section 4.2.3.3).

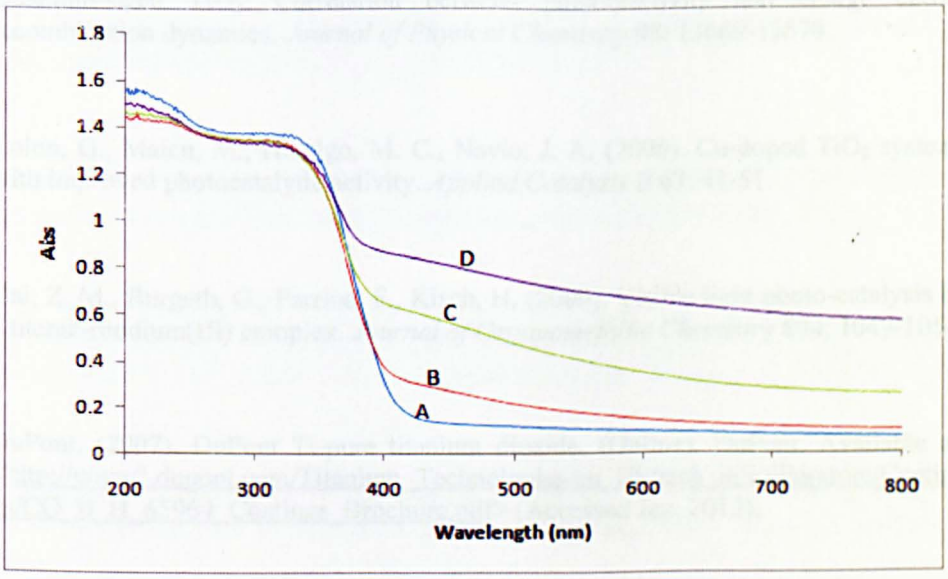

Fig. 4.31: DR UV-Vis spectra of Rh/TiO_2. A: SG TiO_2, B: 0.006 wt% Rh/TiO_2, C: 0.1 wt% Rh/TiO_2, D: 0.5 wt% Rh/TiO_2.

Table 4.16: Threshold wavelengths of Rh/TiO_2.

Catalyst	Threshold wavelength (nm)
SG TiO_2	406
0.006wt%Rh/TiO_2	407
0.1wt%Rh/TiO_2	410
0.5wt%Rh/TiO_2	412

References

Anpo, M., Yamashita, H., Ikeue, K., Fujii, Y., Zhang, S. G., Ichihashi, Y., Park, D. R., Suzuki, Y., Koyano, K., Tatsumi, T. (1998) Photocatalytic reduction of CO_2 with H_2O on Ti-MCM-41 and Ti-MCM-48 mesoporous zeolite catalysts. *Catalysis Today* **44**: 327-332.

Barrett, C. S., Massalski, T. B. (1980). *Structure of metals, 3rd ed.* Pergamon Press. Oxford, New York, Ontario, Potts Point, Paris, and Hammerweg.

Choi, W. Termin, A., Hoffmann, M. R. (1994). The role of metal ion dopants in Quantum-sized TiO_2: Correlation between photoreactivity and charge carrier recombination dynamics. *Journal of Physical Chemistry* **98**: 13669-13679.

Colon, G., Maicu, M., Hidalgo, M. C., Navio, J. A. (2006). Cu-doped TiO_2 systems with improved photocatalytic activity. *Applied Catalysis B* **67**: 41-51.

Dai, Z. M., Burgeth, G., Parrino, F., Kisch, H. (2009). Visible light photo-catalysis by a titania-rhodium(III) complex. *Journal of Organometallic Chemistry* **694**: 1049-1054.

DuPont. (2007). DuPont Ti-pure titanium dioxide. (Online). DuPont. Available at: <http://www2.dupont.com/Titanium_Technologies/en_US/tech_info/literature/Coatings/CO_B_H_65969_Coatings_Brochure.pdf> (Accessed Jan. 2012).

Fisher Scientific. (2004). Copper(II) chloride anhydrous MSDS. (Online). Fisher Scientific. Available at: <https://fscimage.fishersci.com/msds/91790.htm> (Accessed Jan. 2012).

Fisher Scientific. (2009). Rhodium acetate, dimer, dihydrate MSDS. (Online). Fisher Scientific. Available at: <http://www.chemdb-portal.cn/fisher_msds_pdf/29998-99-0_EN.pdf> (Accessed Jan. 2012).

Huang, L., Peng, F., Wang, H. J., Yu, H., Li, Z. (2009). Preparation and characterization of Cu_2O/TiO_2 nano-nano heterostructure photocatalysts. *Catalysis Communications* **10**: 1839-1843.

Howe, R. F. (1998). Recent developments in photocatalysis. *Developments in Chemical Engineering and Mineral Processing* **6**: 55.

Iowa State University. (2001). Copper(I) oxide MSDS. Iowa State University. (Online). Available at: <http://avogadro.chem.iastate.edu/MSDS/copper(I)_oxide.html> (Accessed Jan. 2012).

Jung, K. Y., Park, S. B. (2000). Park, Enhanced photoactivity of silica-embedded titania particles prepared by sol-gel process for the decomposition of trichloroethylene. *Applied Catalysis B* **25**: 249-256.

Jenkins, R., Snyder, R. L. (1996). *Introduction to X-ray powder diffractometry*. John Wiley & Sons Inc. New York.

Kohno, Y., Hayashi, H., Takenaka, S., Tanaka, T., Funabiki, T. (1999). Photo-enhanced reduction of carbon dioxide with hydrogen over Rh/TiO_2. *Journal of Photochemistry and Photobiology A* **126**: 117-123.

Kruk, M., Jaroniec, M. (2001). Gas adsorption characterization of ordered organic-inorganic nanocomposite materials. *Chemistry of Materials* **13**: 3169-3183.

Li, W., Frenkel, A. I., Woicik, J. C., Ni, C., Ismat Shah, S. (2005). Dopant location identification in Nd^{3+}-doped TiO_2 nanoparticles. *Physical Review B* **72**: 155315.

Madikizela-Mnqanqeni, N. N., Coville, N. J. (2008). The effect of sulphur addition during the preparation of $Co/Zn/TiO_2$ Fischer-Tropsch catalyst. *Applied Catalysis A* **340**: 7-15.

Prokes, S. M., Gole, J. L., Chen, X., Burda, C., Carlos, W. E. (2005). Defect-related optical behaviour in surface modified TiO_2 nanostructures. *Advanced Functional Materials* **15**: 161-167.

Rensmo, H., Lindstrom, H., Hagfeldt, A., Lindquist, S. (1997). Lithium intercalation in nanoporous anatase TiO_2 studied with XPS. *Journal of Physical Chemistry B* **101**: 3087-3090.

Sakthivel, S., Shankar, M. V., Palanichamy, M., Arabindoo, B., Bahnemann, D. W., Murugesan, V. (2004). Enhancement of photocatalytic activity by metal deposition: characterisation and photonic efficiency of Pt, Au, and Pd deposited on TiO_2 catalyst. *Water Research* **38**: 3001-3008.

Sanchez, E., Lopez, T. (1995). Effect of the preparation method on the band gap of titania and platinum-titania sol-gel materials. *Materials Letters* **25**: 271-273.

Sing, K. S. W., Everett, D. H., Haul, R. A. W., Moscou, L., Pierotti, R. A., Rouquerol, J., Siemieniewska, T. (1985). Reporting physisorption data for gas/solid systems with special reference to the determination of surface area and porosity. *Pure & Applied Chemistry* **57**: 603-619.

Science Lab. (2010a). Cupric chloride dihydrate MSDS. (Online). Science Lab. Available at: <http://www.sciencelab.com/msds.php?msdsId=9923592> (Accessed Jan. 2012).

Science Lab. (2010b). Zinc chloride MSDS. (Online). Science Lab. Available at: <http://www.sciencelab.com/msds.php?msdsId=9927328> (Accessed Jan. 2012).

Science Lab. (2010c). Zinc oxide MSDS. (Online). Science Lab. Available at: <http://www.sciencelab.com/msds.php?msdsId=9927329> (Accessed Jan. 2012).

Shannon, R. D. (1976). Revised effective ionic radii and systematic studies of interatomic distances in halides and chalcogenides. *Acta Crystallographica A* **32**: 751.

Serpone, N. (2006). Is the band gap of pristine TiO_2 narrowed by anion- and cation-doping of titanium dioxide in second-generation photocatalysts? *Journal of Physical Chemistry B* **110**: 24287-24293.

Tseng, I. H., Chang, W. C., Wu, J. C. S. (2002). Photoreduction of CO_2 using sol-gel derived titania and titania-supported copper catalysts. *Applied Catalysis B* **37**: 37-48.

Tseng, I. H., Wu, J. C. S. (2004). Chemical states of metal-loaded titania in the photoreduction of CO_2. *Catalysis Today* **97**: 113-119.

Tian, G. H., Fu, H. G., Jing, L. Q., Xin, B. F., Pan, K. (2008). Preparation and characterization of stable biphase TiO_2 photocatalyst with high crystallinity, large surface area, and enhanced photoactivity. *Journal of Physical Chemistry C* **112**: 3083-3089.

Weng-Sieh, Z., Gronsky, R., Bell, A. T. (1997). Microstructural evolution of γ-alumina-supported Rh upon aging in air. *Journal of Catalysis* **170**: 62-74.

Wu, J. C. S., Yeh, C. Y. (2001). Sol-gel derived photosensitive TiO_2 and Cu/TiO_2 esing homogeneous hydrolysis technique. *Journal of Materials Research* **16**: 2.

Wu, J. C. S., Tseng, I. H., Chang, W. C. (2001). Synthesis of titania-supported copper nanoparticles via refined alkoxide sol-gel process. *Journal of Nanoparticle Research* **3**: 113-118.

Wang, Z., Zhang, H., Zhang, L., Yuan, J., Yan, S., Wang, C. (2003). Low-temperature synthesis of ZnO nanoparticles by solid-state pyrolytic reaction. *Nanotechnology* **14**: 11-15.

Weckhuysen, B. M., Schoonheydt, R. A. (1999). Recent progress in diffuse reflectance spectroscopy of supported metal oxide catalysts. *Catalysis Today* **49**: 441-451.

Xu, Y., Schoonen, M. A. A. (2000). The absolute energy positions of conduction and valence bands of selected semiconducting minerals. *American Mineralogist* **85**: 543-556.

Xin, B., Jing, L., Ren, Z., Wang, B., Fu, H. (2005). Effects of simultaneously doped and deposited Ag on the photocatalytic activity and surface states of TiO_2. *Journal of Physical Chemistry B* **109**: 2805-2809.

Yang, Y. Z., Chang, C. H., Idriss, H. (2006). Photo-catalytic production of hydrogen form ethanol over M/TiO_2 catalysts (M=Pd, Pt or Rh). *Applied Catalysis B* **67**: 217-222.

Yamashita, H., Fujii, Y., Ichihashi, Y., Zhang, S. G., Ikeue, K., Park, D. R., Koyano, K., Tatsumi, T., Anpo, M. (1998). Selective formation of CH_3OH in the photocatalytic reduction of CO_2 with H_2O on titanium oxides highly dispersed within zeolites and mesoporous molecular sieves. *Catalysis Today* **45**: 221-227.

Zhang, Y. J., Yan, W., Wu, Y. P., Wang, Z. H. (2008). Synthesis of TiO_2 nanotubes coupled with CdS nanoparticles and production of hydrogen by photocatalytic water decomposition, *Materials Letters* **62**: 3846-3848.

Chapter 5: Photocatalytic reduction of CO_2

As described in Chapter 3, TiO_2 catalysts, either pure (referred as SG TiO_2) or modified by metals (referred as M/TiO_2), were synthesized via sol-gel process in this work. These catalysts were characterized by using a series of analytical techniques, and the data of such analysis are presented in Chapter 4. These sol-gel derived TiO_2 catalysts were then tested for CO_2 photoreduction. This chapter reports the results of these experiments.

5.1 CO_2 photoreduction catalysed by Anatase reference and SG TiO_2

The anatase reference (Acros Organics, 99%) and SG TiO_2 were tested for CO_2 photoreduction. The procedure and conditions of such experiments are described in Section 3.4.1. The experiments were conducted when irradiated by UVA lamps. Because the threshold wavelengths of the anatase reference and SG TiO_2 were 388 nm and 406 nm, respectively (measured by using DR UV-Vis spectrometer, Section 4.2.7.1); the UVA light (wavelength 365 nm) is believed to be able to activate these catalysts during the experiment. After 1.5-hr irradiation, methane was found to be the only detectable product. The results of CO_2 photoreduction catalysed by the anatase reference and SG TiO_2 are shown in Table 5.1. It is worthy to note that SG TiO_2 was tested three times under identical conditions for CO_2 photoreduction to confirm the

reproducibility of the study, and the error (1.5-hr methane production) was calculated to be 1.51 %.

It can be seen in Table 5.1 that SG TiO_2 was able to successfully catalyse CO_2 photoreduction into methane. In contrast, the anatase reference did not show any activity for the same purpose. As these two catalysts were in the same crystalline phase of anatase (as proven via powder XRD, Section 4.2.2.1), their different performances for CO_2 photoreduction should be primarily due to the differences on their particle sizes and specific surface areas (Koci et al., 2009; Jung et al., 2000; Tian et al., 2007).

Table 5.1: Results of the 1.5-hr reactions of CO_2 photoreduction catalysed via the anatase reference and SG TiO_2.

Catalyst	**1.5-hr methane production (nmol)**	**Quantum efficiency (10^{-4} %)**	**Conversion of CO_2 (10^{-5} %)**
Anatase reference	0	0	0
SG TiO_2	3.10	3.25	2.42

The particle sizes of SG TiO_2 and the anatase reference were observed via TEM (Section 4.2.4) to be 11-16 nm and 40-200 nm, respectively. The particle size of SG TiO_2 was within the range optimal for CO_2 photoreduction (around 14 nm; as introduced in Section 2.3.2.1; Koci et al., 2009). In contrast, the particle size of the anatase reference was too large (> 29 nm), and this could increase the bulk recombination rate of the photo-generated electrons and holes within the anatase reference (Serpone et al., 1995). Furthermore, the

surface-area-to-volume ratios (SA:V) of SG TiO_2 and the anatase reference were calculated via dividing their external surface areas of their particles (calculated via their radii estimated by TEM, Section 4.2.4) by their volumes. It can be found that the SA:V of SG TiO_2 and the anatase reference were 0.55-0.38 nm^{-1} and 0.15-0.03 nm^{-1}, respectively. The values of SA:V of SG TiO_2 were also much larger than those of the anatase reference, which were advantageous for the better activity of SG TiO_2 compared to that of the anatase reference.

Moreover, the specific surface areas of SG TiO_2 and the anatase reference were measured via N_2 adsorption isotherms (Section 4.2.5) to be 54.23 m^2/g and 7.93 m^2/g, respectively. As described in Section 2.4.4 (Jung et al., 2000; Tian et al., 2007), higher specific surface areas can result in higher activity, and thus may contribute to the better activity of SG TiO_2 compared to that of the anatase reference.

In conclusion, both the differences on the particle sizes and the specific surface areas determine that it is rational for SG TiO_2 to present better activity than the anatase reference for photoreduction of CO_2 into methane.

5.2 CO_2 photoreduction catalysed by M/TiO_2

M/TiO_2 were tested for CO_2 photoreduction. The procedure and conditions of these experiments were the same as the ones described in Section 3.4.1. Methane was found to be the only detectable product after the reactions. Therefore, the productions of methane were used to assess the activities of M/TiO_2. It has been proven via powder XRD (Section 4.2.2), TEM (Section 4.2.4), and N_2 isotherms (Section 4.2.5) that all the sol-gel derived TiO_2 catalysts (both SG TiO_2 and M/TiO_2) had the same crystalline phase of anatase, and similar specific surface areas (50.24-63.37 m^2/g) and particle sizes (11-16 nm). Therefore, the differences between the activities of M/TiO_2 and that of SG TiO_2 reported in this section were primarily attributed to the effects of the added metals.

5.2.1 Cu/TiO_2

The results of the 1.5-hr reactions of CO_2 photoreduction catalysed by Cu/TiO_2 when irradiated by UVA light are shown in Table 5.2 and Fig. 5.1. The optimal Cu/TiO_2 (0.03 wt% Cu/TiO_2) was tested three times under identical conditions for CO_2 photoreduction to confirm the reproducibility of the studies, and the error (1.5-hr methane production) was calculated to be 1.60 %.

Table 5.2: Results of the 1.5-hr reactions of CO_2 photoreduction catalysed via Cu/TiO_2.

Catalyst	1.5-hr methane production (nmol)	Quantum efficiency (10^{-4} %)	Conversion of CO_2 (10^{-5} %)
SG TiO_2	3.10	3.25	2.42
0.01 wt% Cu/TiO_2	25.98	27.20	20.30
0.02 wt% Cu/TiO_2	30.98	32.42	24.20
0.03 wt% Cu/TiO_2	36.11	37.81	28.21
0.04 wt% Cu/TiO_2	35.94	37.63	28.08
0.05 wt% Cu/TiO_2	34.50	36.12	26.95
0.07 wt% Cu/TiO_2	23.37	24.47	18.26
0.1 wt% Cu/TiO_2	15.38	16.10	12.02
0.3 wt% Cu/TiO_2	3.34	3.50	2.61
0.5 wt% Cu/TiO_2	2.56	2.68	2.00

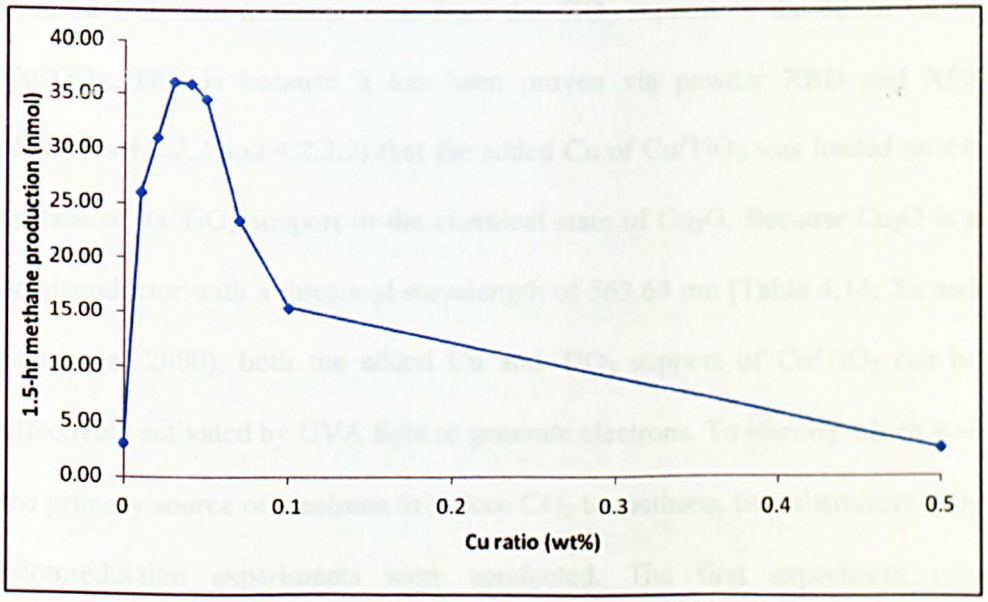

Fig. 5.1: 1.5-hr methane production from CO_2 photoreduction by using Cu/TiO_2 as catalyst.

It can be seen in Table 5.2 and Fig. 5.1 that the activity of Cu/TiO_2 for methane production was greatly affected by the Cu ratio. The methane production increased when the Cu ratio increased in the range of 0-0.03 wt%. The activity of TiO_2 was significantly improved by the presence of such extremely small amount of Cu, wherein the activity of the best-performing 0.03 wt% Cu/TiO_2 for methane production was dramatically (1064.84%) higher than that of SG TiO_2. On the other hand, when the Cu ratio exceeded 0.03 wt%, the activity of Cu/TiO_2 started to decrease.

To understand the performance of Cu/TiO_2, as shown in Table 5.2 and Fig. 5.1, it is firstly necessary to define whether the photo-generated electrons to reduced CO_2 into methane were from the TiO_2 support or the added Cu of Cu/TiO_2. This is because it has been proven via powder XRD and XPS (Sections 4.2.2.2 and 4.2.3.2) that the added Cu of Cu/TiO_2 was loaded on the surface of its TiO_2 support in the chemical state of Cu_2O. Because Cu_2O is a semiconductor with a threshold wavelength of 563.64 nm (Table 4.14; Xu and Schoonen, 2000), both the added Cu and TiO_2 support of Cu/TiO_2 can be effectively activated by UVA light to generate electrons. To identify which was the primary source of electrons to reduce CO_2 to methane, two alternative CO_2 photoreduction experiments were conducted. The first experiment was performed by using 0.03 wt% Cu/TiO_2 as catalyst, which was irradiated by visible light (via a 500 W visible halogen lamp) rather than UVA light. The second experiment was catalysed via SG TiO_2 mixed with Cu_2O powders (copper (I) oxide, 97%, Acros Organics), wherein the ratio of Cu_2O/SG TiO_2 was 0.03 wt% (referred as 0.03 wt% Cu_2O/SG TiO_2). Such experiment was

irradiated by UVA light. The results of these two experiments are shown in Table 5.3.

Table 5.3: 1.5-hr methane production of the alternative CO_2 photoreduction experiments.

Catalyst	Amount of methane produced after 1.5-hr reaction (nmol)
0.03 wt% Cu/TiO_2 irradiated by visible light	0
0.03 wt% Cu/TiO_2 irradiated by UVA light	36.11
0.03 wt% Cu_2O/SG TiO_2 irradiated by UVA light	2.96
SG TiO_2 irradiated by UVA light	3.10

It can be seen in Table 5.3 that 0.03 wt% Cu/TiO_2 exhibited no activity for methane production when irradiated by visible light, even though such catalyst was the optimal Cu/TiO_2 when irradiated by UVA light. The result of this experiment proves that the added Cu, with the chemical state of Cu_2O, on the surface of Cu/TiO_2 was not the primary source of the photo-generated electrons for CO_2 photoreduction. This is because only the added Cu, rather than its TiO_2 support, of Cu/TiO_2 could be effectively activated by visible light (wavelength: 400-800 nm). Therefore, the poor performance of 0.03 wt% Cu/TiO_2 when irradiated by visible light indicates that the photo-generated electrons from the added Cu of Cu/TiO_2 were not able to effectively induce the reaction of CO_2 photoreduction into methane.

Moreover, Table 5.3 also shows that the activity for methane production of 0.03 wt% Cu_2O/SG TiO_2 was similar to that of SG TiO_2, when both of these

catalysts were irradiated by UVA light. This phenomenon further confirms that the TiO_2 support, rather the added Cu, of Cu/TiO_2 was the primary contributor to the photo-generated electrons for CO_2 photoreduction. This is because, when irradiated by UVA light, both Cu_2O and SG TiO_2 could be effectively activated. Therefore, the similar methane productions of 0.03 wt% Cu_2O/SG TiO_2 and SG TiO_2 indicate that TiO_2 was primarily responsible to initiate the reaction of CO_2 photoreduction into methane. It can be concluded from the results shown in Table 5.3 that the TiO_2 support of Cu/TiO_2 was the primary source of the photo-generated electrons for CO_2 photoreduction.

Furthermore, the correspondence between the 1.5-hr methane production from CO_2 photoreduction via Cu/TiO_2 and the specific surface area/dispersion of the added Cu measured by using N_2O as adsorbate (Section 4.2.6) is shown in Fig. 5.2. Meanwhile, the correlation between the 1.5-hr methane production and Cu dispersion of Cu/TiO_2 is presented in Fig. 5.3.

It can be seen from Fig. 5.2 that the specific surface area/dispersion of the added Cu played a key role on determining the activity of Cu/TiO_2. The activity of Cu/TiO_2 for methane production steadily increased when the Cu ratio increased within the range of 0-0.03 wt%, which was the range that the added Cu maintained the high values of specific surface area (926.66-940.83 m^2/g) and dispersion (97.71-99.21 %). However, when the Cu ratio exceeded 0.03 wt%, the activity of Cu/TiO_2 decreased rapidly as the Cu specific surface area and dispersion started to decrease (940.83-24.81 m^2/g and 99.21-36.78 %,

respectively). This phenomenon indicates that the activity of Cu/TiO_2 started to decrease when the aggregation of the added Cu occurred. Fig. 5.3 further shows that the activity of Cu/TiO_2 presented a clear linear correlation with the dispersion of the added Cu. The results shown in Figures 5.2 and 5.3 indicate that the added Cu of Cu/TiO_2 could be the active sites on the surface of its TiO_2 support for CO_2 photoreduction. Therefore, when the aggregation of the added Cu started to occur, the active site on the surface of Cu/TiO_2 were reduced, resulting in the decrease of the activity of Cu/TiO_2.

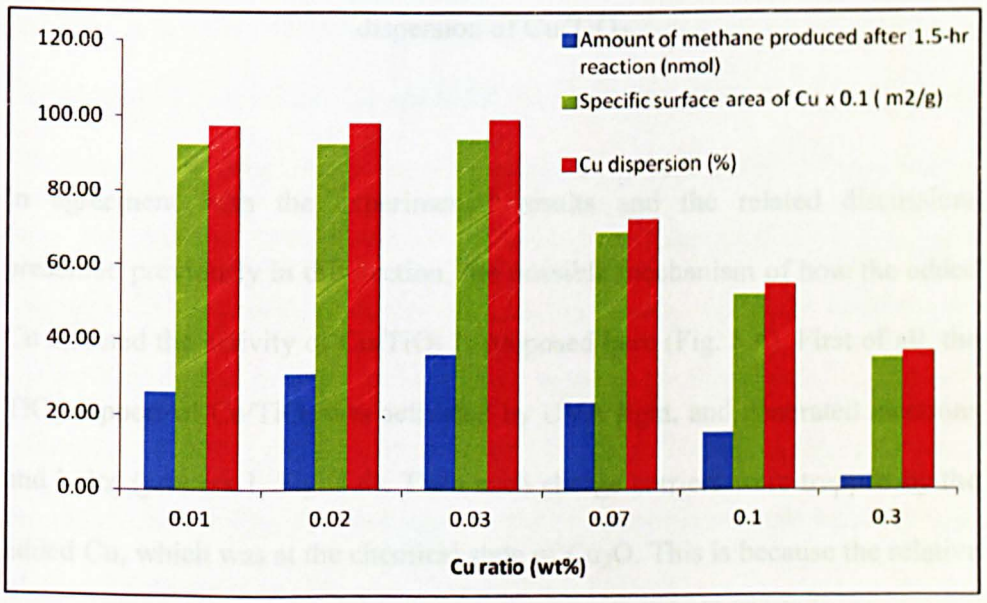

Fig. 5.2: Correspondence between the 1.5-hr methane production and Cu specific surface area/dispersion of Cu/TiO_2.

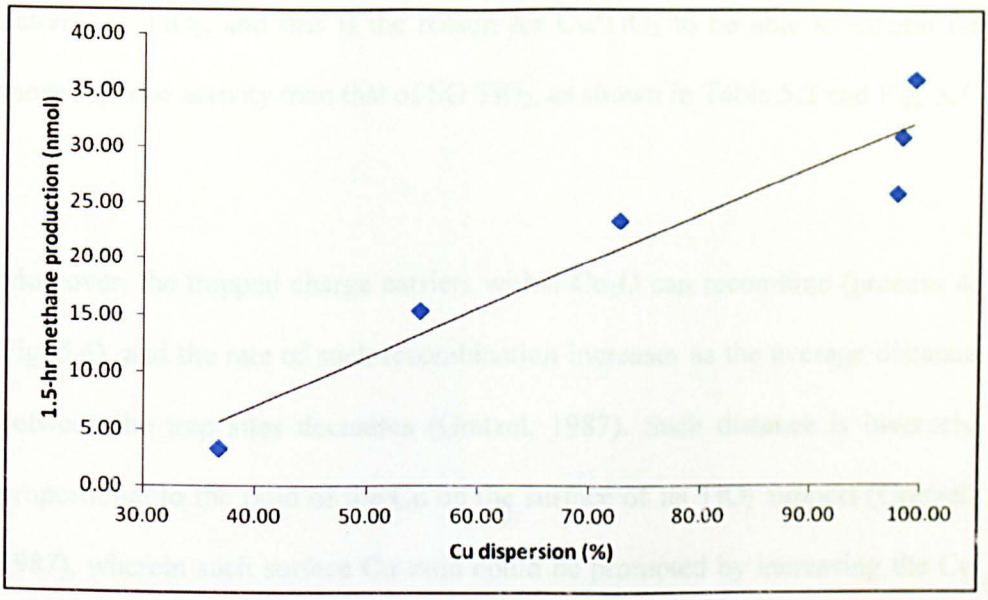

Fig. 5.3: Liner correlation between 1.5-hr methane production and Cu dispersion of Cu/TiO_2.

In agreement with the experimental results and the related discussions presented previously in this section, the possible mechanism of how the added Cu affected the activity of Cu/TiO_2 is proposed here (Fig. 5.4). First of all, the TiO_2 support of Cu/TiO_2 was activated by UVA light, and generated electrons and holes (process 1, Fig. 5.4). Then such charge carriers were trapped by the added Cu, which was at the chemical state of Cu_2O. This is because the relative positions of the CB and VB of TiO_2, compared to those of Cu_2O, make the photo-generated electrons and holes from TiO_2 favourable to transfer to Cu_2O (processes 2 and 3, Fig. 5.4) (Linsebigler et al., 1995). The charge carrier exchange between TiO_2 and Cu_2O is able to not only enhance the separation of the photo-generated electrons and holes derived from TiO_2, but also allows the added Cu to act as the active site on the surface of TiO_2 for CO_2 photoreduction. Both of these two effects favour the enhancement of the

activity of TiO_2, and this is the reason for Cu/TiO_2 to be able to exhibit far more superior activity than that of SG TiO_2, as shown in Table 5.2 and Fig. 5.1.

Moreover, the trapped charge carriers within Cu_2O can recombine (process 4, Fig. 5.4), and the rate of such recombination increases as the average distance between the trap sites decreases (Gratzel, 1987). Such distance is inversely proportional to the ratio of the Cu on the surface of its TiO_2 support (Gratzel, 1987), wherein such surface Cu ratio could be promoted by increasing the Cu ratio of Cu/TiO_2 (as proven by XPS, Table 4.9, Section 4.2.3.5). Therefore, the increase of the Cu ratio could promote the recombination rate of the trapped electrons and holes within the added Cu. Furthermore, when the aggregation of the added Cu occurred due to the over-increase (exceeded 0.03 wt%) of the Cu ratio, the specific surface area of the added Cu decreased (Fig. 5.2). This indicates that the over-increase of the Cu ratio could not only facilitate the recombination rate of the charge carriers trapped by the added Cu, but also reduce the Cu active sites on the surface of Cu/TiO_2. Therefore, the decrease of the activity of Cu/TiO_2 for methane production was observed when the Cu ratio exceeded 0.03 wt%, as shown in Table 5.2 and Fig. 5.1.

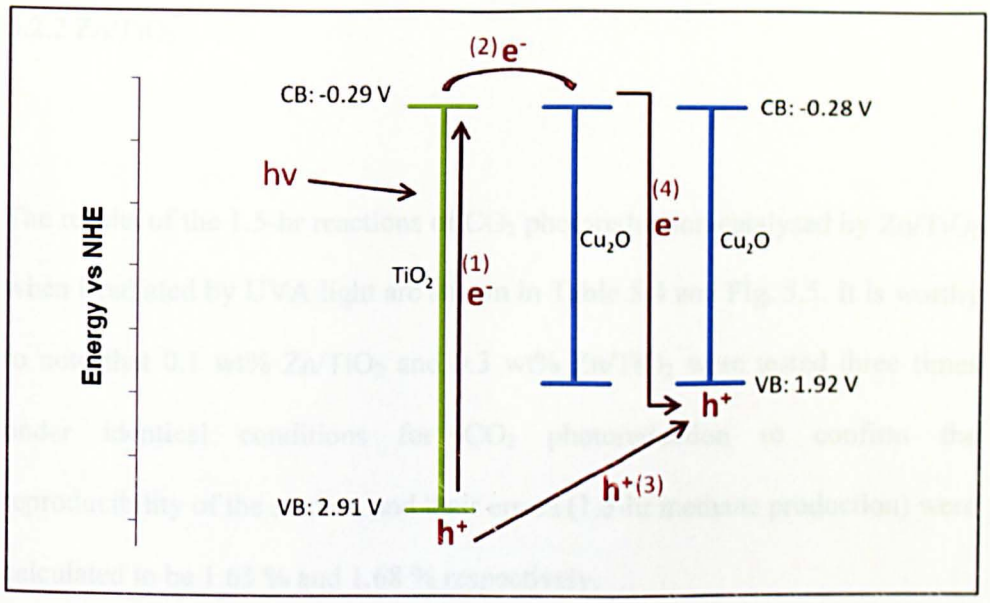

Fig. 5.4: Possible mechanism of the transfer process of the charge carriers within Cu/TiO_2. The data of CB and VB positions were obtained from Xu and Schoonen (2000).

In conclusion, the activity of TiO_2 for CO_2 photoreduction to methane could be significantly enhanced by the added Cu, loaded on the surface of TiO_2. This is because such added Cu was able to act as the charge carrier trap and active site on the surface of TiO_2, due to its relative CB and VB positions in contrast to those of TiO_2. However, the activity of Cu/TiO_2 started to decrease when its Cu ratio was over-increased. This is because such over-increase of the Cu ratio could promote of the recombination rate of the trapped charge carriers, and initiate Cu aggregation that could reduce the Cu active sites on the surface of TiO_2.

5.2.2 Zn/TiO_2

The results of the 1.5-hr reactions of CO_2 photoreduction catalysed by Zn/TiO_2 when irradiated by UVA light are shown in Table 5.4 and Fig. 5.5. It is worthy to note that 0.1 wt% Zn/TiO_2 and 0.3 wt% Zn/TiO_2 were tested three times under identical conditions for CO_2 photoreduction to confirm the reproducibility of the studies, and their errors (1.5-hr methane production) were calculated to be 1.65 % and 1.68 % respectively.

Table 5.4: Results of the 1.5-hr reactions of CO_2 photoreduction catalysed via Zn/TiO_2.

Catalyst	1.5-hr methane production (nmol)	Quantum efficiency (10^{-4} %)	Conversion of CO_2 (10^{-5} %)
SG TiO_2	3.10	3.25	2.42
0.05 wt% Zn/TiO_2	3.08	3.22	2.41
0.07 wt% Zn/TiO_2	3.13	3.28	2.45
0.1 wt% Zn/TiO_2	3.03	3.17	2.37
0.3 wt% Zn/TiO_2	2.98	3.12	2.33
0.5 wt% Zn/TiO_2	3.18	3.33	2.48

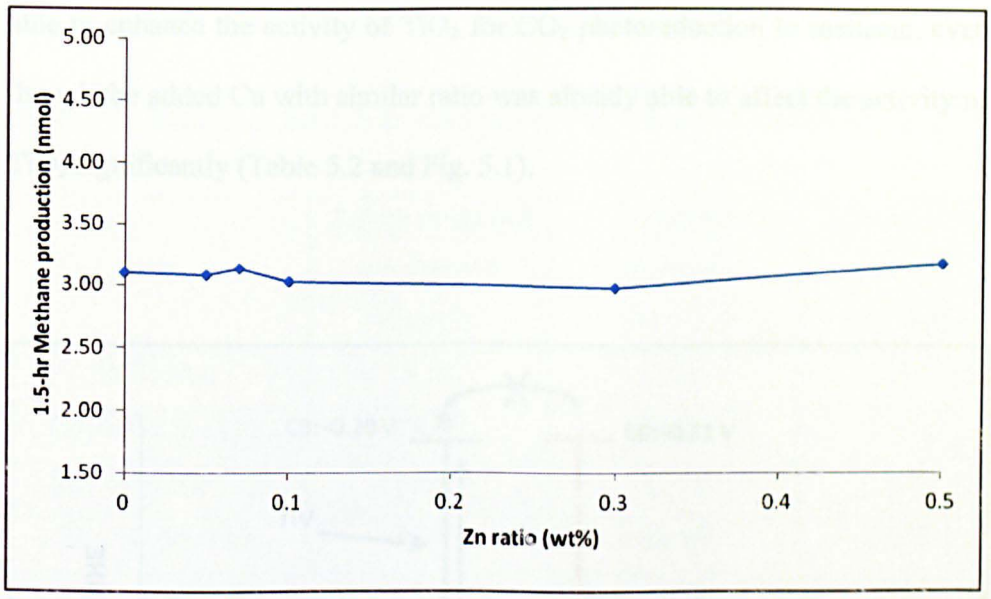

Fig. 5.5: 1.5-hr methane production from CO_2 photoreduction by using Zn/TiO_2 as catalyst.

It can be seen in Table 5.4 and Fig. 5.5 that the presence of the added Zn was not able to significantly (neither positively nor negatively) affect the activity of TiO_2 (in contrast to Cu/TiO_2, Fig. 5.1). The activity of all Zn/TiO_2 catalysts (regardless the Zn ratio) for methane production were similar to that of SG TiO_2. Such phenomenon should be attributed to the band-structure of the added Zn of Zn/TiO_2. It was shown by powder XRD and XPS studies (Sections 4.2.2.4 and 4.2.3.4) that the added Zn was located on the surface of the TiO_2 support with its chemical state to be ZnO. The band-structures of TiO_2 and ZnO are schematically shown in Fig. 5.6. It can be seen that the CB position of TiO_2 is relatively lower than that of ZnO. Therefore, the photo-generated electrons from TiO_2 were not favourable to transfer to the CB of ZnO. Consequently, the added Zn of Zn/TiO_2 is not able to act as the electron trap. Hence, the presence of the added Zn, with the ratio of 0.05-0.5 wt%, was not

able to enhance the activity of TiO_2 for CO_2 photoreduction to methane, even though the added Cu with similar ratio was already able to affect the activity of TiO_2 significantly (Table 5.2 and Fig. 5.1).

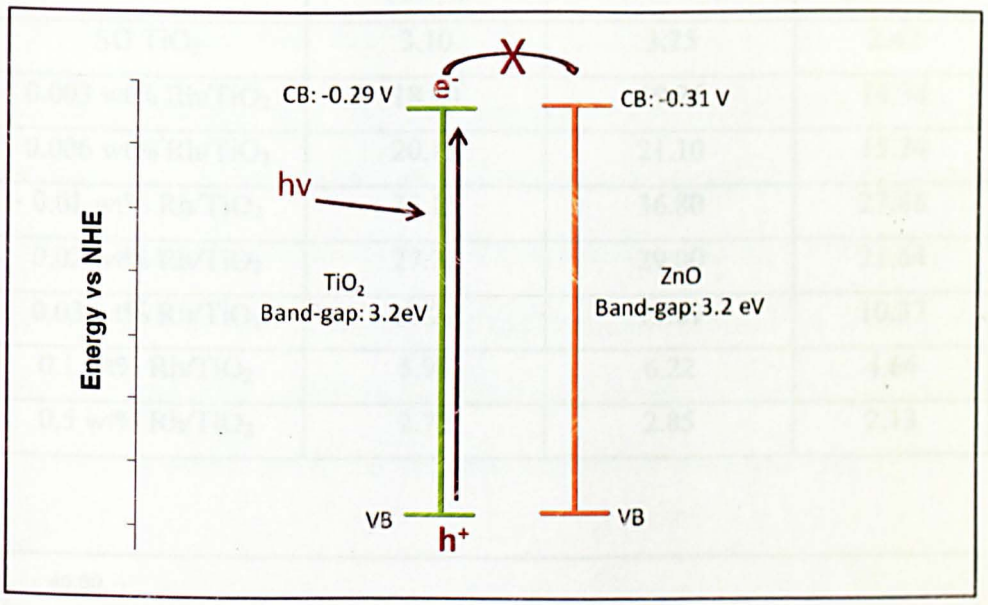

Fig. 5.6: Possible mechanism of the transfer process of the charge carriers within Zn/TiO_2. The data of CB and VB positions were obtained from Xu and Schoonen (2000).

5.2.3 Rh/TiO_2

The results of 1.5-hr reactions of CO_2 photoreduction catalysed via Rh/TiO_2 when irradiated by UVA light are shown in Table 5.5 and Fig. 5.7. The optimal Rh/TiO_2 (0.01 wt% Rh/TiO_2) was tested three times under identical conditions for CO_2 photoreduction to confirm the reproducibility of the studies, wherein the error (1.5-hr methane production) was calculated to be 1.60 %.

Table 5.5: Results of the 1.5-hr reactions of CO_2 photoreduction catalysed via Rh/TiO_2.

Catalyst	1.5-hr methane production (nmol)	Quantum efficiency (10^{-4} %)	Conversion of CO_2 (10^{-5} %)
SG TiO_2	3.10	3.25	2.42
0.003 wt% Rh/TiO_2	18.40	19.26	14.38
0.006 wt% Rh/TiO_2	20.15	21.10	15.74
0.01 wt% Rh/TiO_2	35.15	36.80	27.46
0.02 wt% Rh/TiO_2	27.70	29.00	21.64
0.03 wt% Rh/TiO_2	13.27	13.89	10.37
0.1 wt% Rh/TiO_2	5.94	6.22	4.64
0.5 wt% Rh/TiO_2	2.72	2.85	2.13

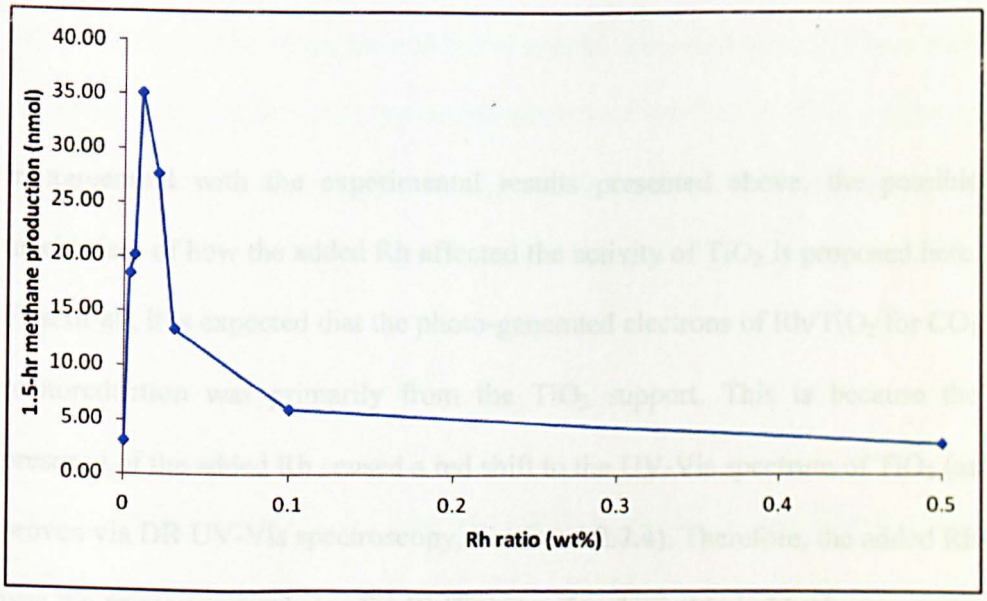

Fig. 5.7: 1.5-hr methane production from CO_2 photoreduction by using Rh/TiO_2 as catalyst.

It can be seen in Table 5.5 and Fig. 5.7 that the Rh ratio could significantly affect the activity of Rh/TiO_2 for methane production. The activity of Rh/TiO_2 increased as the Rh ratio increased within the range of 0-0.01 wt%. The presence of the added Rh was able to significantly enhance the activity of TiO_2, wherein the methane production of the best-performing 0.01 wt% Rh/TiO_2 was 1033.87 % higher than that of SG TiO_2. However, as the Rh ratio over-increased (exceeded 0.01 wt%), the activity of Rh/TiO_2 started to decrease. Furthermore, an alternative CO_2 photoreduction experiment irradiated by visible light was conducted by using the optimal Rh/TiO_2 (0.01 wt% Rh/TiO_2) as catalyst. The result indicates that such catalyst presented no activity for methane production under visible light, even though it was able to exhibit significantly better activity for the same experiment when irradiated by UVA light.

In agreement with the experimental results presented above, the possible mechanism of how the added Rh affected the activity of TiO_2 is proposed here. First of all, it is expected that the photo-generated electrons of Rh/TiO_2 for CO_2 photoreduction was primarily from the TiO_2 support. This is because the presence of the added Rh caused a red shift to the UV-Vis spectrum of TiO_2 (as proven via DR UV-Vis spectroscopy, Section 4.2.7.4). Therefore, the added Rh was the primary contributor for Rh/TiO_2 to absorb visible light. However, the poor performance of 0.01 wt% Rh/TiO_2 when irradiated by visible light indicates that such absorption of visible light by the added Rh was not able to generate effective electrons to induce CO_2 photoreduction. In contrast, the significantly more superior performance of the same catalysts when irradiated

by UVA light confirms that the TiO_2 support of Rh/TiO_2, which could only be effectively activated by UVA light, was the primary contributor for the photo-generated electrons to initiate CO_2 photoreduction to methane.

Meanwhile, the results shown in Table 5.5 and Fig. 5.7 indicate that the presence of the added Rh was able to greatly enhance the activity of TiO_2. This is because the added Rh was substitutionally doped into the lattice of the surface of its TiO_2 support with its chemical state to be Rh^{3+} (as proven via powder XRD and XPS, Sections 4.2.2.3 and 4.2.3.3). Such doping was able to introduce additional energy level into the band-gap of TiO_2 (as shown in Section 2.3.1.2; Choi et al., 1994). Moreover, the redox potential (NHE) of Rh^{3+}/Rh^{2+} is 0.158 V (Kitano et al., 2011), which lies below the CB position of TiO_2 (-0.29 V). Therefore, the additional energy level introduced by the added Rh was able to trap the photo-generated electrons from the CB of TiO_2 (Choi et al., 1994). Such phenomenon could improve the separation of the electrons and holes derived from TiO_2, and enhance the activity of TiO_2 for CO_2 photoreduction.

Finally, Table 5.5 and Fig. 5.7 also show that the activity of Rh/TiO_2 could be decreased via the over-increase of the Rh ratio. This is because the additional energy level introduced by the added Rh could also act as the charge carrier recombination center, which facilitate the recombination rate of the photo-generated electrons and holes derive from TiO_2 (as shown in Section 2.3.1.2; Choi et al., 1994). Therefore, the presence of the added Rh could have both

positive and negative effects on the activity of TiO_2. There was an optimal Rh ratio that could achieve the balance of such two opposite effects and optimize the activity of Rh/TiO_2. Such Rh ratio was presented as 0.01 wt% in Table 5.5 and Fig. 5.7. Hence, when the Rh ratio exceeded 0.01 wt%, the activity of Rh/TiO_2 started to decrease.

It can be therefore concluded that the activity of TiO_2 for CO_2 photoreduction to methane could be significantly enhanced by the added Rh, which was doped into the lattice of TiO_2. This is because such added Rh was able to introduce an additional energy level to the band-gap of TiO_2, which could act as the electron trap to improve the charge carrier separation. Meanwhile, the activity of the Rh/TiO_2 was found to be decreased via the over-increase of the Rh ratio. This is because the additional energy level introduced by the added Rh could also act as the recombination center. Therefore, the presence of the excessive amount of the added Rh could facilitate the recombination rate of the charge carrier and decrease the activity of Rh/TiO_2.

5.2.4 $Rh/Cu/TiO_2$

It has been reported in Sections 5.2.1 and 5.2.3 that both Cu and Rh were able to improve the activity of TiO_2 in this study, even though they modified their TiO_2 supports on different ways. The added Cu was loaded on the surface of TiO_2 as Cu_2O, and the added Rh was doped to the lattice of TiO_2 with its

chemical state to be Rh^{3+}. Moreover, Section 5.2.1 presented that the aggregation of the added Cu induced via the over-increase (over 0.03 wt%) of the Cu ratio was one of the primary reasons to limit the activity of Cu/TiO_2 for CO_2 photoreduction. To further improve the activity of Cu/TiO_2, certain amount of additional Rh was doped into the optimal Cu/TiO_2 (0.03 wt% Cu/TiO_2). Because the additional Rh dopant was doped into the lattice rather than loaded on the surface of TiO_2, it was expected that such additional Rh dopant would not induce the Cu aggregation, but synergistically further improve the activity of 0.03 wt% Cu/TiO_2.

The TiO_2 simultaneously modified by Rh and Cu is referred as $Rh/Cu/TiO_2$ in this study. Such catalysts were also synthesized via the sol-gel process described in Section 3.1. The Cu ratio of $Rh/Cu/TiO_2$ was maintained to be 0.03 wt%; which has been reported in Section 5.2.1 to be the optimal for Cu/TiO_2, and did not induce the Cu aggregation. On the other hand, the ratio of Rh of $Rh/Cu/TiO_2$ was varied within the range of 0.003-0.02 wt% in order to find out the optimal ratio of the additional Rh. The synthesized $Rh/Cu/TiO_2$ were tested for 1.5-hr reactions of CO_2 photoreduction when irradiated by UVA light. The results of these experiments are shown in Table 5.6 and Fig. 5.8. It is worthy to note that the optimal $Rh/Cu/TiO_2$ (0.006 wt% Rh/0.03 wt% Cu/TiO_2) was tested three times under identical conditions for CO_2 photoreduction to confirm the reproducibility of the studies, and the error (1.5-hr methane production) was 2.13 %.

Table 5.6: Results of the 1.5-hr reactions of CO_2 photoreduction catalysed via Rh/TiO_2, Cu/TiO_2, and $Rh/Cu/TiO_2$.

Catalyst	1.5-hr methane production (nmol)	Quantum efficiency (10^{-4} %)	Conversion of CO_2 (10^{-5} %)
0.006 wt% Rh/TiO_2	20.15	21.10	15.74
0.01 wt% Rh/TiO_2	35.15	36.80	27.46
0.03 wt% Cu/TiO_2	36.11	37.81	28.21
0.003 wt% Rh/0.03 wt% Cu/TiO_2	37.05	38.79	28.95
0.006 wt% Rh/0.03 wt% Cu/TiO_2	45.57	47.71	35.60
0.01 wt% Rh/0.03 wt% Cu/TiO_2	28.91	30.27	22.59
0.02 wt% Rh/0.03 wt% Cu/TiO_2	24.83	26.00	19.40

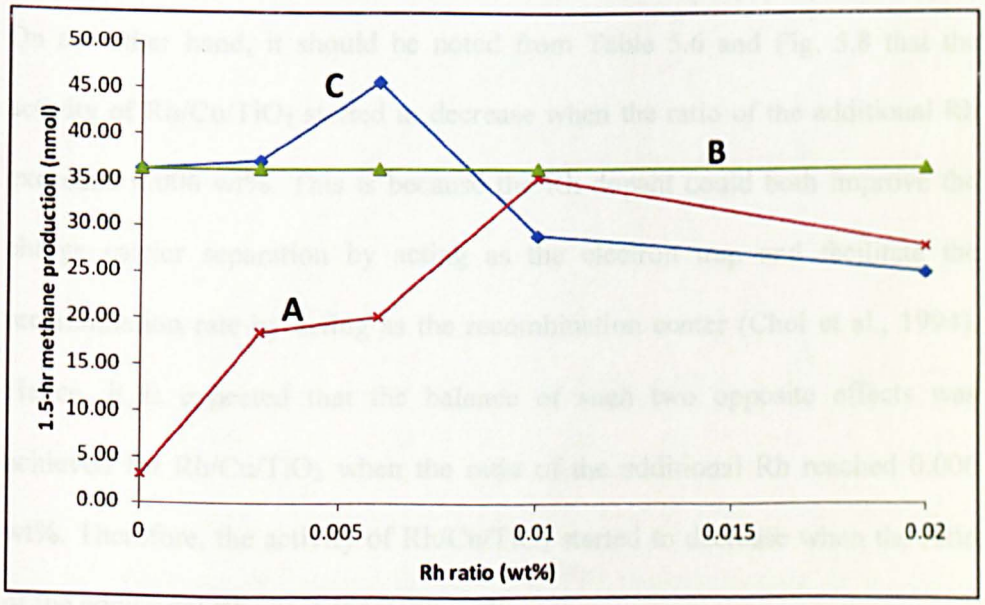

Fig. 5.8: 1.5-hr methane productions from CO_2 photoreduction by using A: Rh/TiO_2, B: 0.03 wt% Cu/TiO_2, and C: $Rh/Cu/TiO_2$ as catalysts.

It can be seen in Table 5.6 and Fig. 5.8, that the additional Rh doping was indeed able to further improve the activity of 0.03 wt% Cu/TiO_2. The methane production of the best-performing 0.06 wt% Rh/0.03 wt% Cu/TiO_2 was 26.20 % and 29.64 % higher than those of the optimal Cu/TiO_2 (0.03 wt% Cu/TiO_2) and Rh/TiO_2 (0.01 wt% Rh/TiO_2), respectively. It is expected that this is because the additional Rh was doped into the lattice rather than being loaded on the surface of TiO_2. Hence such additional Rh did not affect the dispersion of the original 0.03 wt% added Cu that was loaded on the surface of TiO_2. Therefore, the additional Rh and the original 0.03 wt% Cu were able to synergistically enhance the activity of TiO_2. Such phenomenon made $Rh/Cu/TiO_2$ able to exhibit better activity than any of the Cu/TiO_2 or Rh/TiO_2 catalysts.

On the other hand, it should be noted from Table 5.6 and Fig. 5.8 that the activity of $Rh/Cu/TiO_2$ started to decrease when the ratio of the additional Rh exceeded 0.006 wt%. This is because the Rh dopant could both improve the charge carrier separation by acting as the electron trap and facilitate the recombination rate by acting as the recombination center (Choi et al., 1994). Hence, it is expected that the balance of such two opposite effects was achieved for $Rh/Cu/TiO_2$ when the ratio of the additional Rh reached 0.006 wt%. Therefore, the activity of $Rh/Cu/TiO_2$ started to decrease when the ratio of the additional Rh exceeded 0.006 wt%.

5.3 Experiments of 4.5-hr CO_2 photoreduction

The optimal M/TiO_2 (0.01 wt% Rh/TiO_2, 0.03 wt% Cu/TiO_2, 0.006 wt% Rh/0.03 wt% Cu/TiO_2) and SG TiO_2 were tested for 4.5-hr CO_2 photoreduction experiments irradiated by UVA light. The quantities of methane produced during the experiments were analysed periodically. Fig. 5.9 shows the methane productions during such 4.5-hr experiments, and the maximum quantities of the methane produced during these experiments are listed in Table 5.7, which were used to calculate the turnover numbers (TON) of the tested catalysts.

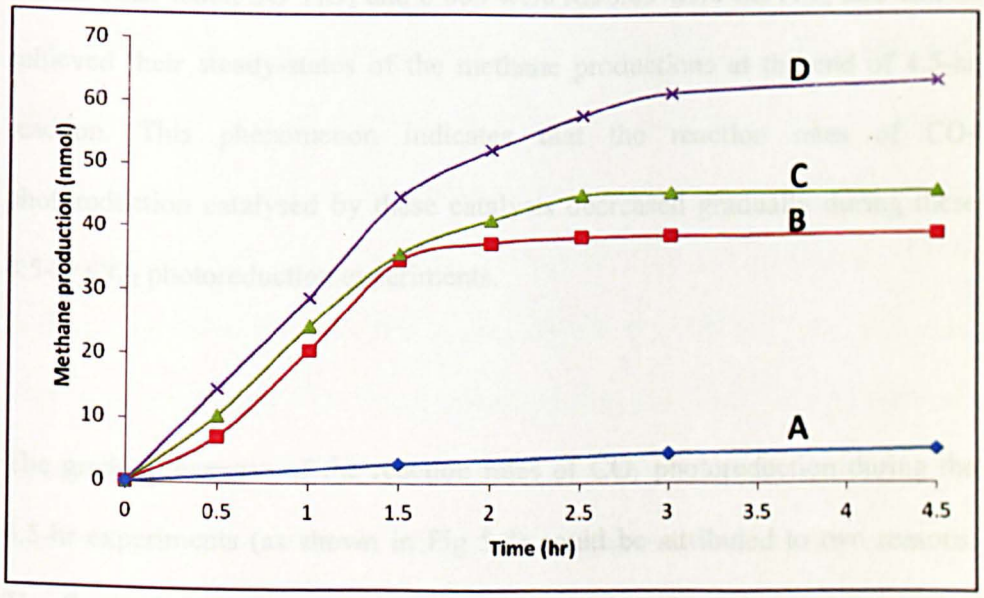

Fig. 5.9: Methane productions during 4.5-hr CO_2 photoreduction. A: SG TiO_2, B: 0.01 wt% Rh/TiO_2, C: 0.03 wt% Cu/TiO_2, D: 0.006 wt% Rh/0.03 wt% Cu/TiO_2.

Table 5.7: TONs of the catalysts.

Catalyst	Maximum quantity of methane produced (nmol)	TON
SG TiO_2	5.24	4.19×10^{-10}
0.01 wt% Rh/TiO_2	39.15	31.32×10^{-10}
0.03 wt% Cu/TiO_2	45.89	36.71×10^{-10}
0.006 wt% Rh/0.03 wt% Cu/TiO_2	63.42	50.74×10^{-10}

TON was defined as the ratio between the maximum quantity (mole) of the methane produced to the quantity (mole) of catalyst.

It can be seen in Fig. 5.9 that 0.01 wt% Rh/TiO_2 and 0.03 wt% Cu/TiO_2 achieved the steady-states of their methane productions after 2.5-hr reaction. On the other hand, SG TiO_2 and 0.006 wt% Rh/0.03 wt% Cu/TiO_2 also almost achieved their steady-states of the methane productions at the end of 4.5-hr reaction. This phenomenon indicates that the reaction rates of CO_2 photoreduction catalysed by these catalysts decreased gradually during these 4.5-hr CO_2 photoreduction experiments.

The gradual decrease of the reaction rates of CO_2 photoreduction during the 4.5-hr experiments (as shown in Fig 5.8) could be attributed to two reasons. The first reason is that the reaction of CO_2 photoreduction was approaching equilibrium. This is because the organic products generated via CO_2 photoreduction (e.g. methane) could be re-oxidized by the photo-generated holes within TiO_2 (Halmann et al., 1983). Therefore, the quantity of the methane produced via CO_2 photoreduction can stop increasing when the reactions of the photoreduction and re-oxidation achieve equilibrium. The

second reason for the decrease of the reaction rate can be the deactivation of the catalysts due the loss of the active sites (Tseng et al., 2002).

In this work, the decrease of the reaction rate of CO_2 photoreduction is expected not to be solely due to the equilibrium of the reaction. The deactivation of the catalyst due to the loss of the active sites should be another contributor for such phenomenon. Fig. 5.10 shows the colours of the catalysts before and after 4.5-hr CO_2 photoreduction experiments. It can be seen that the colours of these catalysts were darkened at the end of the 4.5-hr experiments. Such phenomenon has been reported to be due to the photoinduced surface corrosion of TiO_2 (Linsebigler et. al., 1995; Kajeshwar et. al., 1978; Nakajima et al., 2001). This is because, when TiO_2 is irradiated by UV light with high intensity, excessive charge carriers can be generated. If such charge carriers are not removed in time (e.g. by recombination or participanting photocatalytic reactions), they will decompose the surface of TiO_2 (Shapira et al., 1976). Furthermore, the data of the XPS analysis for the 0.5 wt% Cu/TiO_2 before and after being irradiated by UVA light for 4.5-hr (Fig. 5.11 and Table 5.8) indicate that, although the chemical state of the added Cu did not change by UVA irradiation, the Cu ratio on the surface of TiO_2 decreased after being irradiated by UVA light for 4.5-hr. This phenomenon indicates that the photoinduced surface corrosion could also decompose the added Cu, wherein such Cu has been proven to be the active sites on the surface of Cu/TiO_2 for CO_2 photoreduction (Section 5.2.1).

Therefore, it can be concluded that the deactivation of the TiO_2 catalyst caused by the surface corrosion induced via UVA irradiation was also a contributor for the decrease of the reaction rate during the 4.5-hr CO_2 photoreduction experiment (as well as the reaction was approaching equilibrium). Nevertheless, such problem can be greatly mitigated if visible light could take the place of UV light for the excitation of TiO_2 (proposed as a further work, Section 6.2.2).

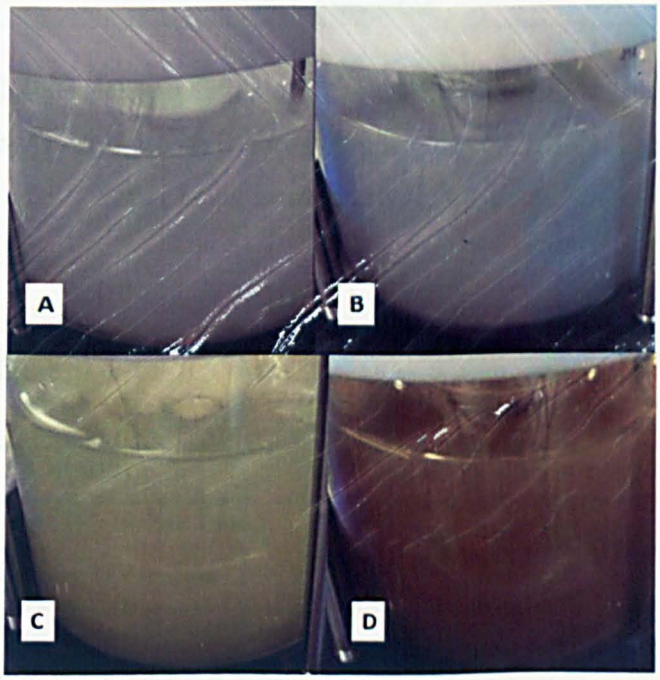

Fig. 5.10: Colours of SG TiO_2 and 0.03 wt% Cu/TiO_2 during 4.5-hr CO_2 photoreduction experiments irradiated by UVA light. A: SG TiO_2 before experiment started, B: SG TiO_2 after the 4.5-hr experiment, C: 0.03 wt% Cu/TiO_2 before experiment started, D: 0.03 wt% Cu/TiO_2 after the 4.5-hr experiment.

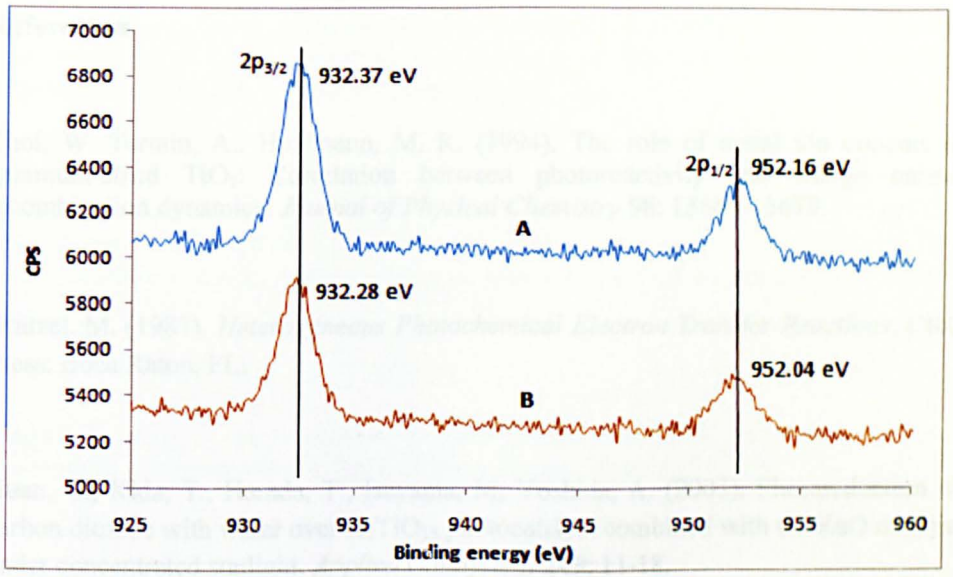

Fig. 5.11: XPS spectra of Cu 2p of 0.5 wt% Cu/TiO_2 before and after being irradiated by UVA light. A: Before being irradiated by UVA light, B: 4.5-hr after being irradiated by UVA light.

Table 5.8: Cu ratios of 0.5 wt% Cu/TiO_2 before and after 4.5-hr UVA irradiation.

Catalyst	Elemental ratio measured by XPS
0.5 wt% Cu/TiO_2 before being irradiated by UVA light.	1.31 wt% Cu/TiO_2
0.5 wt% Cu/TiO_2 after being irradiated by UVA light for 4.5-hr.	0.76 wt% Cu/TiO_2

References

Choi, W. Termin, A., Hoffmann, M. R. (1994). The role of metal ion dopants in Quantum-sized TiO_2: Correlation between photoreactivity and charge carrier recombination dynamics. *Journal of Physical Chemistry* **98**: 13669-13679.

Gratzel, M. (1987). *Heterogeneous Photochemical Electron Transfer Reactions*. CRC Press: Boca Raton, FL.

Guan, G., Kida, T., Harada, T., Isayama, M, Yoshida, A. (2003). Photoreduction of carbon dioxide with water over K_2TiO_{13} photocatalyst combined with Cu/ZnO catalyst under concentrated sunlight. *Applied Catalysis A* **249**: 11-18.

Halmann, M. (1983). *Photochemical fixation of carbon dioxide, energy resource through photochemistry and catalysis*. Academic Press, New York.

Jung, K. Y., Park, S. B. (2000). Park, Enhanced photoactivity of silica-embedded titania particles prepared by sol-gel process for the decomposition of trichloroethylene. *Applied Catalysis B* **25**: 249-256.

Koci, K., Obalova, L., Matejova, L., Placha, D., Lacny, Z., Jirkovsky, J., Solcova, O. (2009). Effect of TiO_2 particle size on the photocatalytic reduction of CO_2, *Applied Catalysis B* **89**: 494-502.

Kajeshwar, K., Singh, P., DuBow, J. (1978). Energy conversion in photoelectrochemical systems-a review. *Electrochimica Acta* **23**: 1117.

Kitano, S., Hashimoto, K., Kominami, H. (2011) Photocatalytic mineralization of volatile organic compounds over commercial titanium (IV) oxide modied with rhodium (III) ion under visible light irradiation and correlation between physical properties and photocatalytic activity and correlation between physical properties and photocatalytic activity. *Catalysis Today* **164**: 404-409.

Linsebigler, A. L., Lu, G., Yates, J. T. (1995). Photocatalysis on TiO_2 surface: principles, mechanisms, and selected results. *Chemical Reviews* **95**: 735-758.

Nakajima, A., Koizumi, S., Watanabe, T., Hashimoto, K. (2001). Effect of repeated photo-illumination on the wettability conversion of titanium dioxide. *Journal of Photochemistry and Photobiology A* **146**: 129-132.

Serpone, N., Lawless, D., Khairlutdinov, R., Pelizzetti, E. (1995). Size effects on the photophysical properties of colloidal anatase TiO_2 particles: Size quantization versus direct transitions in this indirect semiconductor? *Journal of Physical Chemistry* **99**: 16655.

Shapira, Y., Cox, S. M., Lichtman, D. (1976). Chemisorption, Photodesorption and conductivity measurements on ZnO surfaces. *Surface Science* **54**: 43.

Tseng, I. H., Chang, W. C., Wu, J. C. S. (2002). Photoreduction of CO_2 using sol-gel derived titania and titania-supported copper catalysts. *Applied Catalysis B* **37**: 37-48.

Tian, G. H., Fu, H. G., Jing, L. Q., Xin, B. F., Pan, K. (2008). Preparation and characterization of stable biphase TiO_2 photocatalyst with high crystallinity, large surface area, and enhanced photoactivity. *Journal of Physical Chemistry C* **112**: 3083-3089.

Xu, Y., Schoonen, M. A. A. (2000). The absolute energy positions of conduction and valence bands of selected semiconducting minerals. *American Mineralogist* **85**: 543-556.

Chapter 6: Conclusions and recommended further works

The results and related discussions derived from this work have been reported in Chapters 4 and 5. This chapter presents the summary of the conclusions, and recommends the further works that are worthy to be conducted in future.

6.1 Conclusions

This work aimed to study the effects of metal modification on TiO_2 for CO_2 photoreduction. The primary results were derived from catalysts synthesis and characterization, and CO_2 photoreduction experiments. This section summarised the conclusions of these studies.

6.1.1 Catalyst synthesis and characterization

Pure and metal modifiedTiO_2 (referred as SG TiO_2 and M/TiO_2, respectively) had been synthesized via sol-gel process in this work. The adopted sol-gel process for such catalyst synthesis was developed by Wu et al. (Wu and Yeh, 2001; Wu et al., 2001). The metals chosen to modify TiO_2 included Cu, Zn, and Rh. **Compared to the previous studies that only reported the nominal elemental ratios of their metal modified TiO_2 catalysts (e.g. Wu and Yeh, 2001; Wu et al., 2001; Tseng et al., 2002 and 2004), this work confirmed**

the actual elemental ratios of M/TiO_2 by using inductively coupled plasma mass spectrometry (ICP-MS). To dissolve these TiO_2 catalysts for ICP-MS analysis, hot sulphuric acid was used as the solvent (as described in Section 3.2.3). The result of ICP-MS analysis confirmed that the actual elemental ratios of M/TiO_2 synthesized in this work was consistent with their nominal elemental ratios (Section 4.2.1).

The further catalyst characterization determined that all the sol-gel derived TiO_2 in this work had the same anatase crystalline phase (Section 4.2.2), and similar particle sizes (11-16 nm, Section 4.2.4) and surface areas (50.24-63.37 m^2/g, Section 4.2.5). **Importantly, compared to the previous studies that did not conclusively prove whether the added metal was doped or loaded to the sol-gel derived metal modified TiO_2 (Kohno et al., 1999; Tseng et al., 2004; Colon et al., 2006), this work used powder X-ray diffraction (powder XRD, Section 4.2.2) and X-ray photoelectron spectroscopy (XPS, Section 4.2.3) to identify how the added metals modified their TiO_2 supports.** The results show that, even though synthesized via the same sol-gel process, the added metals could modify their TiO_2 supports differently. The added Cu and Zn were loaded to the surfaces of their TiO_2 supports with their chemical states to be Cu_2O and ZnO, respectively. On the other hand, the added Rh was substitutionally doped into the lattice of its TiO_2 support with its chemical state to be Rh^{3+}. Such phenomenon was attributed to the different ionic sizes of Cu^{1+} (91 pm), Zn^{2+} (88 pm), Rh^{3+} (80.5 pm), and Ti^{4+} (74.5 pm); wherein the ionic sizes of Cu^{1+} and Zn^{2+} were too large for substitutional doping to TiO_2 lattice,

but the ionic size of Rh^{3+} was favourable for such doping (Shannon, 1976, Barrett and Massalski, 1980; Li et al., 2005).

Furthermore, the specific surface area and dispersion of the added Cu on the surface of Cu/TiO_2 were measured by using N_2O as adsorbate (Section 4.2.6). **Previous studies (Sakthivel et. al., 2004a; Madikizela-Mnqanqeni and Coville, 2008) have claimed that the added Cu was uniformly dispersed on the surface of TiO_2 when the powder XRD analysis showed poor detection for the added Cu. However, the measurement of the Cu dispersion in this work clearly indicated that significant aggregation of the added Cu on the surface of Cu/TiO_2 could have occurred even if such added Cu was still not detectable via powder XRD.**

6.1.2 CO_2 photoreduction experiments

The TiO_2 catalysts derived from the so-gel process in this work and an anatase reference (Acros Organics, 99%) were tested for CO_2 photoreduction. Although the sol-gel derived TiO_2 catalysts presented deactivation partially due to the photoinduced surface corrosion (Section 5.3), these catalysts were indeed able to successfully catalyse the reactions of CO_2 photoreduction to methane (Sections 5.1 and 5.2).

In contrast, the anatase reference showed no activity for catalysing the same reaction at all (Section 5.1). This is caused by the excessive large particle size (40-200 nm, Section 4.2.4) and poor surface area (7.93 m^2/g, Section 4.2.5) of the anatase reference. This result confirmed the conclusions of the previous studies (Zhang et al., 1998; Koci et al., 2009; Jung et al., 2000; Tian et al., 2008) that particle size and surface area can effectively affect the activity of TiO_2 for photocatalysis.

In addition, the results of CO_2 photoreduction experiments also confirmed that the added Cu and Rh were able to significantly enhance the activity of TiO_2 (as reported by Kohno et al., 1999; Tseng et al., 2004), whereas, the added Zn presented no effects for the same purpose. **Since this work has clearly shown how the added metals modify their TiO_2 supports (in contrast to previous studies, e.g. Kohno et al., 1999; Tseng et al., 2004), the possible mechanisms for these added metals to affect the activity of TiO_2 for CO_2 photoreduction were proposed (Sections 5.2.1 5.2.2, and 5.2.3).** The added Cu was proven to be loaded on the surface of TiO_2 with its chemical state to be Cu_2O. The combination of such added Cu and TiO_2 was considered to be a composite semiconductor catalyst, wherein the added Cu was able to improve the activity of TiO_2 via trapping the photogenerated electrons (e^-) due to its relatively lower conduction band position compared to that of TiO_2 (Xu and Schoonen, 2000). However, the over-increase of the Cu ratio could also decrease the activity of Cu/TiO_2. This is because such over-increase of the Cu ratio could promote the recombination rate of the trapped charge carriers, and initiate Cu aggregation that could reduce the Cu active sites on the surface of

TiO_2 for CO_2 photoreduction. In contrast, although the added Zn was also loaded on the surface of TiO_2, it was in the chemical state of ZnO, which has a conduction band position relatively higher than that of TiO_2 (Xu and Schoonen, 2000). Therefore, the added Zn was not favourable to trap the photo-generated electrons from TiO_2 and improve the activity of TiO_2 for CO_2 photoreduction. On the other hand, the added Rh was substitutionally doped into the lattice of its TiO_2 support with its chemical state to be Rh^{3+}. Such added Rh was able to introduce an additional energy level to the band-gap of TiO_2 (Choi et al., 1994), which could act as the electron trap to improve the activity of TiO_2. However, such additional energy level could also act as recombination center. Therefore, the presence of the excessive amount of the added Rh could also facilitate the recombination rate of the charge carrier and decrease the activity of Rh/TiO_2.

Finally, it was found that the additional Rh doping was able to further improve the activity of the best-performing Cu/TiO_2 (0.03 wt% Cu/TiO_2), wherein the activity of such double metal modified TiO_2 (Rh/Cu/TiO_2) was able to exhibit better activity than any of the Cu/TiO_2 or Rh/TiO_2 catalysts in this work (Section 5.2.4). It is expected that this was because the additional Rh was doped into the lattice of TiO_2, rather than being loaded on the surface of TiO_2. Hence, such additional Rh doping did not affect the dispersion of the original added Cu on the surface of TiO_2. Therefore, the additional Rh doping and the original Cu loading were able to synergistically enhance the activity of TiO_2, allowing the optimal Rh/Cu/TiO_2 (0.006 wt% Rh/0.03 wt% Cu/TiO_2) to present better activity than any of the Cu/TiO_2 or Rh/TiO_2.

6.2 Recommended further works

The future works worthy to be conducted are recommended in this section. They include the investigations on involving TiO_2 in mesoporous materials and doping TiO_2 with anions.

6.2.1 Involving TiO_2 in mesoporous materials

Involving TiO_2 in mesoporous material (e.g. silicate) had proven to be another promising method to improve the activity and selectivity of TiO_2 for CO_2 photoreduction (Anpo et al., 1998; Shioya et al., 2003; Li et al., 2010). However, the current reported studies are only sufficient to prove the higher activity of such mesoporous-material-supported TiO_2 comparing to the traditional powdered TiO_2. The understanding on the relation between the intricate properties of such mesoporous catalyst (e.g. optimal pore size) and its activity for CO_2 photoreduction is still not comprehensive. Therefore, it is worthy to conduct more investigations in this field.

6.2.2 Doping TiO_2 with anions

As described in Section 2.3, the primary problems for TiO_2 to be a practical catalyst for CO_2 photoreduction are its relatively low activity and poor

photocatalytic performance under visible light. This work has focused on the improvement of the activity of TiO_2. It is also worthy to work on improving the photocatalytic performance of TiO_2 for CO_2 photoreduction under visible light. Doping TiO_2 with anions (e.g. N, S, C) had been proven to be an effective method to enhance the activity of TiO_2 under visible light (Asahi et al., 2001; Sakthivel et al., 2004b; Ho et al., 2006; Lin et al., 2011). However, only limited investigations had been conducted for the use of such anion doped TiO_2 to photoreduce CO_2 under visible light (Varghese et al., 2009). Therefore, further study on this field is encouraged.

References

Anpo, M., Yamashita, H., Ikeue, K., Fujii, Y., Zhang, S. G., Ichihashi, Y., Park, D. R., Suzuki, Y., Koyano, K., Tatsumi, T. (1998) Photocatalytic reduction of CO_2 with H_2O on Ti-MCM-41 and Ti-MCM-48 mesoporous zeolite catalysts. *Catalysis Today* **44**: 327-332.

Asahi, R., Morikawa, T., Ohwaki, T., Aoki, K., Taga, Y. (2001). Visible-light photocatalysis in nitrogen-doped titanium oxides. *Science* **293**: 269.

Barrett, C. S., Massalski, T. B. (1980). *Structure of metals, 3rd ed.* Pergamon Press. Oxford, New York, Ontario, Potts Point, Paris, and Hammerweg.

Colon, G., Maicu, M., Hidalgo, M. C., Navio, J. A. (2006). Cu-doped TiO_2 systems with improved photocatalytic activity. *Applied Catalysis B* **67**: 41-51.

Choi, W. Termin, A., Hoffmann, M. R. (1994). The role of metal ion dopants in Quantum-sized TiO_2: Correlation between photoreactivity and charge carrier recombination dynamics. *Journal of Physical Chemistry* **98**: 13669-13679.

Ho, W., Yu, J. C., Lee, S. (2006). Low-temperature hydrothermal synthesis of S-doped TiO_2 with visible light photocatalytic activity. *Journal of Solid State Chemistry* **179**: 1171-1176.

Jung, K. Y., Park, S. B. (2000). Park, Enhanced photoactivity of silica-embedded titania particles prepared by sol-gel process for the decomposition of trichloroethylene. *Applied Catalysis B* **25**: 249-256.

Koci, K., Obalova, L., Matejova, L., Placha, D., Lacny, Z., Jirkovsky, J., Solcova, O. (2009). Effect of TiO_2 particle size on the photocatalytic reduction of CO_2, *Applied Catalysis B* **89**: 494-502.

Kohno, Y., Hayashi, H., Takenaka, S., Tanaka, T., Funabiki, T. (1999). Photo-enhanced reduction of carbon dioxide with hydrogen over Rh/TiO_2. *Journal of Photochemistry and Photobiology A* **126**: 117-123.

Li, W., Frenkel, A. I., Woicik, J. C., Ni, C., Ismat Shah, S. (2005). Dopant location identification in Nd^{3+}-doped TiO_2 nanoparticles. *Physical Review B* **72**: 155315.

Li, Y., Wang, W. N., Zhan, Z., Woo, M. H., Wu, C. Y., Biswas, P. (2010). Photocatalytic reduction of CO_2 with H_2O on mesoporous silica supported Cu/TiO_2 catalysts. *Applied Catalysis B* **100**: 386-392.

Lin, X., Rong, F., Ji, X., Fu, D. (2011). Carbon-doped mesoporous TiO_2 film and its photocatalytic activity. *Microporous and Mesoporous Materials* **142**: 276-281.

Madikizela-Mnqanqeni, N. N., Coville, N. J. (2008). The effect of sulphur addition during the preparation of $Co/Zn/TiO_2$ Fischer-Tropsch catalyst. *Applied Catalysis A* **340**: 7-15.

Shannon, R. D. (1976). Revised effective ionic radii and systematic studies of interatomic distances in halides and chalcogenides. *Acta Crystallographica A* **32**: 751.

Sakthivel, S., Shankar, M. V., Palanichamy, M., Arabindoo, B., Bahnemann, D. W., Murugesan, V. (2004a). Enhancement of photocatalytic activity by metal deposition: characterisation and photonic efficiency of Pt, Au, and Pd deposited on TiO_2 catalyst. *Water Research* **38**: 3001-3008.

Sakthivel, S., Janczarek, M., Kisch, H. (2004b). Visible light activity and photoelectrochemical properties of nitrogen-doped TiO_2. *Journal of Physical Chemistry B* **108**: 19384-19387.

Shioya, Y., Ikeue, K., Ogawa, M., Anpo, M. (2003). Synthesis of transparent Ti-containing mesoporous silica thin film meterials and their unique photocatalytic activity for the reduction of CO_2 with H_2O. *Applied Catalysis A* **254**: 251-259.

Tseng, I. H., Chang, W. C., Wu, J. C. S. (2002). Photoreduction of CO_2 using sol-gel derived titania and titania-supported copper catalysts. *Applied Catalysis B* **37**: 37-48.

Tseng, I. H., Wu, J. C. S. (2004). Chemical states of metal-loaded titania in the photoreduction of CO_2. *Catalysis Today* **97**: 113-119.

Tian, G. H., Fu, H. G., Jing, L. Q., Xin, B. F., Pan, K. (2008). Preparation and characterization of stable biphase TiO_2 photocatalyst with high crystallinity, large surface area, and enhanced photoactivity. *Journal of Physical Chemistry C* **112**: 3083-3089.

Varghese, O. K., Paulose, M., LaTempa, T. J., Crimes, C. A. (2009). High-rate solar photocatalytic conversion of CO_2 and water vapour to hydrocarbon fuels. *Nano Letters* **9**: 731-737.

Wu, J. C. S., Yeh, C. Y. (2001). Sol-gel derived photosensitive TiO_2 and Cu/TiO_2 esing homogeneous hydrolysis technique. *Journal of Materials Research* **16**: 2.

Wu, J. C. S., Tseng, I. H., Chang, W. C. (2001). Synthesis of titania-supported copper nanoparticles via refined alkoxide sol-gel process. *Journal of Nanoparticle Research* **3**: 113-118.

Xu, Y., Schoonen, M. A. A. (2000). The absolute energy positions of conduction and valence bands of selected semiconducting minerals. *American Mineralogist* **85**: 543-556.

Zhang, Z., Wang, C. C., Zakaria, R., Ying, J. Y. (1998). Role of particle size in nanocrystalline TiO_2-based photocatalysts. *Journal of Physical Chemistry B* **102**: 10871-10878.